Engineering Plasmonic Nanopillar Arrays for Surface-enhanced Raman Spectroscopy

Wu, Kaiyu

Publication date:
2016

Document Version
Publisher's PDF, also known as Version of record

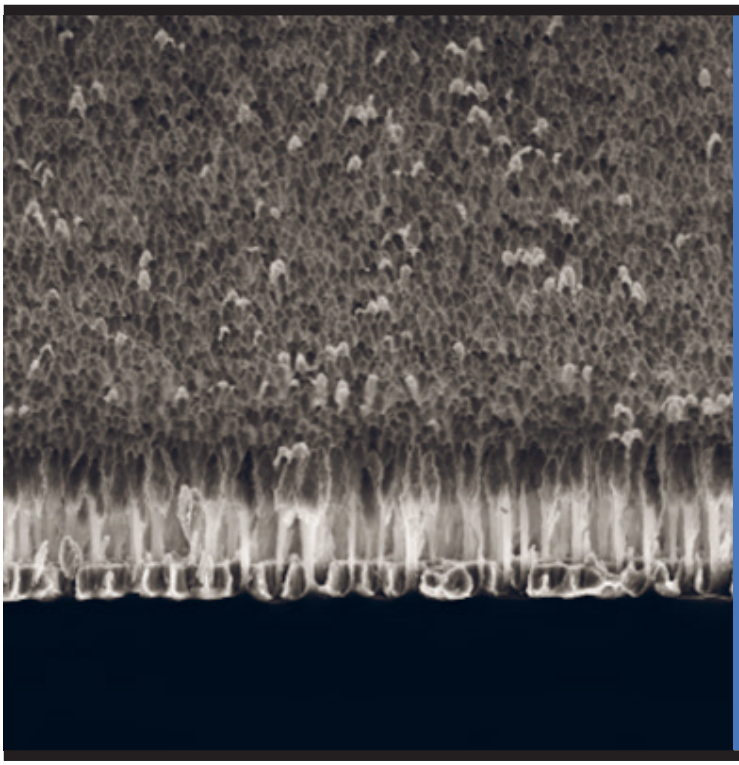

Engineering Plasmonic Nanopillar Arrays for Surface-enhanced Raman Spectroscopy

Kaiyu Wu
PhD Thesis April 2016

DTU Nanotech
Department of Micro- and Nanotechnology

Engineering Plasmonic Nanopillar Arrays for Surface-enhanced Raman Spectroscopy

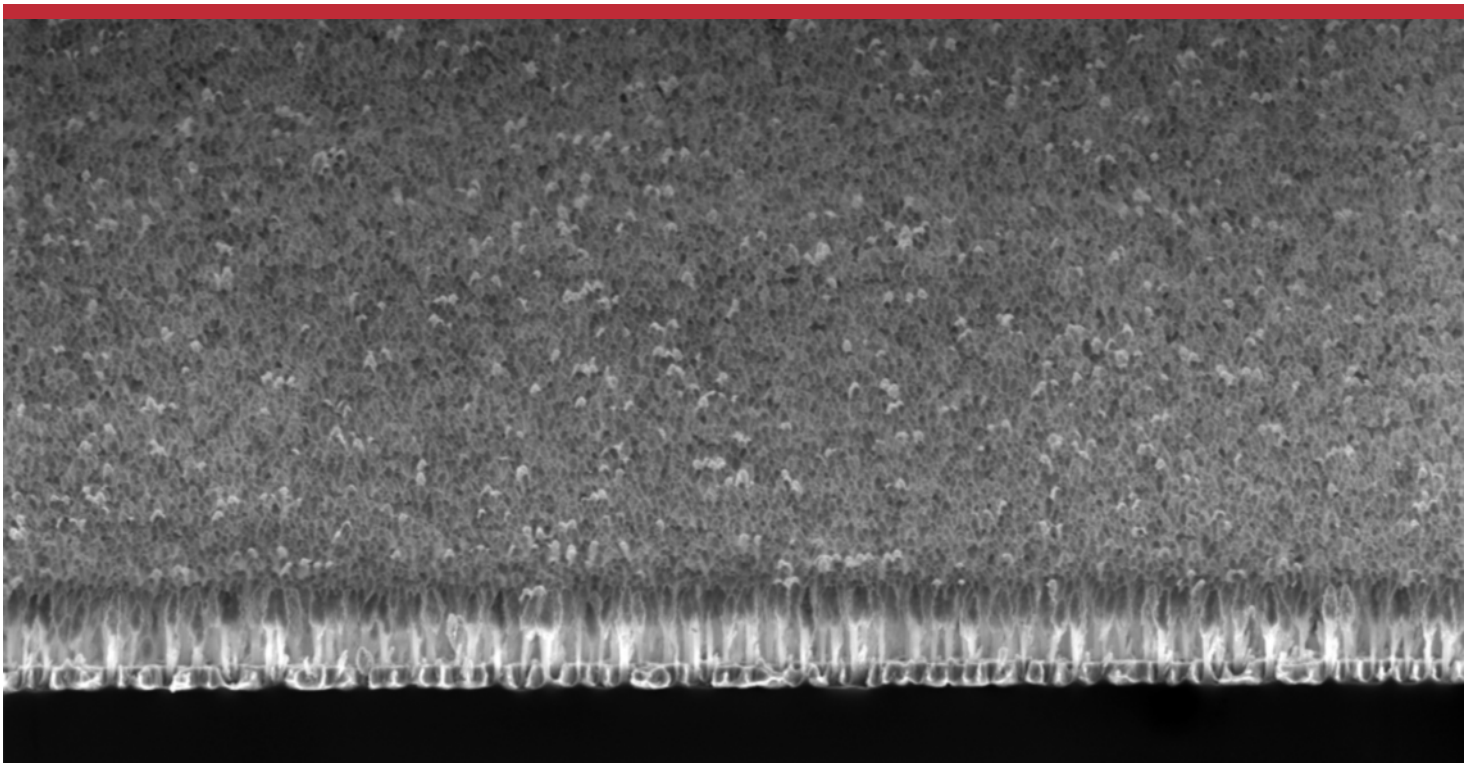

Kaiyu Wu
April 2016

DTU Nanotech
Department of Micro- and Nanotechnology

ENGINEERING PLASMONIC NANOPILLAR ARRAYS FOR SURFACE-ENHANCED RAMAN SPECTROSCOPY

A Thesis
Presented to
The Academic Faculty

by

Kaiyu Wu

In Partial Fulfillment
of the Requirements for the
Ph.D. Degree in the
Department of Micro- and Nanotechnology

Technical University of Denmark
April 2016

ENGINEERING PLASMONIC NANOPILLAR ARRAYS FOR SURFACE-ENHANCED RAMAN SPECTROSCOPY

Main Supervisor:

Professor Anja Boisen,
Department of Micro- and Nanotechnology
Technical University of Denmark

Supervisors:

Researcher Tomas Rindzevicius
Department of Micro- and Nanotechnology
Technical University of Denmark

Senior Researcher Michael Stenbæk Schmidt
Department of Micro- and Nanotechnology
Technical University of Denmark

PREFACE

The scientific work presented in this thesis was carried out at the Department of Micro- and Nanotechnolgy, Technical University of Denmark. The Ph.D. project was funded by the NAPLAS project, the Danish Council for Independent Research. The employment took place in DTU Nanotech, from 1st of May, 2013, until 30th of April, 2016.

ACKNOWLEDGEMENTS

First, I want to thank my supervisors, Professor Anja Boisen, Researcher Tomas Rindzevicius, and Senior Researcher Michael Stenbæk Schmidt, for giving me the opportunity to carry out this Ph.D. project. I deeply appreciate all your contributions of time, ideas and funding to help me complete my Ph.D. study. Specifically, I would like to thank Professor Anja Boisen, for the always positive and motivating atmosphere around, and the excellent example she has provided as a successful professor. Her teachings, both consciously and unconsciously, will affect and benefit me for a lifetime. I would like to express my deepest gratitude to Researcher Tomas Rindzevicius, for the invaluable guidance and examples he has provided me, on how to be a professional scientist and how to write a decent scientific paper. I am particularly grateful to Senior Researcher Michael Stenbæk Schmidt, for all the experimental advice, and all his care for my personal life. To me, he is the know-it-all person in regards to cleanroom fabrications. Without his knowledge, this Ph.D. project would not even exist. Furthermore, I would like to thank again both Researcher Tomas Rindzevicius and Senior Researcher Michael Stenbæk Schmidt, for the countless times of scientific discussions, which are always constructive. I am extremely lucky to have all of them as my Ph.D. supervisors.

I would like to thank Senior Researcher Klaus Bo Mogensen for allowing me to use his Dark-field setup. I would like to express my gratitude to Dr. Aron Hakonen, Professor Michael Käll from Chalmers University of Technology, Associate Professor Sanshui Xiao from DTU Photonics, and again Senior Researcher Klaus Bo Mogensen for the valuable inputs on my manuscripts.

It has been my honor to work for the Nanoprobes group, which has been a source of friendships as well as excellent advice and collaboration. I greatly appreciate Rasmus Schmidt, Professor Silvan Schmid, Assistant Professor John J. Castillo, Anil Haraksingh Thilsted, and Dr. Tao Li for engaging me in their projects as a collaborator. The collaborations have widened my scientific perspective, and the outcomes are fruitful. Special thanks to Onur Durucan and Anil Haraksingh Thilsted for the countless times of "scientific chats", which are often insightful and let us share knowledge. I also would like

to thank Rikke Kragh Lauridsen, Dr. Anna Line Brøgger, Dr. Peter Emil Larsen, Dr. Kasper Bayer Frøhling, Senior Researcher Tommy Sonne Alstrøm and Lidia Morelli for scientific discussions. I learned a lot from them.

Lastly, I would like to thank my family, for the kindness of my parents in raising me, for their support in all my pursuits, and for the love and encouragement from my wife.

Kaiyu Wu
DTU Nanotech
March 2016

ABSTRACT

This Ph.D. thesis presents (i) an in-depth understanding of the localized surface plasmon resonances (LSPRs) in the nanopillar arrays (NPs) for surface-enhanced Raman spectroscopy (SERS), and (ii) systematic ways of optimizing the fabrication process of NPs to improve their SERS efficiencies.

This Ph.D. project is part of the NAPLAS - NAnoPLAsmonic Sensors project, funded by The Danish Council for Independent Research.

LSPRs in silver capped silicon NPs are studied using numerical simulations and dark-field scattering microscopy. Simulations show that a standalone NP supports two LSPR modes, i.e., the particle mode and the cavity mode. The particle mode can be hybridized via leaning of pillars. The LSPR wavelength of the cavity mode is dominant only by the diameter of the Si pillar. The presence of a substrate dramatically changes the intensities of these two LSPR modes, by introducing constructive and destructive interference patterns with the excitation fields. Experimental scattering spectra can be interpreted using theoretical simulations.

The processes, which affect the SERS efficiencies of the silver NPs, are systematically evaluated. Short exposures to the O_2-plasma and the use of 1-3 nm Cr adhesion layers are advantageous for reducing the SERS background signals. Influence of the NP height and silver deposition thickness on SERS intensities is also investigated. Using an optimized recipe, the measured SERS enhancement factor (EF) reaches 10^8, and the SERS signal intensity exhibits a standard deviation of ~14% (660 data points) across a 5 x 5 mm^2 surface area.

Lastly, a further improved process shows that high-density NPs exhibit unrivalled macroscale SERS uniformities (RSD: ~2.5% in mm scale, ~7% in inch scale) and SERS reproducibilities (RSD: ~1.5% across three wafers), while at the same time displaying a very large average SERS EF of $>10^8$.

From a practical point of view, the developed SERS substrates are particularity interesting, since they are easy to handle and store and the fabrication is scalable, facilitating a wide and simple use of SERS in sensing applications.

DANSK RESUME

Denne Ph.D. afhandling præsenterer (i) en tilbundsgående undersøgelse af de lokale overflade plasmon resonanser (LSPR) som befinder sig på nanosøjler i forbindelse med overflade forstærket Raman spektroskopi (SERS) og (ii) en systematisk optimeringen af fremstillingsprocessen af NP med henblik på at forbedre SERS effektiviteten.

Dette Ph.D. projekt er udført som en del af NAPLAS – NAnoPLAsmonic Sensors – projektet som er finansieret af det Det Frie Forskningsråd.

LSPR i silicium nanosøjler belagt med sølv er undersøgt med numeriske simuleringer og optisk mikroskopi. Simuleringerne viser at en enkelt sølv nanosøjle understøtter to LSPR svingninger; en partikelsvingning og en kavitetssvingning. Partikelsvingningen er hybridiseret ved at søjlerne læner sig mod hinanden. Kavitetssvingningen er domineret af diameteren af silicium søjlerne. Ved at introducere en vandret overflade under søjlerne ændres intensiteten af de to LSPR svingninger sig drastisk ved at introducere et konstruktiv og et destruktiv interferens mønstrer i eksitationsfeltet. Eksperimentelle spredningsspektre blev fortolket vha. teoretiske simuleringer.

Fabrikationsprocesserne som har indflydelse på SERS effektiviteten af sølv dækket nanosøjler blev evalueret systematisk. En kort behandling med en O_2-plasma og brug af et 1-3 nm krom vedhæftningslag under sølvet er fordelagtige mht. at reducere SERS baggrundssignaler. Indflydelsen af nanosøjlernes højde og sølv tykkelsen på SERS intensiteten blev også undersøgt. Ved at bruge en optimeret fremstillingsmetode blev SERS effekten (EF) målt til 10^8. Intensiteten af SERS signalet havde en standard afvigelse på ~14% over et område på 5 x 5 mm^2 (660 data punkter).

Yderligere optimering viste at ved at forhøje tætheden af nanosøjler kunne man opnå en unik makroskala SERS uniformitet (RSD: ~2.5% på mm skala) og en høj reproducerbarhed (RSD: ~1.5% imellem tre forskellige overflader) alt imens en meget høj SERS EF på over 10^8 blev opnået.

Set fra et praktisk synspunkt er det udviklede SERS substrat især interessant fordi det er nemt at opbevare og håndterer. Samtidigt kan fabrikations metoden opskaleres hvormed det bliver muligt at bruge disse SERS substrater i en lang række praktiske anvendelser hvor kemiske stoffer skal spores.

PUBLICATIONS

In this cumulative thesis, chapters 6 – 8 are composed of the three scientific journal papers below, respectively.

[P1] K. Wu, T. Rindzevicius, M. S. Schmidt, K. B. Mogensen, A. Hakonen and A. Boisen, "Wafer-Scale Leaning Silver Nanopillars for Molecular Detection at Ultra-Low Concentrations," *J. Phys. Chem. C* **119**, 2053 - 2062 (2015)

[P2] K. Wu, T. Rindzevicius, M. S. Schmidt, K. B. Mogensen, S. Xiao and A. Boisen, "Plasmon Resonances of Ag capped Si Nanopillars Fabricated Using Mask-less Lithography," *Opt. Express* **23**, 12965 - 12978 (2015)

[P3] K. Wu, T. Rindzevicius, M. S. Schmidt, A. H. Thilsted and A. Boisen, "Macroscale SERS Uniformity and Reproducibility Using Densely Clustered Nanopillars," Manuscript under review.

MY CONTRIBUTIONS

[P1] I did all the work presented in the paper, participated in the discussions on the interpretation of the results, and wrote a draft of the paper.

[P2] I did all the work presented in the paper, participated in the discussions on the interpretation of the results, and wrote a draft of the paper.

[P3] I did all the work presented in the paper, participated in the discussions on the interpretation of the results, and wrote a draft of the paper.

TABLE OF CONTENTS

	Page
PREFACE	iii
ACKNOWLEDGEMENTS	iv
ABSTRACT	vi
PUBLICATIONS	ix
MY CONTRIBUTIONS	x
LIST OF FIGURES	xv
LIST OF SYMBOLS AND ABBREVIATIONS	xvii

CHAPTER

1	INTRODUCTION	1
	1.1 State-of-the-art Plasmonic Systems for Surface-enhanced Raman Spectroscopy	1
	1.2 Objective of the Ph.D. Project	3
	1.3 Structure of the Thesis	4
2	RAMAN EFFECT FOR PROBING VIBRATIONAL STATES OF MOLECULES	9
	2.1 Molecular Vibrations	9
	2.2 Infrared Absorption	11
	2.3 Raman Scattering	14
	2.4 Electromagnetic Interpretation of Raman Scattering	16
3	LOCALIZED SURFACE PLASMON RESONANCE	20
	3.1 Optical Properties of Bulk Metal	20
	3.1.1 DC Conductivity of Metal	21

3.1.2 AC Conductivity of Metal 22

3.1.3 Dielectric Function of Metal 24

3.2 Optical Properties of a Spherical Metallic Nanoparticle 26

3.2.1 Localized Surface Plasmon Resonance of a Spherical Metallic Nanoparticle 27

3.2.2 Field Enhancement near a Spherical Metallic Nanoparticle 31

4 SURFACE-ENHANCED RAMAN SPECTROSCOPY 34

4.1 Enhancement Mechanisms of Surface-enhanced Raman Scattering 34

4.2 Requirement in Plasmonic Systems for Surface-enhanced Raman Spectroscopy 36

5 NANOPILLAR ARRAYS FOR SURFACE-ENHANCED RAMAN SPECTROSCOPY 40

5.1 Large-area Fabrication of Nanopillars by Lithography-free Processes 40

5.2 Clustering of Nanopillars and Formation of Hot Spots 41

6 PLASMON RESONANCES OF AG CAPPED SI NANOPILLARS FABRICATED USING MASK-LESS LITHOGRAPHY [P1] 45

1 Introduction 46

2 Simulation Model 48

3 Results and Discussion 49

3.1 LSPR Modes of a Single NP 49

3.2 LSPR Wavelengths Broadening of the NPs 52

3.3 LSP Couplings in an Ag NP Dimer 55

3.4 Scattering Measurements on NP Substrates 56

4 Conclusion 59

5 Appendix 59

5.1 Fabrication of NP Substrates 59

5.2 Scattering Measurements 60

5.3 SERS Measurements 61

5.4 LSPR Contribution of the Nanoholes 61

5.5 Further Evidence Proving the Existence of the Cavity LSPR Mode 62

5.6 Geometric Changing of the NP Substrate when Increasing the Ag Deposition Thickness 63

5.7 SERS Uniformity of the NP Substrate 64

6 Acknowledgement 64

7 WAFER-SCALE LEANING SILVER NANOPILLARS FOR MOLECULAR DETECTION AT ULTRA-LOW CONCENTRATIONS [P2] 70

1 Introduction 71

2 Theoretical Methods 74

3 Experimental Methods 76

4 Results and Discussion 78

4.1 O_2 Plasma Treatment 78

4.2 Cr Adhesion Layers 81

4.3 Height of the Ag NPs 83

4.4 Thickness of the Ag Metal Film 85

4.5 Optimized Ag NP Structures for SERS Applications 86

5 Conclusions 89

6 Supporting Information 90

7 Acknowledgement 95

8 MACROSCALE SERS UNIFORMITY AND REPRODUCIBILITY USING DENSELY CLUSTERED NANOPILLARS [P3] 102

1 Introduction 103

2 Results and Discussions 106

2.1 Density Control in the Lithography-free Process 106

2.2 Influence of NP Density on SERS Uniformity 109

2.3 Large-area SERS Uniformity and Wafer-to-wafer SERS Reproducibility of the Densely Clustered Nanopillars 111

2.4 Reproducible SERS Analysis on High-density Nanopillars 113

3 Conclusion 115

4 Experimental Section 116

5 Supporting Information 118

6 Acknowledgements 121

9 CONCLUDING REMARK 125

LIST OF FIGURES

Page

Figure 2.1: Harmonic vibration of a diatomic molecule 10

Figure 2.2: Schematic of IR absorption 12

Figure 2.3: Vibrational modes of a triatomic molecule 13

Figure 2.4: Schematic of Raman scattering 14

Figure 3.1: Photos of the Lycurgus cup 27

Figure 3.2: Schematic of LSPR in a spherical metallic nanoparticle 28

Figure 3.3: Quasi-static model of a spherical metallic nanoparticle 28

Figure 5.1: Process flow of nanopillar arrays 41

Figure 5.2: Concept of the leaning NP substrate 42

Chapter 6 [Paper 1]

Figure 1: Geometric model and SEM images of Ag capped Si NPs 49

Figure 2: Calculated scattering cross section and field distribution of a single NP 50

Figure 3: Calculated scattering cross section of single NPs with different geometries 53

Figure 4: Calculated scattering cross section and field distribution of a NP dimer 55

Figure 5: Measured scattering spectra and SERS spectra obtained on NP substrates 57

Figure 6: A schematic of the dark-field scattering measurements 60

Figure 7: Measured scattering spectra and SERS spectra on NPs and nanoholes 62

Figure 8: Calculated scattering spectra for a dimer of NPs with/without Si cavities 63

Figure 9: SEM images of the NP substrates with different Ag deposition thicknesses 63

Figure 10: Mapped SERS spectra on the NP substrate 64

Chapter 7 [Paper 2]

Figure 1: Measured and simulated scattering spectra, and field distributions of a NP 75

Figure 2: Summary of the fabrication process steps for the Ag NP SERS substrates 78

Figure 3: SERS signals and backgrounds vs O_2-plasma time 79

Figure 4: SERS signals and backgrounds vs Cr adhesion layer thickness 82

Figure 5: Scanned SERS spectra on Ag NP structures with varying NP height 84

Figure 6: SERS signals vs Ag deposition thickness at 780 nm excitations 86

Figure 7: Performance of the Ag NPs fabricated using the optimized recipe 87

Figure S.1: Calculated absorbance spectra and E-field maps for isolated Ag NPs 91

Figure S.2: SERS spectra of thiophenol on Ag NPs with varying NP height 91

Figure S.3: SERS signals vs Ag deposition thickness at 532 nm excitations 92

Figure S.4: SERS spectra of thiophenol on leaned and non-leaned Ag NPs 93

Figure S.5: Calculated scattering spectra of an Ag NP with different shaped Ag caps 94

Chapter 8 [Paper 3]

Figure 1: SEM images and scanned SERS spectra of low- and high-density NPs 106

Figure 2: SEM images of NPs with different densities and the relationship between density and RIE pressure 107

Figure 3: SERS spectra measured on NPs fabricated using different RIE pressures 109

Figure 4: Averaged SERS signal intensities, SERS signal RSDs and SERS line scans obtained on NPs of different densities. 110

Figure 5: Macroscale SERS line scans and SEM images of the high-density NPs 112

Figure 6: An example of SERS analyses using the high-density NP substrates 114

Figure S.1: Optimization of the high-density NPs 118

Figure S.2: Dark-field scattering spectra of the optimized high-density NPs 119

Figure S.3: Distribution of the SERS intensities obtained on high-density Si NPs 120

LIST OF SYMBOLS AND ABBREVIATIONS

m	Mass
m_r	Relative mass
k_r	Force constant
F_r	Restoring force
C	Constant
v_m	Molecular vibrational frequency
V	Potential energy
E	Energy
h	Planck constant
v_p	Photon frequency
$\boldsymbol{\mu}$	Dipole moment
Q	Vibrational coordinate
v_{L}	Light frequency
v_{s}	Stokes frequency
v_{as}	Anti-Stokes frequency
α	Polarizability
E_0	Amplitude of electrical field
Q_0	Magnitude of molecular vibration
P	Power of light
k	Boltzmann constant
T	Temperature
τ	Mean free time

$\mathbf{J}$	Current density
σ	Conductivity
$\mathbf{E}$	Electrical field
$\boldsymbol{v}$	Velocity
m_e	Mass of an electron
e	Charge of an electron
σ_0	DC conductivity
ω	Angular frequency
$\boldsymbol{p}$	Momentum
$\mathbf{B}$	Magnetic field
ε_0	Permittivity of free space
μ_0	Permeability of free space
c	Speed of light in vacuum
ε	Permittivity
k	Wave number
ω_p	Plasma frequency of electrons
Φ	Electrical potential
g	Electrical field enhancement factor
I	Intensity of light
σ'_{RS}	Chemically enhanced Raman cross section
σ_{RS}	Free Raman cross section
$\mathrm{EF}_{\mathrm{SERS}}$	Total SERS enhancement factor
$\mathrm{EF}_{\mathrm{EM}}$	Electromagnetic SERS enhancement factor
$\mathrm{EF}_{\mathrm{CHEM}}$	Chemical SERS enhancement factor

LSPR	Localized surface plasmon resonance
NP	Nanopillar array
SERS	Surface-enhanced Raman spectroscopy
Ag	Silver
Si	Silicon
Cr	Chromium
EF	Enhancement factor
RSD	Relative standard deviation
IR	Infrared
DC	Direct current
AC	Alternating current
UV	Ultra-violet
SERRS	Resonant surface-enhanced Raman scattering
SEM	Scanning electron microscope
FEM	Finite element method

CHAPTER 1

INTRODUCTION

The scientific contents of this thesis fall in the area of surface-enhanced Raman spectroscopy (SERS), which is an iconic application of nanoplasmonic systems. Specifically, the Ph.D. study focuses on one important SERS structure — the plasmonic nanopillar arrays. In the introductive chapter, section 1.1 presents a review on the state-of-the-art plasmonic systems for SERS applications. Section 1.2 describes the motivation and the objective of the Ph.D. project. The structure of the thesis is summarized in section 1.3.

1.1 State-of-the-art Plasmonic Systems for Surface-enhanced Raman Spectroscopy

SERS is a spectroscopic technique. It probes the significantly increased Raman scattering signals from the molecules attached to, or in the very close vicinity of metallic nanostructures, and identifies these molecules by their distinguished Raman lines. Since it was recognized in 1977, that enhanced Raman spectra could be obtained from molecules sitting on electrochemically roughened metal surfaces,[16] the field of SERS has exploded. Until now, over 13,000 research articles in the field of SERS can be found in the literature.[1] Incredibly, the field is still expanding. In the year of 2015 only, more than 1600 research articles regarding SERS were published.[1] These facts, demonstrate the power of SERS as an ultra-sensitive molecular probe, and its immense impact on a wide range of fields, such as physics,[2, 3] chemistry,[4, 5] material science,[6 - 9] life science,[10, 11] food industry,[12, 13] and environmental security.[14, 15] Two important driving forces behind the field of SERS, are the rapid advances of nanotechnology, and the development of highly efficient laser systems.[16, 19]

Essentially, SERS is a prominent spectroscopic application of metallic nanostructures. In SERS, the enhancement of the Raman scattered light arises in two ways.[16] First, the excitation field and the Raman scattering field can receive

magnifications, near metallic nanostructures that support localized surface plasmon resonance (LSPR). This is the electromagnetic enhancement of SERS. Second, electronic interactions between the molecule and the metal can affect the Raman scattering process itself, and can consequently increase the Raman cross section of the molecule. Such an effect is the chemical enhancement of SERS. The total SERS enhancement factor (EF) is the product of the electromagnetic EF and the chemical EF. A detailed explanation of the SERS enhancement mechanisms is given in chapter 4, section 4.1.

Fabricating and engineering plasmonic systems for SERS is one important research branch in the field. In the early years, increasing EF has been the focus. After successfully reaching the goal of single-molecule SERS,[17, 18, 20] the community turned its focus toward developments of robust plasmonic systems, and effective surface modification methods, to transform SERS into a practically useful analytical technique. According to recent reviews,[21, 22] to achieve widespread use in practical applications, a SERS-active plasmonic system should possess (i) compatibility with high-volume manufacturing process flows, (ii) high and reproducible EF, i.e. enhancement uniformity, over large surface areas, and (iii) a tunable LSPR wavelength over a broad spectral region. Early systems, fabricated by electrochemical roughening, suffered greatly from irreproducibility.[16] Thanks to the rapid development of nanofabrication techniques, state-of-the-art SERS systems can be fabricated in a more reproducible manner, with better-defined morphologies. Despite such, the goal and the standards listed above are not straightforward to achieve, due to the non-uniform nature of the local optical fields near the metallic nanostructures.[23]

In terms of fabrication method, the majority of the modern SERS systems can be divided into two categories: nanoparticle colloidal suspensions and structural solid substrates.

A number of plasmonic metallic nanoparticles in colloidal solutions have been synthesized. Notable examples include shell-isolated nanoparticles,[24] core-shell nanoparticles,[25] and nanoparticles with sharp features.[26,27] These structures are easy to prepare, with widely tunable LSPR wavelengths. Their main advantage is the high electromagnetic EFs caused by (i) intra- or inter particle plasmonic couplings, and (ii) lightning-rod effect that is specifically pronounced in metallic nanoparticles with sharp

features. Since the electromagnetic EF is extremely sensitive to the inter particle spacing, it is necessary to control the size of the gap junctions between nanoparticles to achieve a spatially more uniform EF. For example, bio-template assisted synthesis can be used to realize sub-10 nm distance control between nanoparticles.[28] Recently, reliable and quantitative SERS analysis has been reported using core–shell nanoparticles with embedded internal standards,[29] or alkanethiolate ligand-regulated silver nanoparticle films.[30]

SERS-active structural solid substrates are usually fabricated by top-down processes.[31] Most of them are lithography-based techniques, which first tailor mask layers to form different nanostructured patterns, which are then transferred into a variety of substrate materials. The rendered structures are subsequently metalized to make the surface SERS-active.[32-36] In these systems, strong EFs are obtained at hot spots formed either at the gap junctions between individual structures[37-39], or at the metallic nanogrooves[40] and nanotips.[41,42] Structural solid SERS substrates usually exhibit more reproducible SERS signals across larger surface areas compared to colloidal nanoparticle systems, at the cost of lower EFs.[43-45]

1.2 Objective of the Ph.D. Project

This Ph.D. project is part of the NAPLAS - NAnoPLAsmonic Sensors project, funded by The Danish Council for Independent Research. The core element of the NAPLAS project is the nanopillar arrays, which is a plasmonic structure for SERS-based sensing. Specifically, these nanopillar arrays are fabricated by a lithography-free process, which was developed by Senior Researcher Michael Stenbæk Schmidt in the Nanoprobes group at DTU Nanotech. The employed process is wafer-scale, and since it does not require any lithographic step, is fast and repeatable, thus providing possibilities for the produced substrates to be used as cheap and expendable consumables.

To achieve widespread use in practical applications, a SERS substrate should possess (i) a compatibility with high-volume manufacturing process flows, (ii) a high and spatially uniform EF over large areas, and (iii) a tunable LSPR wavelength over a broad spectral region. To develop these nanopillar arrays into a robust SERS platform and maximize the advantage of their cost-effective and high-throughput manufacturing

process, a more thorough understanding of their LSPR properties and their fabrication process capabilities is required. There is a need for further theoretical and experimental work to address (i) the nature of their localized surface plasmon excitations, and subsequently (ii) evaluate experimental procedures that affect their electromagnetic EF, EF spatial uniformity and SERS background signals.

For the reasons above, the objectives of this Ph.D. project are (i) to develop an in-depth understanding of LSPR coupling effects in the nanopillar arrays using advanced spectroscopic and theoretical tools, and (ii) to tailor the optical properties and adjust the fabrication process of the nanopillar arrays, on the basis of (i), to transform such structures into a more robust SERS platform with a higher EF, a lower SERS background signal, and a spatially more uniform EF.

1.3 Structure of the Thesis

This thesis consists of nine chapters, which are divided into four sections. After chapter 1 – introduction, the second section consists of chapter 2 - Raman effect for probing vibrational states of molecules, chapter 3 – localized surface plasmon resonance, and chapter 4 – surface-enhanced Raman spectroscopy. This section addresses the scientific foundation of the Ph.D. project. The derived properties and conclusions from the simple theoretical models are important facts that guide the Ph.D. project to its research goals. The third section is composed of chapters 5 – 8. Chapter 5 – nanopillar arrays for surface-enhanced Raman spectroscopy, introduces the research subject of the Ph.D. project. The original findings of the Ph.D. study and the utilized methodologies are presented in chapter 6 – plasmon resonances of Ag capped Si nanopillars fabricated using mask-less lithography, chapter 7 – wafer-scale leaning silver nanopillars for molecular detection at ultra-low concentrations, and chapter 8 – macroscale SERS uniformity and reproducibility using densely clustered nanopillars. As a cumulative thesis, its chapters 6 – 8 are respectively three scientific journal papers. The fourth and final section of the thesis is chapter 9 – concluding remark, which consolidates the discrete conclusions presented in chapters 6 – 8, and puts the key results into a broader context.

References

[1] Thomson Reuters, Web of Science.

[2] P. Roelli, C. Galland, N. Piro, T. J. Kippenberg, *Nat. Nanotechnol.* **2016,** *11*, 164

[3] M. Moskovits, *Rev. Mod. Phys.* **1985**, *57*, 783.

[4] J. R. Lombardi, R. L. Birke, T. Lu, J. Xu, *J. Chem. Phys.* **1986**, *84*, 4174.

[5] D.-Y Wu, X.-M. Liu, S. Duan, X. Xu, B. Ren, S.-H Lin, Z.-Q. Tian, *J. Phys. Chem. C* **2008**, *112*, 4195.

[6] F. Schedin, E. Lidorikis, A. Lombardo, V. G. Kravets, A. K. Geim, A. N. Grigorenko, K. S. Novoselov, A. C. Ferrari**,** *ACS Nano* **2010**, *4*, 5617.

[7] S.-Y. Chou, C.-C. Yu, Y.-T. Yen, K.-T. Lin, H.-L. Chen, W.-F. Su, *Anal. Chem.* **2015**, *87*, 6017.

[8] B. Sharma, R. R. Frontiera, A.-I. Henry, E. Ringe, R. P. Van Duyne, *Mater. Today* **2012**, *15*, 16.

[9] S. Murphy, L. Huang, P. V. Kamat, *J. Phys. Chem. C* **2013**, *117*, 4740.

[10] W. Xie, S. Schlücker, *Phys. Chem. Chem. Phys.* 2013, **15**, 5329.

[11] M. V. Yigit, L. Zhu, M. A. Ifediba, Y. Zhang, K. Carr, A. Moore, Z. Medarova, *ACS Nano* **2011**, *5*, 1056.

[12] J.-M. Li, W.-F. Ma, C. Wei, L.-J. You, J. Guo, J. Hu, C.-C. Wang**,** *Langmuir* **2011**, *27*, 14539.

[13] A. Kim, S. J. Barcelo, R. S. Williams, Z. Li, *Anal. Chem.* **2012**, *84*, 9303.

[14] A. Hakonen, T. Rindzevicius, M. S. Schmidt, P. O. Andersson, L. Juhlin, M. Svedendahl, A. Boisen, M. Käll. *Nanoscale*, **2016**, *8*, 1305.

[15] R. A. Halvorson, P. J. Vikesland, *Environ. Sci. Technol.* **2010**, *44*, 7749.

[16] P. L. Stiles, J. A. Dieringer, N. C. Shah, R. P. Van Duyne, *Annu. Rev. Anal. Chem.* **2008**, *1*, 601.

[17] S. M. Nie, S. R. Emery, *Science*, **1997**, *275*, 1102.

[18] K. Kneipp, Y. Wang, H. Kneipp, L. T. Perelman, I. Itzkan, R. R. Dasari, M. S. Feld, *Phys. Rev. Lett.* **1997**, *78*, 1667.

[19] K. Kneipp, *Phys. Today* **2007**, 40.

[20] H. Xu, E. J. Bjerneld, M. Käll, L. Börjesson, *Phys. Rev. Lett.* **1999**, *83*, 4357.

[21] S. Schlücker, *Angew. Chem. Int. Ed.* **2014**, *53*, 4756.

[22] B. Sharma, M. F. Cardinal, S. L. Kleinman, N. G. Greeneltch, R. R. Frontiera, M. G. Blaber, G. C. Schatz, R. P. Van Duyne, *MRS Bulletin* **2013**, *38*, 615.

[23] H. Wei, H. Xu, *Nanoscale*, **2013**, *5*, 10794.

[24] J. F. Li, Y. F. Huang, Y. Ding, Z. L. Yang, S. B. Li, X. S. Zhou, F. R. Fan, W. Zhang, Z. Y. Zhou, D. Y. Wu, B. Ren, Z. L. Wang, Z. Q. Tian, *Nature* **2010**, *464*, 392.

[25] A. K. Samal, L. Polavarapu, S. Rodal-Cedeira, L. M. Liz-Marzán, J. Pérez-Juste, I. Pastoriza-Santos, *Langmuir* **2013**, *29*, 15076.

[26] V, López-Puente, S. Abalde-Cela, P. C. Angelomé, R. A. Alvarez-Puebla, L. M. Liz-Marzán, *J. Phys. Chem. Lett.* **2013**, *4*, 2715.

[27] L. Pérez-Mayen, J. Oliva, A. Torres-Castro, E. De la Rosa, *Nanoscale* **2015**, *7*, 10249.

[28] D.-K. Lim, K.-S. J, J.-H. Hwang, H. Kim, S. Kwon, Y. D. Suh, J.-M. Nam, *Nat. Nanotechnol.* **2011**, *6*, 452.

[29] W. Shen, X. Lin, C. Jiang, C. Li, H. Lin, J. Huang, S. Wang, G. Liu, X. Yan, Q. Zhong, B. Ren, *Angew. Chem.* **2015**, *127*, 7416.

[30] H.-Y. Chen, M.-H. Lin, C.-Y. Wang, Y.-M. Chang, S. Gwo, *J. Am. Chem. Soc.* **2015**, *137*, 13698.

[31] B. Sharma, M. F. Cardinal, S. L. Kleinman, N. G. Greeneltch, R. R. Frontiera, M. G. Blaber, G. C. Schatz, R. P. Van Duyne, *MRS Bulletin* **2013**, *38*, 615.

[32] T.-W. Chang, M. R. Gartia, S. Seo, A. Hsiao, G. L. Liu, *Nanotechnology* **2014**, *25*, 145304.

[33] C. Hou, G. Meng, Q. Huang, C. Zhu, Z. Huang, B. Chena, K. Suna, *Chem. Commun.* **2014**, *50*, 569.

[34] Y. Zhao, Y.-L. Zhang, J.-A. Huang, Z. Zhang, X. Chen, W. Zhang, *J. Mater. Chem. A* **2015**, *3*, 6408.

[35] J. Li, C. Chen, H. Jans, X. Xu, N. Verellen, I. Vos, Y. Okumura, V. V. Moshchalkov, L. Lagaea, P. V. Dorpe, *Nanoscale* **2014**, *6*, 12391.

[36] V. Merk, J. Kneipp, K. Leosson, *Adv. Opt. Mater.* **2013**, *1*, 313.

[37] X. Liu, Y. Shao, Y. Tang, K.-F. Yao, *Sci. Rep.* **2014**, *4*, 5835.

[38] M. Hu, F. S. Ou, W. Wu, I. Naumov, X. Li, A. M. Bratkovsky, R. S. Williams, Z. Li, *J. Am. Chem. Soc.* **2010**, *132*, 12820.

[39] A. Hakonen, M. Svedendahl, R. Ogier, Z.-J. Yang, K. Lodewijks, R. Verre, T. Shegai, P. O. Anderssonb, M. Käll, *Nanoscale* **2015**, *7*, 9405.

[40] M. Yilmaz, M. Ozdemir, H. Erdogan, U. Tamer, U. Sen, A. Facchetti, H. Usta, G. Demirel, *Adv. Funct. Mater.* **2015**, *25*, 5669.

[41] A. S. D. S. Indrasekara, S. Meyers, S. Shubeita, L. C. Feldman, T. Gustafsson, L. Fabris, *Nanoscale* **2014**, *6*, 8891.

[42] Y. Lu, G. L. Liu, J. Kim, Y. X. Mejia, L. P. Lee, *Nano Lett.* **2005**, *5*, 119.

[43] Q. Zhang, Y. H. Lee, I. Y. Phang, C. K. Lee, X. Y. Ling, *Small* **2014**, *10*, 2703.

[44] H. Liu, X. Zhang, T. Zhai, T. Sander, L. Chen, P. J. Klarb, *Nanoscale* **2014**, *6*, 5099.

[45] A. N. Severyukhina, B. V. Parakhonskiy, E. S. Prikhozhdenko, D. A. Gorin, G. B. Sukhorukov, H. Möhwald, A. M. Yashchenok, *ACS Appl. Mater. Inter.* **2015**, *7*, 15466.

CHAPTER 2

RAMAN EFFECT FOR PROBING VIBRATIONAL STATES OF MOLECULES

The most important scientific foundation of this thesis is the Raman scattering effect, which can be used as a spectroscopic technique to identify molecules. By probing molecular vibrational states, Raman spectroscopy reveals the structural information of analytes. In this chapter, molecular vibration is first illustrated using a simple harmonic oscillating model. Then, Raman scattering, together with its complementary spectroscopic technique — Infrared (IR) spectroscopy, are explained. The advantages and disadvantages of Raman and IR spectroscopies are also discussed. Finally, the physics behind Raman scattering is explained in detail using the classical electromagnetic radiation theory.

2.1 Molecular Vibrations

In a molecule, nuclei vibrate relatively to each other. The simplest model that describes molecular vibration is the harmonic oscillating model, in which two nuclei are restrained by a spring that obeys the Hooke's Law of force. Consider a diatomic molecule composed of atoms A and B, with masses m_a and m_b, respectively. The system is shown in Figure 2.1.

The relative mass m_r can be expressed by

$$m_r = \frac{m_a m_b}{m_a + m_b} \tag{2.1}$$

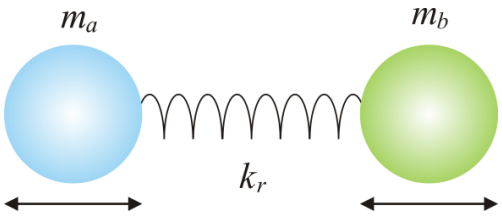

Figure 2.1. Harmonic vibration of a diatomic molecule. A diatomic molecule is composed of atoms A and B, with masses m_a and m_b, respectively. The two nuclei are restrained by a spring that obeys the Hooke's Law of force, with a force constant k_r.

In such a system, the restoring force is proportional to the displacement x, and is thus

$$F_r = -k_r x \tag{2.2}$$

where k_r is the force constant whose value is related to the chemical bonding between A and B. A strong chemical bond leads to a higher k_r, and vice versa. As this is a case of harmonic motion, the following relation holds

$$x(t) = Csin(2\pi v_m t) \tag{2.3}$$

where

$$v_m = \frac{1}{2\pi}\sqrt{\frac{k_r}{m_r}} \tag{2.4}$$

. v_m is the vibrational frequency of the diatomic molecule AB. Equation 2.4 illustrates how the masses of atoms and the force constant, which is related to the strength of the chemical bond, determine the vibrational frequency of a diatomic molecule.

The potential energy of the harmonic oscillating system, in this case a diatomic molecule AB, can be expressed as

$$\mathrm{V}(x) = \frac{1}{2}k_r x^2 \tag{2.5}$$

Obviously, the variation of V with x has a parabolic shape. To quantize the energy, V(x) needs to be solved in the Schrödinger equation. The energies of the solutions that satisfy the boundary conditions are:[1]

$$E_n = \left(n + \frac{1}{2}\right) h\nu_m \qquad n = 0, 1, 2 \ldots \tag{2.6}$$

where n is the vibrational quantum number.[2] It can be seen from equation 2.6 that the energies have a uniform gap of $h\nu_m$, and are proportional to ν_m. In addition, if taking into consideration also equation 2.4, it can be deduced that stronger chemical bonds or smaller masses lead to a bigger gap between adjacent energy levels for diatomic molecules.

2.2 Infrared Absorption

As has been shown in section 2.1, the energy gap between two adjacent energy levels is $h\nu_m$. Similarly, the energy of a photon is $h\nu_p$, where ν_p is the frequency. Therefore, it is possible to trigger direct interactions between photons and vibrational states of molecules, when the following condition is met:

$$\nu_p = \nu_m \tag{2.7}$$

Photons fulfill the above condition are in the IR region of the electromagnetic spectrum. For example, consider a carbon monoxide molecule CO. Since CO is a diatomic molecule, equation 2.4 can be applied to estimate its vibrational frequency. Using the following parameters: force constant k_r = 1860 N/m,[3] mass of ^{12}C = 12 u, and mass of ^{16}O = 16 u, the vibrational frequency of CO is 2143 cm^{-1}, which falls exactly in the IR energy region in the electromagnetic spectrum.

Indeed, a molecule can absorb resonant IR light, causing transitions from a ground vibrational state to the excited vibrational states. IR spectroscopy probes such transitions. A typical IR spectrum is recorded by measuring transmission of a light beam

in the IR region that passes through the sample. Figure 2.2 is a schematic of IR absorption.

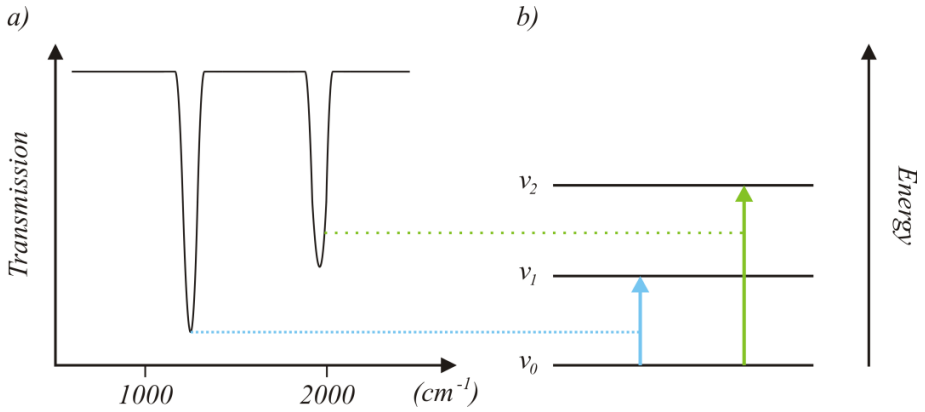

Figure 2.2. Schematic of IR absorption. (a) An example of IR spectrum. (b) The absorptions illustrated in the energy bands correspond accordingly to the dips in the IR spectrum, shown in (a).

Molecular vibrations involve charged blocks of matter. Dipole moment or polarizability changes when a molecule vibrates. For a vibrational mode to be IR-active there must be a change in the dipole moment. To be more specific, another prerequisite in addition to equation 2.7 has to be fulfilled to enable IR absorption:

$$\frac{\partial \mu}{\partial Q} \neq 0 \tag{2.8}$$

where μ is the dipole moment, and Q is the vibrational coordinates of the molecule.[4] The physics behind equation 2.8 can be explained qualitatively in the following way. Since the typical size of a molecule (< 1 nm) is much smaller than the IR wavelength (> 1 μm), it is reasonable to hypothesis that, within the molecule, the electric field is spatially uniform at any given time. Therefore, vibrations that do not involve changes in the dipole moment cannot be driven by such an electric field. In other words, spatially uniform electric fields would never be in resonant with molecular vibrational modes that do not cause changes in the dipole moment. For example, consider a triatomic molecule.

Figure 2.3 shows its vibrational modes. Imagine that a time-varying and spatially uniform electric field is applied on the molecule. Clearly, such a field is not able to drive the symmetric stretching mode whose $\Delta\mu = 0$.

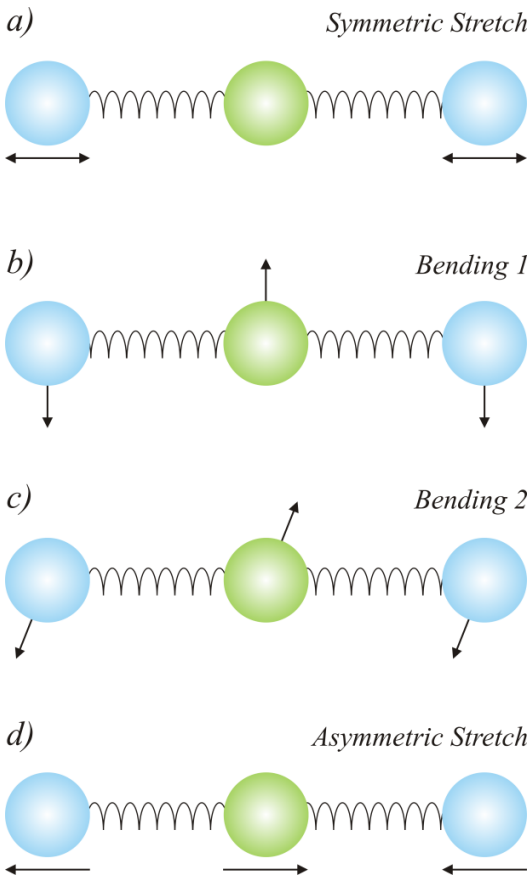

Figure 2.3 Vibrational modes of a triatomic molecule. Except for the symmetric stretching shown in (a), the rest vibrational modes (b) – (d) are all IR-active, as they involve changes in the dipole moment μ.

It can be concluded that only the vibrations that involve changes in the dipole moment are IR-active, and can thus be probed by IR spectroscopy. On the other hand, Raman-active vibrations must involve changes in the polarizability (reasons will be shown in section 2.3.2). Therefore, IR spectroscopy and Raman spectroscopy are spectroscopic techniques that provide complementary information on the molecular vibrations.

2.3 Raman Scattering

When light with a frequency ν_L is scattered by atoms or molecules, a strong Rayleigh scattering light with the same frequency ν_L can be observed. Besides, weak discrete spectral lines whose frequencies are shifted from the excitation frequency ν_L can also be observed. The latter effect is Raman scattering, which is in other words the inelastic scattering of photons. Raman scattering was discovered by C. V. Raman and K. S. Krishnan in liquids,[5] and by G. Landsberg and L. I. Mandelstam in crystals.[6] The amount of frequency shifts for the Raman scattering photon is related to the vibrational frequency of the molecule ν_m. A schematic of Raman scattering is shown by Figure 2.4.

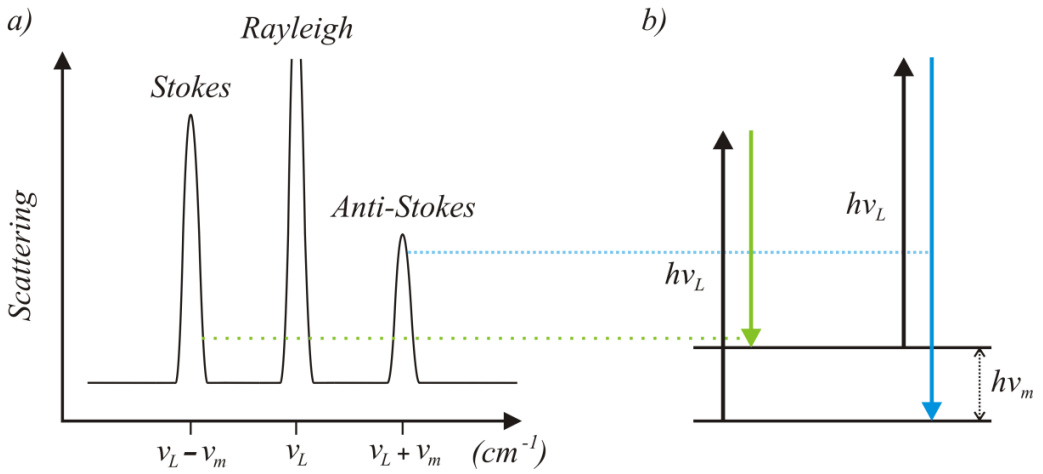

Figure 2.4 Schematic of Raman scattering. (a) An example of a Raman spectrum. The intensity of the anti-Stokes scattering is weaker than the Stokes scattering, since the vibrational excited state is populated by the Boltzmann distribution, and less molecules are available for an anti-Stokes process. (b) The Raman scatterings illustrated in the energy bands, correspond accordingly to the Stokes and the anti-Stokes peaks in (a).

It can be seen from Figure 2.4 that Raman photons can appear at either sides of the excitation wavelength, depending upon whether the incident photon interacts with a molecule on its vibrational ground state or on its vibrational excited state. The frequency of the Raman scattering photon can be expressed as either $\nu_L - \nu_m$ or $\nu_L + \nu_m$. In the former case, the incident photon interacts with a molecule on its vibrational ground state. Starting by exciting the molecule to a virtual state, the incident photon transfers energy of

$h\nu_m$ to the molecule to stimulate a vibration, and is scattered with a lower frequency $\nu_s = \nu_L - \nu_m$. Such a process is called Stokes scattering. For the latter case, the incident photon interacts with a molecule on an excited vibrational state. It first excites the molecule to a virtual state, absorbs energy of $h\nu_m$ to relax the molecule to the vibrational ground state, and is scattered with a higher frequency $\nu_{as} = \nu_L + \nu_m$. This process is called anti-Stokes scattering. Note that the vibrational excited states are populated following the Boltzmann distribution, thus at room temperature, the anti-Stokes scattering is weaker than the Stokes scattering since less molecules are available for an anti-Stokes process.

Raman spectroscopy is a spectroscopic technique to identify molecules by providing their vibrational fingerprints. The fundamental components of a Raman system are a laser which is the source of excitation, a notch filter which bypasses the signal of the Rayleigh scattering light, and a grating which resolves the Raman spectral lines. Due to the employment of lasers as excitation sources, handheld Raman systems can be produced to allow on-site identification of analytes with high signal-to-noise ratios and high spatial resolutions.[7] On the other hand, IR spectroscopy requires an excitation source that covers a wide spectral range, preferably a synchrotron light source if high signal-to-noise ratios and good spatial resolutions are needed. This, among other factors, has limited its applications.

Although Raman scattering light carries information about the vibrational states of the molecules, it has an extremely low intensity. The reason for this is that the frequency of the Raman excitation light is not in resonance with any molecular transitions. This leads to Raman cross sections for a molecule to be $\sim 10^{-30}$ cm^2/sr.[8] In comparison, fluorescence processes involve absorption and emission relative to molecular transitions, and the representative value for its cross section is $\sim 10^{-17}$ cm^2/sr.[9] The extremely low Raman cross sections prevent regular Raman spectroscopy from applications such as sensing trace amounts of molecules. To increase the Raman intensity, resonant Raman spectroscopy can be employed, in which the frequency of the excitation laser matches the electronic transition gap of the target molecule. To further boost the Raman signal, surface-enhanced Raman spectroscopy (SERS) should be used. The mechanism of the signal enhancement in SERS will be discussed in chapter 4.

2.4 Electromagnetic Interpretation of Raman Scattering

In this section, the physics behind Raman scattering is explained using the electromagnetic radiation theory. Consider light as electromagnetic radiation. It contains an electromagnetic field harmonically oscillating at a specific frequency ν_L. Such a field is able to give out electromagnetic radiation of the same frequency ν_L. Therein, the electric field can interact with a molecule through its polarizability, as polarizability describes the ability of a molecule to interact with an electric field to build a dipole moment. The amount of the induced dipole moment μ, which equals to the product of the polarizability of the molecule and the applied electric field, can be expressed as

$$\mu = \alpha E_0 \cos(2\pi \nu_L t) \tag{2.9}$$

where E_0 is the amplitude of the electric field, ν_L is the oscillating frequency of the electric field, and α is the polarizability of the molecule. For a harmonic vibration, the vibrational coordinate Q is

$$Q = Q_0 \cos(2\pi \nu_m t) \tag{2.10}$$

where ν_m is the vibrational frequency of the molecule, and Q_0 is the magnitude of the vibration. The polarizability α depends on the vibrational coordinate Q, thus

$$\alpha = \alpha(Q) \tag{2.11}$$

Equation 2.11 can be represented in a Taylor series

$$\alpha = \alpha_0 + \left(\frac{\partial \alpha}{\partial Q}\right)_0 Q_0 \cos(2\pi \nu_m t) \tag{2.12}$$

Since a harmonic approximation is used, the terms which involve powers of Q higher than first are neglected in equation 2.12. Replace α in equation 2.9 with equation 2.12, the induced dipole moment μ can then be written as

$$\mu = \alpha_0 E_0 \cos(2\pi v_0 t) + \left(\frac{\partial \alpha}{\partial Q}\right)_0 Q_0 E_0 \cos(2\pi v_m t) \cos(2\pi v_{\mathrm{L}} t) \tag{2.13}$$

Using the trigonometric identity

$$\cos\theta \cos\varphi = \frac{1}{2}[\cos(\theta + \varphi) + \cos(\theta - \varphi)] \tag{2.14}$$

The induced dipole moment μ is now

$$\mu = \alpha_0 E_0 \cos(2\pi v_{\mathrm{L}} t) + \frac{1}{2}\left(\frac{\partial \alpha}{\partial Q}\right)_0 Q_0 E_0 [\cos(2\pi v_s t) + \cos(2\pi v_{as} t)] \tag{2.15}$$

where v_{L}, $v_{\mathrm{s}} = v_{\mathrm{L}} - v_{\mathrm{m}}$, and $v_{\mathrm{as}} = v_{\mathrm{L}} + v_{\mathrm{m}}$ represents Rayleigh scattering, Stokes scattering and anti-Stokes scattering, respectively. Equation 2.15 shows that the induced dipole oscillates at three frequencies v_{L}, v_{s}, and v_{as}, and is capable of emitting light of these three frequencies: the Rayleigh scattering light whose frequency is the same as that of the applied electric field, the Stokes scattering light and the anti-Stokes scattering light, whose frequency is red- or blue shifted from that of the applied electric field, respectively. In addition, equation 2.15 shows that only those vibrational modes that change the polarizability of the molecule are Raman-active. In other words, the following condition must be fulfilled to trigger Raman scattering:

$$\frac{\partial \alpha}{\partial Q} \neq 0 \tag{2.16}$$

Furthermore, for a classical oscillator, its scattering radiation power is proportional to the fourth power of the frequency. If a Boltzmann factor is introduced to thermally populate the vibrational exited states of the molecules, the ratio of the scattering powers between Stokes scattering and anti-Stokes scattering can be written as

$$\frac{P_{Stokes}}{P_{anti-Stokes}} = \frac{(v_{\mathrm{L}} - v_m)^4}{(v_{\mathrm{L}} + v_m)^4 exp(-hv_m/\mathrm{k}T)} \tag{2.17}$$

It should be noted that the Boltzmann factor is not included in the electromagnetic model. A quantum mechanical treatment should be employed to strictly derive equation 2.17.[10]

In short, the physics behind Raman scattering can be explained as follows. The excitation light as an electromagnetic wave induces a dipole moment in the molecule. Since the polarizability is a function of the molecular vibrational coordinate, the induced dipole moment is modulated by the molecular vibration. Consequently, the induced dipole oscillates not only at the frequency of the excitation light, but also at two side bands, and therefore can radiate Rayleigh, Stokes and anti-Stokes scattering lights.[11]

References

[1] P. Atkins, J. de Paula, *Physical Chemistry for the Life Sciences*, *2nd Ed*. Oxford: Oxford University Press, **2011**.

[2] D. N. Sathyanarayana, *Vibrational Spectroscopy: Theory and Applications*, New Delhi: New Age International, **2004.**

[3] http://hyperphysics.phy-astr.gsu.edu/hbase/molecule/vibspe.html

[4] B. Stuart, *Infrared Spectroscopy: Fundamentals and Applications*, John Wiley & Sons, **2004.**

[5] C. V. Raman, *Indian J. Phys*. **1928**, *2*, 387.

[6] G. Landsberg, L. Mandelstam, *Naturwissenschaften* **1928**, *16*, 557.

[7] A. Hakonen, M. Svedendahl, R. Ogier, Z.-J. Yang, K. Lodewijks, R. Verre, T. Shegai, P. O. Anderssonb, M. Käll, *Nanoscale* **2015**, *7*, 9405.

[8] C. M. Penney, L. M. Goldman, M. Lapp, *Nature Physical science* **1972**, *235*, 110.

[9] L. Kastrup, S. W. Hell, *Angew. Chem. Int. Ed*. **2004**, *43*, 2.

[10] D. F. Walls, *Zeitschrift für Physik.* 1970, **237**, 224.

[11] S. K. Freeman, *Applications of laser Raman spectroscopy*. New York: Wiley, **1974**.

CHAPTER 3

LOCALIZED SURFACE PLASMON RESONANCE

Localized surface plasmon resonance is the resonant oscillation and redistribution of charges near the surfaces of metallic nanostructures. The resulting enhanced local optical field is the foundation of plasmon-supported spectroscopies, and is the key for localizing spectroscopic interactions within extremely small volumes. In this chapter, the basic optical properties of plasmonic structures are presented via the simplest plasmonic system — a metallic nanosphere. Following a systematic approach, the frequency dependent dielectric function of metals is first introduced using the Drude model. Next, the physics behind the localized surface plasmon resonance of a spherical metallic nanoparticle is explained.

3.1 Optical Properties of Bulk Metal

The optical properties of metals lie in their frequency dependent dielectric functions which are mainly determined by the free conduction electrons in metals. To explain the properties of electrical transportation in metals, Paul Drude proposed in 1900 the Drude model.[1, 2] Although the Drude model is an oversimplification, the DC or AC conductivity of a metal, respectively corresponding to the behavior of the electrical transportation under a static or an oscillating electric field, can be very well explained. In the following sections 3.1.1 and 3.1.2, the assumptions in the Drude model are employed to derive the conductivity of a metal. In section 3.1.3, the derived AC conductivity is applied in the Maxwell equations to reveal the dielectric function of metals, which can be used to explain the propagation of electromagnetic waves in metals.

3.1.1 DC Conductivity of Metal

The Drude model is an application of kinetic theory, assuming that the microscopic behavior of dense electrons in a solid may be treated with the kinetic theory of gas. The detailed assumptions are as follows. 1. Between collisions, each electron is treated as an independent and free electron, meaning that the effect of electron-electron interaction and electron-ion interaction is ignored. Subsequently, in the absence of an externally applied electromagnetic field, the electrons move along a straight line in between collisions with ions. In the presence of an externally applied electromagnetic field, Newton's law of motion governs the movement of the electrons in between collisions. 2. Only collisions between electrons and immobile ions are taken into consideration. A collision is regarded as an instantaneous event that alters the velocity of the involved electron. The mean free time between two adjacent collisions is τ, and thus the probability of a collision in a certain time period dt is dt/τ. Furthermore, τ is independent of the velocity and the position of the electron. 3. Electrons achieve thermal equilibrium only by collisions with ions. After one collision, an electron emerge at a random direction with its speed relating to the temperature of the region in which the collision happened, by $m_e v^2/2 = 3/2\mathrm{k}T$, where m_e is the mass of the electron.

Using the assumptions above, the DC conductivity of a metal can be derived. Consider using the Ohm's law

$$\mathbf{J} = \sigma \mathbf{E} \tag{3.1}$$

where **J** is the current density, σ is the conductivity and **E** is the electric field. Imagine an arbitrary electron. Let $\boldsymbol{v}_0$ be its velocity and t be the time elapsed since its last collision with an ion. In the presence of an externally applied DC electric field, after time t, its velocity can be written according to Newton's second law as

$$\boldsymbol{v} = \boldsymbol{v}_0 - \frac{e\mathbf{E}t}{m_e} \tag{3.2}$$

For a Drude system consisting of N electrons,

$$\mathbf{J} = -Ne\boldsymbol{v}_{avg} \tag{3.3}$$

where $\boldsymbol{v}_{avg}$ is the average velocity of the electrons. In such a system, *t* can be replaced by the mean free time τ to obtain the expression of $\boldsymbol{v}_{avg}$

$$\boldsymbol{v}_{avg} = \frac{\sum_{i=1}^{N} \boldsymbol{v}_{0i}}{N} - \frac{e\mathbf{E}\tau}{m_e}, \quad i \in [1, N], \quad i \in Z \tag{3.4}$$

Recall that in a Drude system the following assumption holds: an electron after a collision moves in a random direction. Therefore, the first term on the right side of equation 3.5 equals zero. Now substitute equation 3.4 into equation 3.3, the current density can then be expressed as

$$\mathbf{J} = \frac{Ne^2\tau}{m_e}\mathbf{E} \tag{3.5}$$

, and the DC conductivity is therefore

$$\sigma_0 = \frac{Ne^2\tau}{m_e} \tag{3.6}$$

3.1.2 AC Conductivity of Metal

Consider the response of an electron in a Drude system under an externally applied time-dependent AC electrical field:

$$\mathbf{E} = E_0 exp(-i\omega t) \tag{3.7}$$

According to law of conservation of momentum, the movement of the electron can be established as

$$\frac{d\boldsymbol{p}}{dt} = -\frac{\boldsymbol{p}}{\tau} - e\mathbf{E} \tag{3.8}$$

where $\boldsymbol{p} = m_e\boldsymbol{v}$ is the momentum. The solution of equation 3.8 is of the following form:

$$\boldsymbol{p} = p_0 exp(-i\omega t) \tag{3.9}$$

Replace $\boldsymbol{p}$ in equation 3.8 with equation 3.9, then the solution of equation 3.8 becomes

$$\boldsymbol{p} = \frac{e\tau}{i\omega\tau - 1}\mathbf{E} \tag{3.10}$$

Consider using the relationship between momentum $\boldsymbol{p}$ and current density **J**,

$$\mathbf{J} = -\frac{Ne\boldsymbol{p}}{m_e} \tag{3.11}$$

Substitute equation 3.10 into equation 3.11, **J** can be now expressed as

$$\mathbf{J} = \frac{Ne^2\tau}{m_e}\left(\frac{1}{1 - i\omega\tau}\right)\mathbf{E} \tag{3.12}$$

As can be seen, equation 3.12 is already in the form of the Ohm's law. Therefore, the AC conductivity is

$$\sigma = \frac{\sigma_0}{1 - i\omega\tau} \tag{3.13}$$

where σ_0 is the DC conductivity (see equation 3.6).

3.1.3 Dielectric Function of Metal

In this section, the frequency-dependent dielectric function of metals in the Drude model is derived to unveil the optical properties of metals. The derivation is done by applying the obtained AC conductivity in the Maxwell equations.

Assuming the metal is a nonmagnetic material with its net charge equaling zero, the Maxwell equations can be written as follows

$$\nabla \cdot \mathbf{E} = 0 \tag{3.14}$$

$$\nabla \cdot \mathbf{B} = 0 \tag{3.15}$$

$$\nabla \times \mathbf{E} = -\frac{\partial \mathbf{B}}{\partial t} \tag{3.16}$$

$$\nabla \times \mathbf{B} = \mu_0 \left(\sigma \mathbf{E} + \varepsilon_0 \frac{\partial \mathbf{E}}{\partial t} \right) \tag{3.17}$$

, where **E** and **B** is the electrical and magnetic field, respectively; ε_0 and μ_0 is the permittivity and permeability of free space, respectively; and σ is the conductivity. By applying the vector calculus identity below

$$\nabla \times \nabla \times \mathbf{E} = \nabla(\nabla \cdot \mathbf{E}) - \nabla^2 \mathbf{E} \tag{3.18}$$

, the following equality holds:

$$\nabla^2 \mathbf{E} = -\nabla \times \nabla \times \mathbf{E} = \frac{\partial}{\partial t}(\nabla \times \mathbf{B}) \tag{3.19}$$

Use the following relationship

$$\frac{1}{c^2} = \mu_0 \varepsilon_0 \tag{3.20}$$

where *c* is the speed of light in vacuum, and the dispersion relation below

$$k^2 = \frac{\omega^2}{c^2}\varepsilon(\omega) \tag{3.21}$$

where k is the wavenumber, and $\varepsilon(\omega)$ is the dielectric function, which is a function of frequency ω. Upon substitution, the following equation can be established

$$\nabla^2\mathbf{E} + \frac{\omega^2}{c^2}\left(1 + \frac{i\sigma}{\omega\varepsilon_0}\right)\mathbf{E} = 0 \tag{3.22}$$

It can be seen that equation 3.22 is exactly the time-harmonic wave equation with the form

$$\nabla^2\mathbf{E} + k^2\mathbf{E} = 0 \tag{3.23}$$

with a solution of the following form

$$\mathbf{E} = \mathbf{E}(x)exp(-i\omega t) \tag{3.24}$$

Therefore, the complex dielectric function of metal is

$$\varepsilon(\omega) = 1 + \frac{i\sigma}{\omega\varepsilon_0} \tag{3.25}$$

with σ being the AC conductivity in equation 3.13. To grasp some physical meaning behind the complex dielectric function of metal, consider working in a regime where $\omega\tau >> 1$, i.e. the electrons become collisionless, and replace σ in equation 3.25 with equation 3.13. To a first approximation, the dielectric function can be written as

$$\varepsilon(\omega) \approx 1 - \frac{{\omega_p}^2}{\omega^2} \tag{3.26}$$

where

$$\omega_p{}^2 = \sqrt{\frac{Ne^2}{\varepsilon_0 m_e}} \tag{3.27}$$

ω_p is called the plasma frequency of the electrons. The dispersion relation now becomes

$$k^2 \approx \frac{\omega^2}{c^2}\left(1 - \frac{\omega_p{}^2}{\omega^2}\right) \tag{3.28}$$

From equation 3.28, the optical properties of metal can be viewed in two regimes.

1. When $\omega < \omega_p$, k is purely imaginary. Therefore, the field decays exponentially with distance inside the metal.

2. When $\omega > \omega_p$, k is real, and the field propagates through the metal without decay, i.e. the metal is transparent to the electromagnetic wave.

In general, electromagnetic radiation at frequencies lower than the plasma frequency is reflected. Since metals exhibit plasma resonances in the UV range, visible lights are reflected.[3] This leads to the shining colors of bulk silver and gold.

3.2 Optical Properties of a Spherical Metallic Nanoparticle

Reducing the sizes of noble metals to the nanometer range, the metallic nanoparticles exhibit extraordinary optical properties as a consequence of their complex dielectric functions combined with their dimensions, shapes, compositions, and surrounding media. It has been known since Roman times, that by mixing gold colloids with glass or ceramics, the latter appears to have various colors. A classic example is the 'Lycurgus Cup' manufactured in the late Roman times. As can be seen from figure 3.1, the cup is ruby red in transmitted light and green in reflected light, due to the presence of gold colloids.[4]

Figure 3.1 The Lycurgus Cup. The cup shows the moment when Lycurgus is entrapped by the maenad Ambrosia in form of a vine. The cup is ruby red in transmitted light and green in reflected light, due to the presence of gold colloids.[4] Photo Credit: The Trustees of the British Museum / Art Resource, NY.

Such mysteries were not completely understood until Gustav Mie proposed the Mie theory which could exactly predict the optical responses of spheres.[5] In general, the reason for all those extraordinary optical properties of noble metallic nanostructures is that they support the so-called localized surface plasmon resonances (LSPR), which correspond to the oscillation and redistribution of charges near their surfaces. In this section, quasi-static approximation is first used to reveal the LSPR condition of an individual spherical nanoparticle. Then, the electrical field enhancement of the nanosphere is derived. It should be noted that the enhanced local optical fields due to LSPR is the foundation of plasmon-supported spectroscopies, and is the key for localizing spectroscopic interactions within extremely small volumes. Perhaps its most famous application is Surface-enhanced Raman Spectroscopy (SERS), which may boost the Raman scattering signal by a factor of $> 10^8$.[6]

3.2.1 Localized Surface Plasmon Resonance of a Spherical Metallic Nanoparticle

The simplest system that supports LSPR is a metallic nanosphere. A schemetic of its LSPR, i.e. the collective oscillations of free electrons near its surface, is shown in figure 3.2. The resulting optical response can be calculated analytically using the Mie theory.[5] Although the Mie theory gives the exact solutions of Maxwell equations, the easiest way to understand the optical properties of a metallic nanosphere is by using the

quasi-static approximation, which is valid when the size of the sphere is much smaller than the wavelength ($a << \lambda$), i.e., the retardation effect can be neglected.

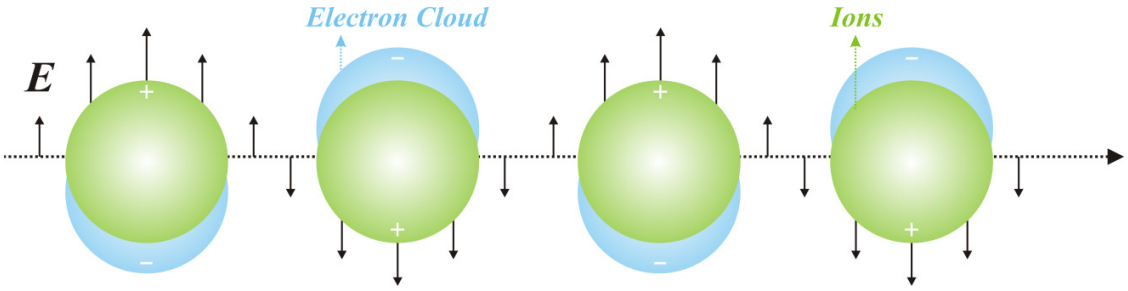

Figure 3.2. A schemetic of the LSPR in a spherical metallic nanoparticle, driven by an oscillating electrical field, which essentially induces the collective oscillations of free electrons near the surface of the nanoparticle.

The quasi-static approximation assumes that all points of an object respond simultaneously to the incoming field. Therefore, to obtain the optical response, one calculates the spatial field distribution under an electrostatic field, i.e. the Maxwell equations are replaced by the Laplace equation of electrostatics, and the frequency-dependent components are later added to the solutions. Consider an isotropic sphere in an arbitrary medium, illustrated in figure 3.3.

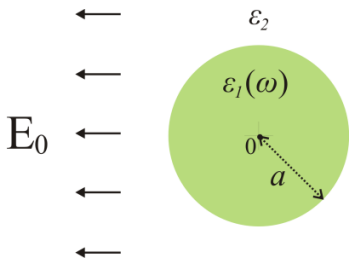

Figure 3.3 Quasi-static model of a spherical metallic nanoparticle, which is placed in an arbitrary medium, and experiences an electrostatic field. The origin of coordinates is at the center of the spherical nanoparticle.

To reveal the optical response of the sphere under the quasi-static approximation, one solves the Laplace equation

$$\nabla^2 \Phi = 0 \tag{3.29}$$

In spherical coordinates, equation 3.29 becomes

$$\frac{1}{r^2}\frac{\partial}{\partial r}\left(r^2 \frac{\partial \Phi}{\partial r}\right) + \frac{1}{r^2 \sin\theta}\frac{\partial}{\partial \theta}\left(\sin\theta \frac{\partial \Phi}{\partial \theta}\right) + \frac{1}{r^2 \sin\theta}\left(\frac{\partial^2 \Phi}{\partial \varphi^2}\right) \tag{3.30}$$

where

$$\Phi = \Phi(r, \theta, \varphi) \tag{3.31}$$

Assume that Φ_1 is the potential inside the sphere, and Φ_2 is the potential outside the sphere with $\Phi_2 = \Phi_s + \Phi_0$, in which Φ_s is the scattering potential, and Φ_0 is the potential relating to the homogeneous electrical field along the *x*-direction in the medium. Φ_0 can be expressed by

$$\Phi_0 = -\mathrm{E}_0 x = -\mathrm{E}_0 r\cos\theta \tag{3.32}$$

where E_0 is the amplitude of the applied electric static field. Now, the boundary conditions can be expressed as

$$\left.\frac{\partial \Phi_1}{\partial \theta}\right|_{r=a} = \left.\frac{\partial \Phi_2}{\partial \theta}\right|_{r=a} \tag{3.33}$$

$$\varepsilon_1 \left.\frac{\partial \Phi_1}{\partial r}\right|_{r=a} = \varepsilon_2 \left.\frac{\partial \Phi_2}{\partial r}\right|_{r=a} \tag{3.34}$$

Equation 3.33 and 3.34 correspond to the continuity of the tangential and normal component of the electrical field and the electrical displacement at the surface of the sphere, respectively. The potentials below satisfy the Laplace equation and the boundary conditions:

$$\Phi_1 = -\mathrm{E}_0 \frac{3\varepsilon_2}{\varepsilon_1 + 2\varepsilon_2} r\cos\theta \tag{3.35}$$

$$\Phi_2 = -\mathrm{E}_0 r\cos\theta + \mathrm{E}_0 \frac{\varepsilon_1 - \varepsilon_2}{\varepsilon_1 + 2\varepsilon_2} a^3 \frac{\cos\theta}{r^2} \tag{3.36}$$

Note that the second term in equation 3.36 equals Φ_s, which is the potential related to the scattering field. This potential is identical to that of an ideal dipole at the center of the sphere:

$$\Phi_{\mathrm{dipole}} = \frac{\mu}{4\pi\varepsilon_2} \frac{\cos\theta}{r^2} \tag{3.37}$$

Since the dipole moment is given by

$$\boldsymbol{\mu} = \varepsilon_2 \alpha \mathbf{E}_0 \tag{3.38}$$

Upon substitution, the polarizability of the sphere is therefore

$$\alpha = 4\pi a^3 \frac{\varepsilon_1 - \varepsilon_2}{\varepsilon_1 + 2\varepsilon_2} \tag{3.39}$$

From equation 3.39, it can be seen that when $\mathrm{Re}[\varepsilon_1(\omega)] = -2\varepsilon_2$, the polarizability can receive a resonant enhancement, i.e. the LSPR mode of the metallic nanosphere can be excited. It is worth noting that the resonance condition is wavelength dependent, since the complex permittivity of metal is a function of wavelength, as has been discussed in section 3.1. Furthermore, the resonance wavelength is related to the dielectric environment surrounding the metallic sphere. This is the foundation of using metallic nanoparticles as refractive index sensors.[7]

3.2.2 Field Enhancement near a Spherical Metallic Nanoparticle

The spectroscopic applications of LSPR-supportive nanostructures, e.g. SERS, utilize the highly confined and enhanced electromagnetic fields appearing near the surfaces of these structures. In this section, the basic properties of the enhanced local optical fields are inferred from the already established quasi-static model of a spherical metallic nanoparticle in section 3.2.1.

By applying

$$\mathbf{E} = -\nabla\Phi \tag{3.40}$$

to the potentials in equations 3.35 and 3.36, the electrical field inside and outside the sphere can be obtained respectively:

$$\mathbf{E}_1 = \mathrm{E}_0 \frac{3\varepsilon_2}{\varepsilon_1 + 2\varepsilon_2} \boldsymbol{e}_x \tag{3.41}$$

$$\mathbf{E}_2 = \mathrm{E}_0 \boldsymbol{e}_x + \mathrm{E}_0 \frac{\varepsilon_1 - \varepsilon_2}{\varepsilon_1 + 2\varepsilon_2} \frac{a^3}{r^3} (2\cos\theta\, \boldsymbol{e}_r + \sin\theta \boldsymbol{e}_\theta) \tag{3.42}$$

where $\boldsymbol{e}_x$, $\boldsymbol{e}_r$, and $\boldsymbol{e}_\theta$ are unit vectors. Note that $\mathbf{E}_1$ and $\mathbf{E}_2$ are independent of the azimuthal angle φ as a result of the symmetry implied by the applied field. The second term in equation 3.42 corresponds to the scattering field $\mathbf{E}_{\mathrm{sc}}$ of the sphere. Since the field near the surface of the sphere relating to the LSPR is of interest, it is reasonable to define

$$\mathrm{g} = \frac{|\mathbf{E}_{\mathrm{sc}}|}{|\mathbf{E}_0|} = \left|\frac{\varepsilon_1 - \varepsilon_2}{\varepsilon_1 + 2\varepsilon_2}\right| \cdot |2\cos\theta\, \boldsymbol{e}_r + \sin\theta \boldsymbol{e}_\theta| \cdot \frac{a^3}{r^3} \tag{3.43}$$

as the electrical field enhancement factor. Equation 3.43 indicates the following: 1. At the LSPR wavelength, i.e. $\mathrm{Re}[\varepsilon_1(\omega)] = -2\varepsilon_2$, the field near the surface of the sphere receives the strongest enhancement; 2. The enhanced field is particularly strong for a small $\mathrm{Im}[\varepsilon_1(\omega)]$, which indicates small damping of surface plasmons; 3. The field enhancement under the LSPR condition has its strong maximums along the *x*-axis, i.e. when $\theta = 0$ or π; 4. The field enhancement significantly decreases with increased distance

away from the metallic sphere, i.e. g $\propto 1/r^3$. This means that the field is highly confined in the vicinity of the metal. This is also the reason why the spectroscopic applications using LSPR-supportive structures have the prefix 'surface-enhanced' in their names — the enhanced fields only interact with analytes in the small confined volume near the surfaces of these structures.

References

[1] P. Drude, *Annalen der Physik* **1900**, *306*, 566.

[2] P. Drude, *Annalen der Physik* **1900**, *308*, 369.

[3] P. R. West, S. Ishii, G. V. Naik1, N. K. Emani, V. M. Shalaev, A. Boltasseva, *Laser Photonics Rev.* **2010**, *4*, 795.

[4] M. C. Daniel, D. Astruc, *Chem. Rev.* **2004**, *104*, 293.

[5] G. Mie, *Ann. Phys.***1908**, *25*, 377.

[6] E. C. Le Ru, P. G. Etchegoin, *Annu. Rev. Phys. Chem.* **2012**, *63*, 65.

[7] T. Rindzevicius, *Nanoplasmonic Structures for Bio/Chemo Sensing*. Göteborg: Chalmers University of Technology, **2006.**

CHAPTER 4

SURFACE ENHANCED RAMAN SPECTROSCOPY

Surface-enhanced Raman Spectroscopy (SERS) is the phenomenon that significantly increased Raman scattering signals are probed from molecules attached to or in the very close vicinity of metallic nanostructures. It is a prominent spectroscopic application of the highly confined and enhanced optical fields near the surfaces of LSPR-supportive nanostructures. Due to the strongly increased signals which compensate the extremely low Raman scattering cross sections, SERS transforms Raman spectroscopy from a tool for structural analysis to a nanoscale sensing probe, with lowest detection limits down to single molecular levels.[1] In this chapter, the mechanism of the signal enhancement in SERS is first described. Next, the general requirements of plasmonic structures for reliable and quantitative SERS analyses are discussed.

4.1 Enhancement Mechanisms of Surface-enhanced Raman Scattering

Since Raman scattering is a two-photon process, the intensity of the Stokes scattering signal of SERS can be estimated according to

$$I_{\mathrm{SERS}}(v_{\mathrm{s}}) = N\sigma'_{\mathrm{RS}}|\mathrm{g}(v_{\mathrm{L}})|^2|\mathrm{g}(v_{\mathrm{s}})|^2 I(v_{\mathrm{L}}) \tag{4.1}$$

where N is the number of molecules, σ'_{RS} is the Raman cross section of the adsorbed molecule on the surface of the metal, $\mathrm{g}(v_{\mathrm{L}})$ and $\mathrm{g}(v_{\mathrm{s}})$ is the electrical field enhancement factor at the excitation wavelength and at the Stokes wavelength respectively, and $I(v_{\mathrm{L}})$ is the intensity of the excitation laser. Note that equation 4.1 is based on estimation, which assumes that all the molecules are independently sitting in the same chemical environment, and are experiencing an identical excitation field. Although this is an oversimplification, equation 4.1 can help to reveal the basic mechanisms of the signal

enhancement in SERS. Specifically, there are two mechanisms that account for the total SERS enhancement, namely the 'chemical enhancement' and the 'electromagnetic enhancement'.[2]

The chemical enhancement of the Raman signal lies in the Raman cross section of the adsorbed molecule σ'_{RS}, which may be viewed as of ~10 – 100 times higher than σ_{RS}, which is the Raman cross section of the same molecule unattached to a surface. The chemical enhancement effect is related to the electronic interactions between the molecule and the metal, which can induce resonance Raman scattering conditions by introducing new, or shifting electronic levels of the adsorbed molecules.[3] These electronic interactions require close contact between the molecules and the metal, and are molecular dependent.

The electromagnetic enhancement of the Raman signal is reflected by the terms $|\mathrm{g}(v_{\mathrm{L}})|^2|\mathrm{g}(v_{\mathrm{s}})|^2$ in equation 4.1, and is caused by the enhanced local optical fields. Its detailed procedure is as follows. An enhanced local optical field appears near the LSPR-supportive nanostructure when the frequency of the excitation laser is in resonance with that of the LSPR. The enhanced field then induces an oscillating dipole in the molecule. This dipole emits light of three frequencies: the Rayleigh scattering light whose frequency is the same as that of the applied field, the Stokes and the anti-Stokes scattering light, whose frequency is red- or blue shifted by the molecular vibrational frequency v_{m} (see equation 2.15). The Stokes radiation is also enhanced by the LSPR effect, leading to a total enhancement of $|\mathrm{g}(v_{\mathrm{L}})|^2|\mathrm{g}(v_{\mathrm{s}})|^2$ in its intensity (to a first-order approximation[4]). Since v_{L} and v_{s} are usually much higher than v_{m}, it is reasonable to assume that $v_{\mathrm{L}} \approx v_{\mathrm{s}}$. Therefore,

$$I_{\mathrm{SERS}}(v_{\mathrm{s}}) \propto |\mathrm{g}(v_{\mathrm{L}})|^4 \tag{4.2}$$

Equation 4.2 represents the well-known E^4 enhancement of SERS, i.e. the electromagnetic SERS enhancement factor is proportional to the electrical field enhancement factor to the power of four. In the case of a metallic nanosphere, $\mathrm{g}(v_{\mathrm{L}})$ can be replaced by equation 3.43, leading to

$$I_{\mathrm{SERS(sphere)}}(v_{\mathrm{s}}) \propto \left|\frac{\varepsilon_1(v_{\mathrm{L}}) - \varepsilon_2}{\varepsilon_1(v_{\mathrm{L}}) + 2\varepsilon_2}\right|^4 \cdot \left(\frac{a}{r}\right)^{12} \tag{4.3}$$

Although equation 4.3 is based on a simple individual sphere model, it describes the most important properties of the electromagnetic SERS effect. It can be seen from equation 4.3 that the SERS signal is strongly dependent on the distance between the molecule and the metal. In other words, the electromagnetic SERS enhancement does not require direct contact between the molecule and the metal, and the distance dependence of the electromagnetic enhancement factor is proportional to $1/r^{12}$. In addition, equation 4.3 shows that the enhancement is particularly strong when the frequency of the excitation laser is in resonance with the LSPR frequency, i.e. $\mathrm{Re}[\varepsilon_1(v_{\mathrm{L}})] = -2\varepsilon_2$. Due to the electromagnetic enhancement of the SERS signal, the regions near the metallic nanostructures in which strongly enhanced local optical fields exist are called 'hot spots'.[5]

In general, the total SERS enhancement factor $\mathrm{EF_{SERS}}$ can be viewed as the product of the chemical SERS enhancement factor $\mathrm{EF_{CHEM}}$ and the electromagnetic SERS enhancement factor $\mathrm{EF_{EM}}$, with

$$\mathrm{EF_{SERS}} = \mathrm{EF_{CHEM}} \times \mathrm{EF_{EM}} \tag{4.4}$$

$$\mathrm{EF_{CHEM}} = \sigma'_{\mathrm{RS}}/\sigma_{\mathrm{RS}} \tag{4.5}$$

$$\mathrm{EF_{EM}} = |\mathrm{g}(v_{\mathrm{L}})|^2 |\mathrm{g}(v_{\mathrm{s}})|^2 \tag{4.6}$$

It should be noted that the characteristic of $\mathrm{EF_{EM}}$ is 'general', as it is provided by the plasmonic nanostructures via the enhanced local optical fields. On the other hand, $\mathrm{EF_{CHEM}}$ is 'specific', since its intensity is molecular dependent. In addition, $\mathrm{EF_{EM}}$ can be predicted quite well by solving Maxwell equations, while there is no classical theory to predict $\mathrm{EF_{CHEM}}$. To predict $\mathrm{EF_{CHEM}}$, one requires a full quantum mechanical treatment, which is extremely difficult to realize.

4.2 Requirement in Plasmonic Systems for Surface-enhanced Raman Spectroscopy

In general, ideal plasmonic systems for reliable and quantitative SERS analyses should fulfill the three requirements below.[7, 8]

1. The system should exhibit a high and spatially uniform electromagnetic enhancement factor EF_{EM}. To sense analytes of small quantities, a high EF_{EM} is essential to increase the Raman signal, which scales with EF_{EM} to the power of four, as has been shown in section 4.1. Additionally, a more spatially uniform EF_{EM} would enable quantitative SERS analyses. To quantify a single molecule, molecules should experience a same EF_{EM} despite their locations relative to the LSPR structure. However, in reality, EF_{EM} is dependent on the detailed surface morphologies of the LSPR structures, and can vary by several orders among different regions. Nevertheless, one should strive to achieve a more spatially uniform EF_{EM} to improve SERS uniformity and reproducibility, as application-wise it is not always necessary to reach a quantification level down to single molecules.[9] Due to the non-uniform nature of the local optical fields, in practical use, the average total enhancement factor EF_{AVG} is measured experimentally to assess the performance of a SERS system. EF_{AVG} can be described by:

$$\mathrm{EF_{AVG}} = \frac{[I_{\mathrm{SERS}}/N_{\mathrm{Surf}}]}{[I_{\mathrm{RS}}/N_{\mathrm{Vol}}]} \tag{4.7}$$

where I_{SERS} is the measured SERS intensity, N_{Surf} is the number of molecules bound to the enhancing SERS-active structure, I_{RS} is the measured Raman intensity without enhancement, and N_{Vol} is the number of molecules in the excitation volume for measuring I_{RS}.[10,11] To characterize the uniformity of EF_{EM}, SERS scans/mappings over certain distances/areas are usually performed on the SERS-active structure, with different quantities of analytes bound to its surface. The relative standard deviations of pronounced SERS peaks then reflect the spatial uniformity of EF_{EM} for such a structure.

2. The system should exhibit widely tunable LSPR wavelengths. This is mainly because resonant surface-enhanced Raman scattering (SERRS) takes place when the excitation wavelength is in resonance with the absorption wavelength of the analyte. SERRS can provide additional Raman signal enhancement of ~10^2.[12]

3. The system should be easy to fabricate in a reproducible manner. This requirement has been achieved extensively thanks to the rapid development of nanofabrication techniques.[8] In terms of nanofabrication, the majority of produced SERS systems are either (i) metallic nanoparticles in colloidal suspensions, or (ii) nanostructured solid substrates. Representative examples of SERS systems can be found in chapter 1, section 1.1, 'State-of-the-art Plasmonic Systems for Surface-enhanced Raman Spectroscopy'.

References

[1] K. Kneipp, Y. Wang, H. Kneipp, L. T. Perelman, I. Itzkan, R. R. Dasari, M. S. Feld, *Phys. Rev. Lett.* **1997**, *78*, 1667.

[2] K. Kneipp, *Phys. Today* **2007**, 40.

[3] J. R. Lombardi, R. L. Birke, T. Lu, J. Xu, *J. Chem. Phys.* **1986**, *84*, 4174.

[4] G. C. Schatz, R. P. Van Duyne, *Handbook of Vibrational Spectroscopy*, Chichester: John Wiley & Sons, **2002.**

[5] H. Wei, H. Xu, *Nanoscale*, **2013**, *5*, 10794.

[6] E. C. Le Ru, P. G. Etchegoin, *Annu. Rev. Phys. Chem.* **2012**, *63*, 65.

[7] B. Sharma, M. F. Cardinal, S. L. Kleinman, N. G. Greeneltch, R. R. Frontiera, M. G. Blaber, G. C. Schatz, R. P. Van Duyne, *MRS Bulletin* **2013**, *38*, 615.

[8] S. Schlücker, *Angew. Chem. Int. Ed.* **2014**, *53*, 4756.

[9] R. K. Lauridsen, T. Rindzevicius, S. Molin, H. K. Johansen, R. W. Berg, T. S. Alstrøm, K. Almdal, F. Larsen, M. S. Schmidt, A. Boisen, *Sens. Biosens.* **2015**, *5*, 84.

[10] A. D. McFarland, M. A. Young, J. A. Dieringer, R. P. Van Duyne, *J. Phys. Chem. B* **2005**, *109*, 11279.

[11] R. P. Van Duyne, *Chem. Biochem. Appl. Lasers* **1979**, *4*, 101.

[12] C. L. Haynes, R. P. Van Duyne, *J. Phys. Chem. B* **2003**, *107*, 7426.

CHAPTER 5

NANOPILLAR ARRAYS FOR SURFACE-ENHANCED RAMAN SPECTROSCOPY

This chapter introduces the research subject of the Ph.D. study — the metal-capped Si nanopillar arrays (NPs) for surface-enhanced Raman spectroscopy (SERS). Specifically, these NPs are fabricated by a lithography-free process, which was developed by Senior Researcher Michael Stenbæk Schmidt in the Nanoprobes group at DTU Nanotech. [1] Section 5.1 describes the lithography-free fabrication process to obtain the NPs. It is a two-step process, which consists of maskless reactive etching of Si, followed by E-beam evaporation of noble metals. Section 5.2 demonstrates the most important mechanism of the NPs qualifying them to be used for SERS — leaning. Via leaning, clusters of NPs form, and hot spots with strong local optical fields are created in the gap junctions among the NPs.

5.1 Large-area Fabrication of Nanopillars by Lithography-free Processes

The fabrication of the NPs is carried out in DTU Danchip. The following two-step process is employed to fabricate NPs. (i) Starting from a 4-inch or 6-inch Si wafer, standing vertical Si pillars is first produced by maskless reactive ion etching, and (ii) NPs are fabricated by subsequently coating the Si pillars with either silver or gold using e-beam evaporation. Figure 5.1 shows a schematic of the process.

The most distinguishing feature of the process is that it involves no lithography processes, which are lengthy and expensive, yet wafer-scale NPs are produced. Omitting lithographic steps significantly reduces the processing time, and hence can make the SERS NP substrates cheap consumables.

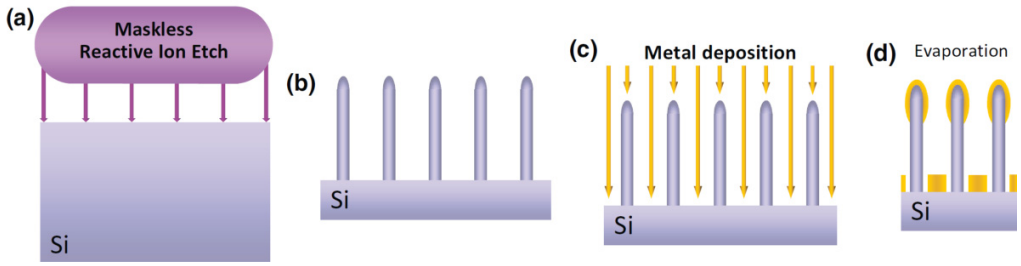

Figure 5.1 Process flow. (a) Maskless reactive ion etching forms Si nanopillars (b) and (c) Ag is deposited by electron beam evaporation onto the Si nanopillars to form SERS-active substrates. (d) Evaporation results in Ag lumps at the top of the Si pillars. Adapted from reference [1].

SEM image of the fabricated Ag capped Si NPs before and after leaning are shown in Figures 5.2 (e) – (g). It can be seen from Figure 5.2 (e) and (f) that a metal film with nanoholes is formed along with the NPs after e-beam evaporation. In addition, the fabricated NPs all have the same height. For SERS applications, it is crucial that the NPs have a uniform height so that after they lean towards their nearest neighbors, the intensity of the localized near fields are more spatially uniform.

5.2 Clustering of Nanopillars and Formation of Hot Spots

A high electromagnetic field enhancement factor is the prerequisite for a plasmonic system to be used for SERS. For the NPs, this is achieved by strong plasmonic couplings via the gap junctions between the metallic caps after leaning of NPs. The mechanism of leaning is shown in Figure 5.2 (a) - (c).

Besides the mechanism of leaning, Figure 5.2 (a) - (c) demonstrates also the workflow of gas sensing using the SERS-active NPs. When the NPs are exposed to analytes in gas phase, the analytes can adsorb onto the metallic caps of the NPs. After clustering of NPs via dipping and evaporation of solvent, those analytes that sit inside/near the hot spots, i.e. the gap junctions between the caps of NPs, can radiate strongly enhanced Raman signals and are thus detectable. In a slightly different way, in

the case of sensing analytes in liquid, the solvent containing analytes is deposited onto the NPs, and the adsorption of the analytes to the NPs takes place on the wet NPs.

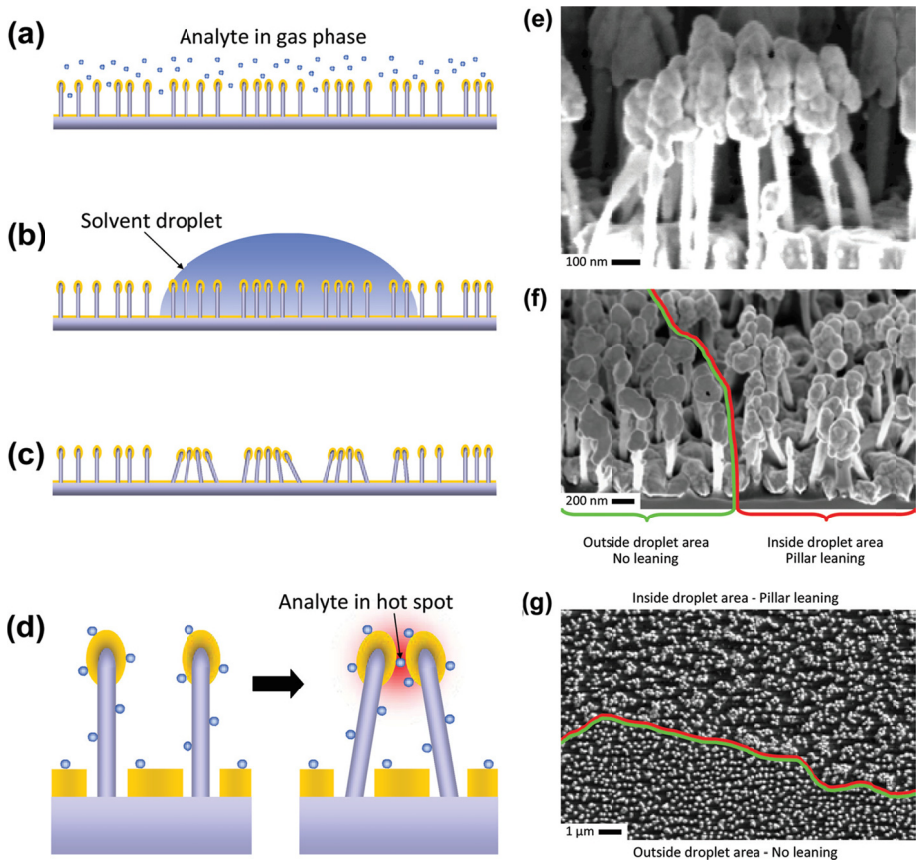

Figure 5.2 Concept of the leaning NP substrate. (a) – (c), Schematic of the leaning mechanism. (d) Schematic of hypothesized enhancement mechanism. When the solvent evaporates, surface tension will pull the Si nanopillars together, trapping the analyte at the hot spot giving rise to a large Raman signal. (e) SEM image of a cluster of leaning Ag capped Si NPs. (f) Tilted SEM image of the outer perimeter of the evaporated solvent droplet area. The NPs to the right have leaned to form hot spots while the NPs to the left remain vertical and free standing. (g) SEM image of NP surface seen perpendicular to the surface. The line indicates the outer perimeter of the evaporated solvent droplet. Bottom: individual freestanding NPs. Top: clusters of NPs have formed. Adapted from reference [1].

The key features of the SERS NPs can be summarized below: (i) their fabrication process is wafer-scale, and does not involve any lithographic steps. Such a process is fast and cost-effective, thus allowing the produced substrates to be used as cheap and

expendable consumables, (ii) their SERS hot spots are formed by clustering, and are located at the gap junctions between the leaning NPs. The ability for the NPs to lean towards their neighbors and create hot spots with strong local optical fields qualifies them for an effective SERS-based sensor.

In the next three chapters, the original findings regarding the SERS-active NPs in the Ph.D. project are presented. Chapter 6 exhibits an in-depth study on the LSPR properties of the NPs, via numerical simulations and dark-field scattering measurements. Based on the strength of the theoretical understandings presented in Chapter 6, Chapter 7 focuses on experimentally improving the electromagnetic EF and the SERS background signals of the NPs, via systematic evaluations of the related procedures. Chapter 8 presents the up-to-date engineering results of the nanopillar arrays. It shows that by carefully optimizing the fabrication process, it is possible to significantly increase the density of the NPs. As a result, a large-scale, highly uniform, and highly efficient SERS substrate is obtained.

References

[1] M. S. Schmidt, J. Hübner, A. Boisen, *Adv. Mater.* **2012**, *24*, OP11.

CHAPTER 6

PLASMON RESONANCES OF AG CAPPED SI NANOPILLARS FABRICATED USING MASK-LESS LITHOGRAPHY [P1]

Kaiyu Wu,[1,*] Tomas Rindzevicius,[1] Michael Stenbæk Schmidt,[1]
Klaus Bo Mogensen,[1] Sanshui Xiao[2], and Anja Boisen[1]

[1]Department of Micro- and Nanotechnology, Technical University of Denmark, 2800 Kongens Lyngby, Denmark
[2]Department of Photonics Engineering, Technical University of Denmark, 2800 Kongens Lyngby, Denmark
*kaiwu@nanotech.dtu.dk

Published in
Opt. Express **2015**, *23*, 12965 – 12978
doi: 10.1364/OE.23.012965

Localized surface plasmon resonances (LSPR) and plasmon couplings in Ag capped Si Nanopillar (Ag NP) structures are studied using 3D FEM simulations and dark-field scattering microscopy. Simulations show that a standalone Ag NP supports two LSPR modes, i.e. the particle mode and the cavity mode. The LSPR peak position of the particle mode can be tuned by changing the size of the Ag cap, and can be hybridized by leaning of pillars. The resonance position of the cavity resonance mode can be tuned primarily via the diameter of the Si pillar, and cannot be tuned via leaning of Ag NPs. The presence of a substrate dramatically changes the intensity of these two LSPR modes by introducing constructive and destructive interference patterns with incident and reflected fields. Experimental scattering spectra can be interpreted using theoretical simulations. The Ag

NP substrate displays a broad plasmonic resonance band due to the contribution from both the hybridized particle LSPR and the cavity LSPR modes.

1 Introduction

Plasmonic nanostructures [1,2] are the key components for extensive applications such as surface-enhanced Raman Scattering (SERS) [3-5], refractive index sensing [6-8], surface-enhanced infrared absorption (SEIRA) [9,10], plasmonic optical devices [11,12] and thermal sensing [13], due to their ability to controllably confine light energy at the nanoscale. For sensing applications based on localized surface plasmon resonance (LSPR), emphasis has been drawn on the development of nanostructures exhibiting high and uniform field enhancement factors (EF), wide range and controllable plasmonic tunability, suitableness for mass-production, and reproducibility. Typical examples include nanoshells [14, 15], highly faceted nanoparticles [16, 17], nanopillars [18-20], and structured substrates [21-23].

Recently, a new class of Si pillar based nanoplasmonic structures fabricated using mask-less reactive ion etching has been developed [24, 25]. It consists of free standing Si nanopillars capped by Ag or Au films, as shown in Fig. 1(c). Such SERS substrates exhibit high and uniform EF and can effectively trap analyte molecules near the electromagnetic hot-spots via leaning of pillars. Substrate application examples include detection of TAMRA-labeled vasopressin molecules in ultra-low concentrations, and characterization of biologically relevant diphenylalanine nanotube-folic acid conjugates, revealing its potential for bioanalytical quantifications of complex biological samples [26, 27]. Most importantly, the fabrication of such substrates is extremely simple, quick, cost-effective and is suitable for mass production. The fabrication process can be completed in 15 minutes. Mask-less reactive ion etching (RIE) is used to form Si pillars with controllable height and density over an entire 4 inch wafer, and then Ag or Au caps can be deposited onto the Si pillars by e-beam evaporation. Despite the reported substrate applications, to the best of our knowledge there are no previous theoretical or experimental reports that address the LSPR behavior of Au/Ag nanopillars fabricated using mask-less lithography. In order to open new possibilities for optimizing the

substrate towards a multifunctional plasmonic sensing platform that fulfills all the requirements of an ideal LSPR substrate, optical properties of isolated and interacting Au/Ag nanopillars need to be systematically investigated. To carry out such a study, a major challenge is that the geometry of the fabricated nanopillars varies from pillar to pillar significantly. This is due to the mask-less Si RIE process which cannot be precisely controlled to obtain Si nanopillar structures with a sub-10 nanometer resolution. In order to simulate experimentally observed optical properties of such nanopillar structures, representative pillar geometries observed by scanning electron microscopy (SEM) should be carefully selected. Due to similarities in the pillar geometry, a single pillar or a dimer of pillars can be modeled using the aforementioned method. Although we acknowledge that it is an approximate approach, a valuable theoretical insight into otherwise a quite complicated nanopillar structure can be obtained.

In this paper, LSPR properties of Ag capped nanopillars (NPs) are studied using 3D FEM simulations, and the results are then verified experimentally. Following a step-by-step approach, LSPR modes of a standalone NP are first simulated and investigated. Two basic LSPR modes, the particle mode and the cavity mode are observed. The particle mode is the collective electron oscillations in the Ag cap. It can be distinguished by the enhanced localized fields around the center of the Ag cap. Its resonant wavelength can be red-shifted by increasing the Ag cap size or the Si pillar diameter, and by flattening the Si pillar tip. The cavity mode is the electron oscillations in the Ag cap coupled via the Si pillar. It can be distinguished from the enhanced and highly localized fields near the neck of the Ag cap. Its wavelength is dominant by the diameter of the Si pillar. The influence of the substrate is also investigated. The substrate is shown to have a strong influence on the intensity of the LSP resonance of the NP, by introducing constructive or destructive interference to the excitation light; however, it has only minor effect on tuning of the LSPR modes. Then, leaning of the NPs are studied by simulating a NP dimer. Results show that the particle mode hybridizes when two NPs lean together, splitting into various LSPR modes, with increased EFs by ~3 - 4 times. Contrary to what happens to the particle mode, leaning of the NPs does not change the cavity LSPR wavelength at all. Finally, scattering measurements are performed on real samples.

Experimental results can be interpreted in light of the conclusions drawn from the simulations. This proves the validity of the numerical approximations and analysis.

2 Simulation Model

3D FEM simulations are performed using the commercial software COMSOL MULTIPHYSICS ver. 4.4a. Figs. 1(a) and 1(b) show the geometry of a single NP in the model. Such geometry is established according to the NPs observed in the SEM images, as shown in Figs. 1(c) and 1(d). In the model, an ellipsoid with a rounded bottom (r = 5 nm) and a cone are used to approximate the metal cap and the tip of the Si pillar, respectively. Unless otherwise noted, the substrate is excluded from the simulation to reduce computation time. If not mentioned, default values of the geometric parameters described in the caption of Fig. 1 are used in the simulation. Ag, Au and Si are modeled by their complex refractive indices as functions of wavelength [28]. The medium surrounding the NP is set to vacuum. The excitation plane wave propagates along the –z direction, where the electrical field is polarized along the x-axis.

In all cases, we calculate the scattering cross-section of the NP(s) using Eq. 1,

$$\sigma_{sca} = \frac{1}{I_0} \iint \mathbf{n} \cdot \mathbf{S}_{\mathbf{sc}} dS \tag{1}$$

where I_0 is the excitation intensity, $\mathbf{n}$ is the normal vector pointing outwards the closed surface of the NP_S and $\mathbf{S}_{\mathbf{sc}}$ is the poynting vector of the scattered light. The electromagnetic field distribution is calculated by setting the excitation field as the background field followed by solving the scattered fields multiple times. A perfect matched layer with scattering boundary conditions on its outer boundaries is employed to eliminate non-physical reflections.

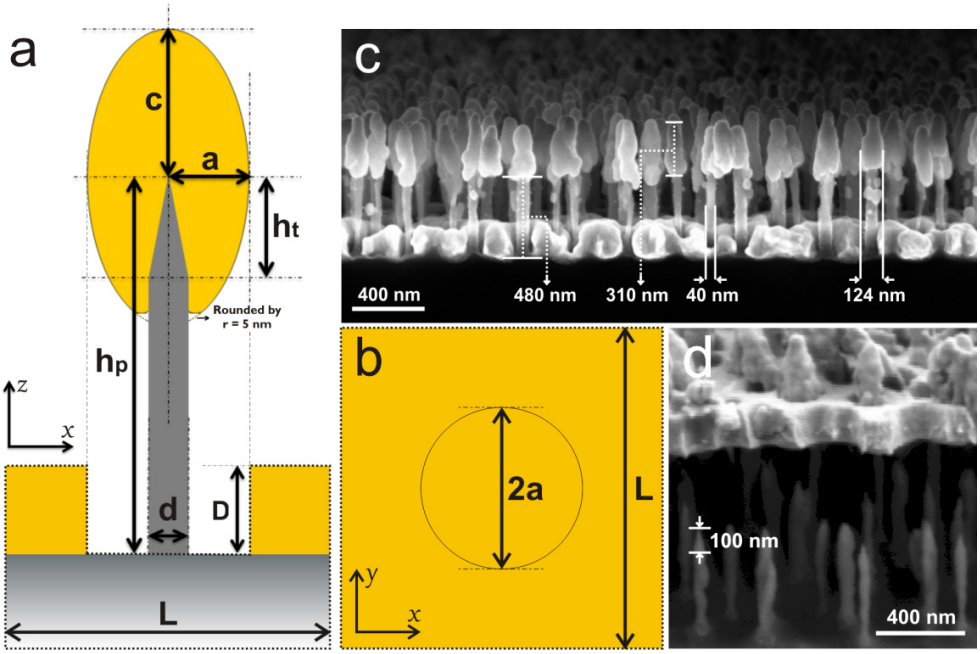

Fig. 1. (a), (b) A modeled single NP, (a) x-z cross-sectional view, (b) x-y top view. Yellow represents metal, while gray stands for silicon. An ellipsoid with a rounded bottom (r = 5 nm) and a cone are used to approximate the metal cap and the tip of the Si pillar, respectively. The substrate is modeled by a Si layer stacked by an Ag film with a hole (radius = a). Unless otherwise noted, the substrate area (surrounded by dotted lines) is excluded from the simulation to reduce computation time. Default values of the geometric parameters are a = 62 nm, c = 155 nm, ht = 100 nm, hp = 635 nm, d = 40 nm, D = 200 nm and L = 400 nm. These values are chosen referring to real NPs observed in (c) and (d). (c) A cross-sectional SEM image of the NPs. Si pillars are covered by Ag, and the Si substrate is covered by an Ag film with holes near the Si pillars. The deposition thickness of Ag is D_{Ag} = 200 nm. (d) A cross-sectional SEM image of the NPs. The Ag film and the Ag caps are lifted up to reveal the bare Si pillars.

3 Results and Discussion

3.1 LSPR Modes of a Single NP

First, LSPR modes of a standalone NP are studied by 3D FEM simulation. Scattering spectra are calculated for both Ag@Si and Au@Si NPs. Results are shown in Fig. 2(a). It can be seen that two LSPR modes can be excited in a single NP. For an Ag@Si NP, the LSPR peaks appear at 650 nm and 800 nm, whereas they appear at 710 nm and 865 nm for the Au@Si case.

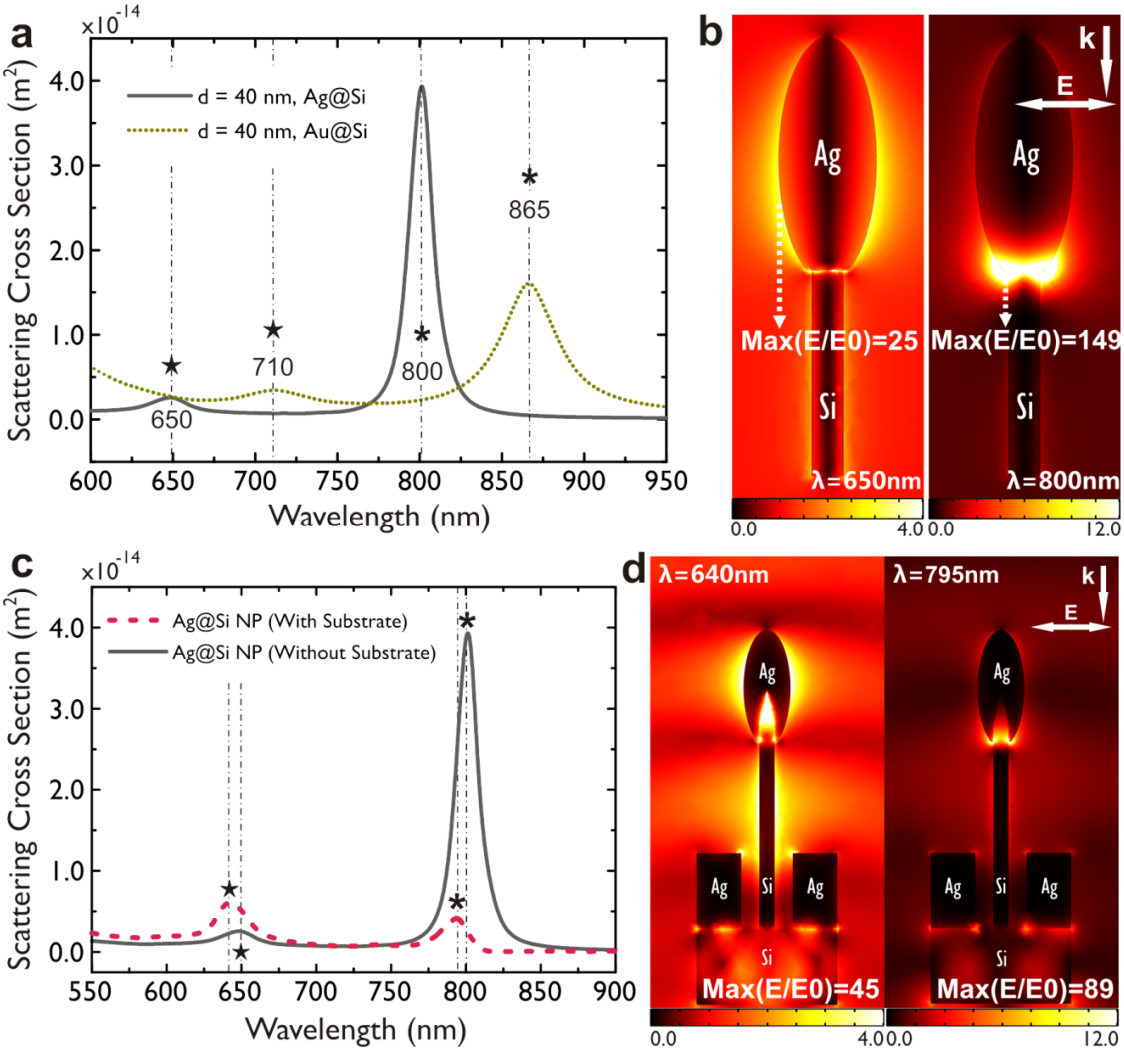

Fig. 2. (a) Calculated scattering cross-section spectra for a single Ag@Si NP (grey line) and a single Au@Si NP (yellow dots). (b) EF distributions on the surface of an Ag@Si NP at resonant LSP wavelengths. (c) Calculated scattering cross-section spectra for an Ag@Si NP with substrate (red dash line) and a standalone Ag@Si NP (grey line). (d) Cross-sectional EF distributions of an Ag@Si NP with a substrate at its resonant LSP wavelengths. The maximum EFs in (b) and (d) are obtained based on the electric fields on the surfaces of those NPs.

To classify the observed LSPR modes, electric field enhancement factor distributions at the resonance wavelengths are plotted for an Ag@Si NP, as shown in Fig. 2(b). At λ = 650 nm, intense and highly localized fields are observed around the Ag cap, due to the strong collective electron oscillations through the center part of the Ag cap. Obviously, such an EF distribution is similar to that of an Ag spherical particle on

resonance. Therefore it is reasonable to define such a LSPR mode as the particle LSPR mode of the NP. At λ = 800 nm, strong EF is observed near the neck of the NP, i.e. near the bottom of the Ag cap. This resonance is caused by the collective electron oscillations inside the bottom part of the Ag cap. Since the diameter of the Si pillar is only 40 nm, which is much smaller than the excitation wavelength, strong coupling between Ag via the Si pillar can be expected. It can be predicted that the diameter of the Si pillar has a strong influence on the resonance wavelength of this mode. (The assumption will be assessed in section 3.2). Due to the plasmonic coupling via the Si pillar, we define such a resonance mode as the cavity LSPR mode of the NP. Note that the maximum EF of the cavity mode is 149, which is about 6 times higher than that of the particle mode. In addition, the enhanced electric field of the cavity mode is more localized than that of the particle mode, as observed in Fig. 2(b). The above discussion is also valid for a single Au@Si NP (field distributions not shown for the Au@Si NP). Its 710 nm and 865 nm peaks correspond to the particle mode and the cavity mode, respectively. The redshifts of the peaks for the Au@Si NP compared with those of the Ag@Si NP are due to the difference in the dielectric functions between Ag and Au. Such red-shifting behavior has been observed and studied extensively in other Ag and Au plasmonic structures [29-31].

Next, the influence of the substrate on the two LSPR modes of a single Ag@Si NP is investigated. The substrate is modeled by a 200 nm thick Si layer stacked by a 200 nm thick Ag film with a hole of radius = a = 62 nm, referring to the SEM image in Fig. 1(c). The simulated scattering spectrum and the EF distributions at the scattering peaks are plotted in Figs. 2(c) and 2(d), respectively. It can be seen that with the presence of the substrate, the NP still has two LSPR modes, i.e. the particle mode and the cavity mode, but they are slightly blue-shifted (10 nm for the particle mode and 5 nm for the cavity mode) comparing to those of a standalone Ag@Si NP. Such blue-shifts are also observed in other plasmonic structures, e.g. crescents [32] and spheres [33] on substrates. Note that since the distance from the center of the Ag cap to the Ag film is 435 nm, which is larger than half of the excitation wavelength, the coupling between the LSP of the nanohole in the Ag film and that of the Ag cap is weak. This gives evidence for the weak LSPR tuning effect introduced by the substrate. However, from Fig. 2(c), it can be seen that introducing the substrate has a significant influence on the LSPR intensities. It

strengthens the scattering cross-section by around 2.5 times for the particle mode, and weakens it by around 8 times for the cavity mode. The reason for this is that the substrate introduces constructive and destructive interference between the incident and the reflected excitation light, as can be seen from the EF patterns in Fig. 2(d). Compared with the maximum EFs of a single Ag@Si NP shown in Fig. 2(b), it can be seen from Fig. 2(d) that by introducing the substrate, at the resonant wavelength of the particle mode, constructive interference happens near the Ag cap region, causing an increase in the maximum EF from 25 to 45, while at the resonant wavelength of the cavity mode, destructive interference happens near the Ag cap region, causing a decrease in the maximum EF from 149 to 89.

3.2 LSPR Wavelengths Broadening of the NPs

Due to the mask-less etching method used, the geometry of the NPs varies, e.g. the diameter of the Si pillar ≈ 40 ± 16 nm, the tip shape of the Si pillar can be sharp or flat, and the shape of the metal caps are different from one to another. Some of these variations can tune the LSPR wavelengths of individual NPs, leading to inhomogeneous broadening of the LSPR peaks. In this section, we study those geometric LSPR tuning effects. First, the influence of the Si pillar diameter d is studied. Fig. 3(a) shows the calculated scattering cross-section of standalone Ag@Si NPs with different d. It can be seen that increasing d causes substantial redshifts to the cavity mode. The mode shifts from 715 nm to 920 nm, when d increases from 24 nm to 64 nm. Such redshifts are linear, as shown in Fig. 3(c), where increasing d by 10 nm introduces a redshift of approximately 50 nm. Changing d tunes the interaction intensity between the Ag on the two sides of the Si pillar near the NP neck. For example, a smaller d strengthens the coupling intensity, leading to the increase of the LSPR energy and thus blue-shifts the cavity LSPR peak. In addition, d affects the LSPR energy of the particle mode. Similarly to what happens to the cavity mode, increasing d red-shifts the particle mode of the NP. Such a redshift is much gentler, compared with that of the cavity mode. Increasing d from 24 nm to 64 nm only leads to a 50 nm redshift of the particle LSPR peak. This is due to the different electron oscillation paths between the particle mode and the cavity mode. Increasing d dramatically changes the plasmonic coupling intensity via the Si pillar for

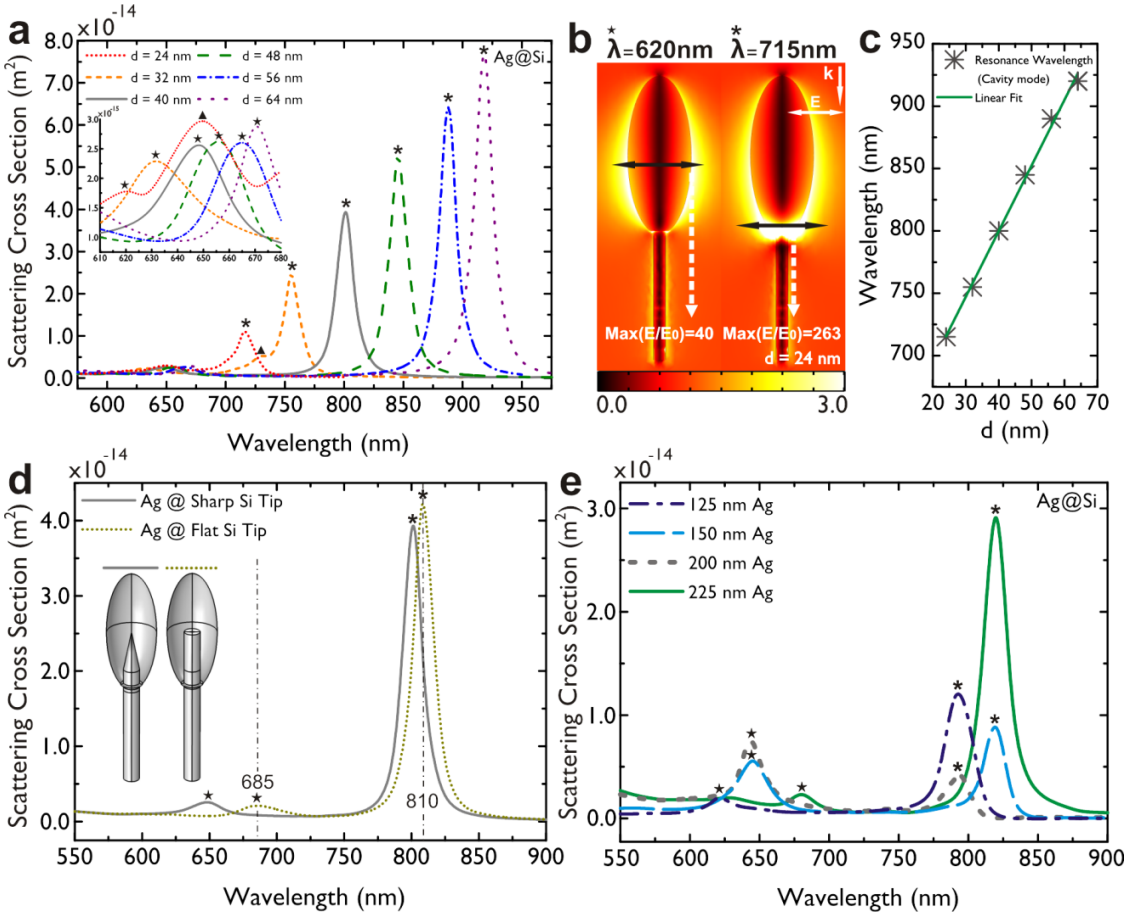

Fig. 3. (a) Calculated scattering cross-section spectra of standalone Ag@Si NPs with different Si pillar diameter d. Asterisks, five-pointed stars and triangles represent the cavity modes, the particle modes and the third mode, respectively. (b) EF distributions on the surface of an Ag@Si NP at resonant wavelengths plotted for the particle mode and the cavity mode, for d = 24 nm. (c) Cavity LSPR wavelengths versus Si pillar diameter d. (d) Calculated scattering cross-section spectra of two standalone Ag@Si NPs. One contains a flat Si pillar tip while the other contains a sharp one. (e) Calculated scattering cross-section spectra of Ag@Si NPs (including substrates) with different Ag deposition thicknesses 125 nm, 150 nm, 200 nm and 225 nm. Geometric parameters are extracted from SEM images. For 125 nm of deposited Ag, a = 37 nm, c = 91 nm, thickness of Ag film on Si wafer = 125 nm. For the 150 nm case, a = 45 nm, c = 144 nm, thickness of Ag film on Si wafer = 150 nm. For the 200 nm case, default values stated in the caption of Fig. 1 are used. For the 225 nm case, a = 65 nm, c = 218 nm, thickness of Ag film on Si wafer = 225 nm. A comparative SEM image showing the Ag@Si NP substrates with different Ag deposition thicknesses can be found in the appendix, Fig. 9.

the cavity mode, while it does not introduce big changes to the dielectric environments in the routes of electron oscillations of the particle mode. Moreover, other than the particle mode and the cavity mode, a third LSPR mode emerges when d is below 32 nm. This mode is marked by triangles in Fig. 3(a).

Since the sharpness of the Si pillar tips is different as shown in Fig. 1(d), their LSPR tuning effect must be studied. For simplicity, this is done by simulating two standalone Ag@Si NPs, one with a sharp Si pillar tip and the other with a flat one. The simulated scattering spectra are shown in Fig. 3(d). It can be seen that as the tip of the Si pillar changes from a sharp one to a flat one, a 10 nm redshift can be observed for the cavity mode, while the resulting redshift for the particle mode is about 35 nm. Similar to explaining the tuning effect of the Si pillar diameter d, the tuning effect of the sharpness of the Si pillar tip can also be explained by the changes in the dielectric environments of the electron oscillating paths and the LSP coupling routes. As the Si pillar tip becomes flatter, the dielectric environment near the NP neck does not change much, thus the resonance wavelength of the cavity mode stays at almost the same position. However, a flatter Si pillar tip dramatically increase the dielectric volume near the center of the Ag cap, where the electron oscillations of the particle mode pass through, therefore leading to a significant 35 nm redshift for the particle LSPR mode.

Finally, the tuning effect of the Ag cap shape is investigated. This is done by simulating additional three Ag@Si pillars including effects of the substrate. Their geometric parameters are extracted from the SEM images of NPs with different Ag deposition thicknesses: 125 nm, 150 nm and 225 nm. The values can be found in the caption of Fig. 3(e). The substrates are taken into account since the deposition thickness will also affect the distance between the Ag caps and the Ag film, resulting in variation of the interference pattern, which has been shown to have a significant influence on the LSPR intensity in section 3.1. The calculated scattering spectra are shown in Fig. 3(e). The particle LSPR mode red shifts from about 620 nm to 680 nm, when the thickness of the deposited Ag increases from 125 nm to 225 nm. In addition, as the deposited Ag thickness increases from 125 nm to 225 nm, it can be observed from Fig. 3(e) that the resonance wavelength of the cavity mode stays at around 800 nm. Therefore it can be concluded that the LSPR energy of the cavity mode is dominated by the cavity size,

rather than the volume of the surrounding metallic structure. Similar results from the study of other cavity based LSP structures support this conclusion [34]. Furthermore, the intensity ratio between the cavity mode and the particle mode varies, when the deposited Ag thickness changes. This is due to the different light interference patterns for the different Ag deposition thicknesses. This effect will be discussed together with the experimental scattering measurements of the NPs in section 3.4.

3.3 LSP Couplings in an Ag NP Dimer

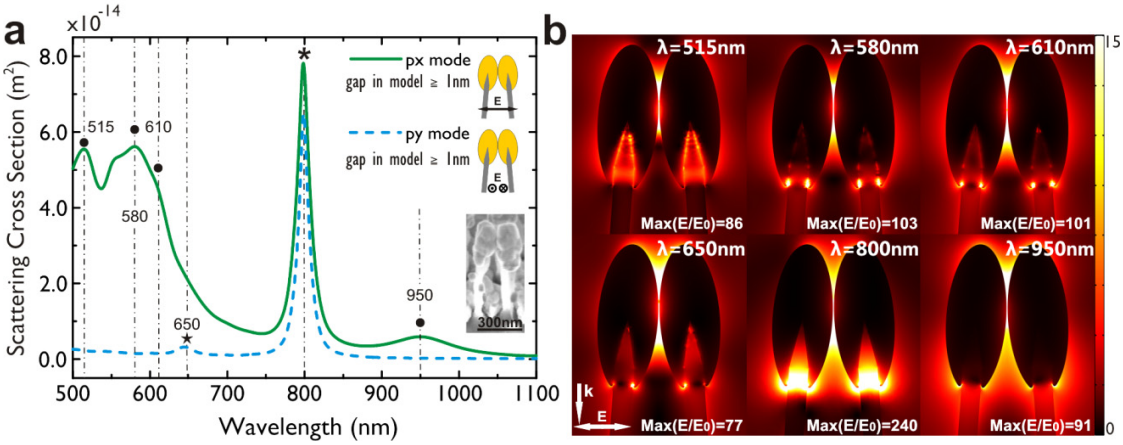

Fig. 4. (a) Calculated scattering cross-section spectra for a dimer of Ag@Si NPs under different polarization directions. The polarization directions used in the calculation are shown in the insets, which also include a SEM image of a NP dimer. The asterisk, the five-pointed star and the circles represent the cavity modes, the particle mode and the hybridized modes, respectively. (b) Cross-sectional EF distributions of a dimer of Ag@Si NPs at different excitation wavelengths for the px mode. The maximum EFs are obtained based on the values of the electric fields on the surface of the NP dimers.

Leaning of the NPs have proved to be critical for applications such as SERS [24]. In this section, the leaning effect is investigated by simulation of a NP dimer with a minimum gap of 1 nm. Simulated scattering spectra of a NP dimer are shown in Fig. 4(a). Two perpendicular polarization directions are used in the calculation, and are labeled as px mode and py mode in Fig. 4(a). For the py mode, the peaks at 650 nm and 800 nm represent the particle mode and the cavity mode, respectively. For the px mode, plasmonic hybridization happens [35]. The results are the vanishing of the 650 nm

particle mode peak and the generation of several new LSPR peaks. Some of them are blue shifted to 610 nm, 580 nm, 515 nm, and one is red shifted to 950 nm, compared with the original 650 nm peak of the particle mode in a standalone NP. However, for the cavity mode, its peak stays at 800 nm for both px and py polarization modes. The reason for this is that the two NPs in the model do not touch or form narrow gaps near their necks, thus plasmonic couplings and interactions are relatively much weaker for the cavity mode compared with those of the particle mode. EF distributions at LSPR wavelengths for the px mode are plotted in Fig. 4(b). By comparing Fig. 4(b) with Fig. 2(b), it can be seen that leaning of two NPs can increase the EF of the particle and the cavity modes by around 1.5 – 4 times via plasmonic couplings and can introduce various new LSPR modes by plasmonic hybridization of the particle mode, enabling the pillars to have strong localized fields in a wide spectral range. Note that in the real case, a cluster of NPs can be dimers, trimers, or contain even more NPs. In addition, the angle of leaning for each NP is usually different. Therefore it is not feasible to simulate all the situations. However, it can be expected based on the simulation result of a NP dimer that for a NP cluster containing more NPs, the LSPR wavelength of the cavity mode does not change or changes very slightly, while the peak of the particle mode vanishes, accompanied by the emergence of various hybridized LSPR modes around 500 – 600 nm. Such an assumption will be proved experimentally in the next section.

3.4 Scattering Measurements on NP Substrates

Finally, scattering measurements are performed using a conventional dark-field setup on NPs before and after leaning. Four substrates with different Ag deposition thicknesses D_{Ag}: 125 nm, 150 nm, 200 nm, and 225 nm are used in the experiment. Cross-sectional view of these NPs are shown in the insets of Fig. 5(b) (D_{Ag} = 125 nm, 150 nm, 225 nm), Fig. 1(c) (D_{Ag} = 200 nm) and Fig. 9. Top views of the leaning NPs are shown in Fig. 5(b). The measured scattering spectra are shown in Fig. 5(a).

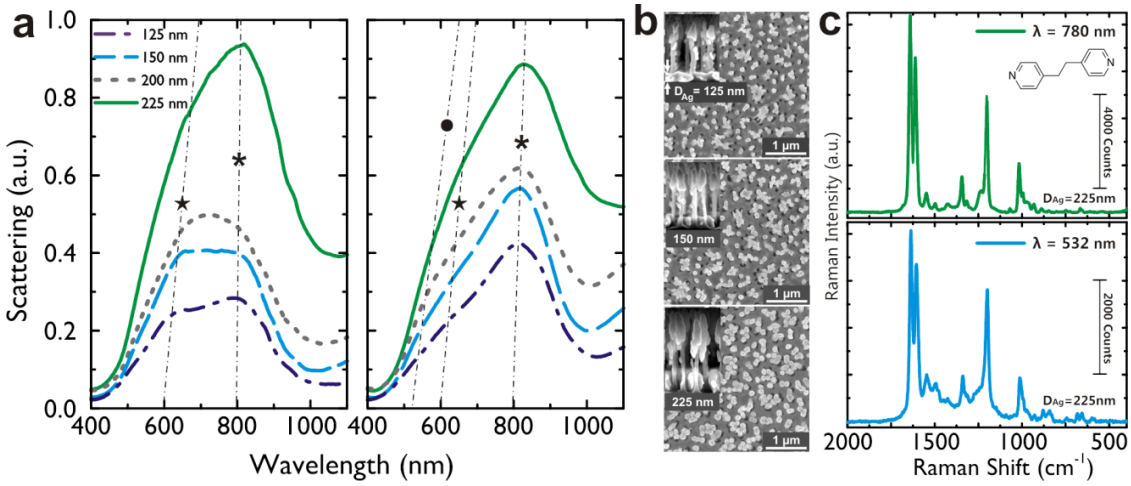

Fig. 5. (a) Measured scattering spectra using a conventional dark-field setup for NPs on four substrates with different Ag deposition thicknesses D_{Ag}: 125 nm, 150 nm, 200 nm, and 225 nm. Asterisks, five-pointed stars and circles represent the cavity modes, the particle modes and the hybridized particle modes, respectively. (b) SEM images of leaning NPs (top view) of substrates with D_{Ag}: 125 nm, 150 nm, and 225 nm, where each NP cluster contains several NPs. Insets: cross-sectional view of the NPs before leaning. (c) SERS spectra of 10 mM trans-1,2-bis (4-pyridyl) ethylene in ethanol solution obtained using the NPs of D_{Ag} = 225 nm under 780 nm and 532 nm excitations. A 10x objective lens was used to focus and collect the light and the laser power was 0.1 mW.

For the NPs before leaning, two peaks can be observed; one stays at around 800 nm, while the other red-shifts from near 600 nm to about 660 nm, when D_{Ag} increases from 125 nm to 225 nm. The former peak corresponds to the cavity LSPR mode of the NPs, while the latter corresponds to the particle LSPR mode. The stability of the cavity LSPR peak and the red-shift of the particle LSPR peak when increasing D_{Ag} have also been shown by the simulation results in Fig. 3(e), as discussed in section 3.2. Note that due to the uneven geometries of the fabricated NPs, the two observed scattering peaks are broad and overlapping. The broadening of the cavity mode peak is dominated by the uneven distribution of the Si pillar diameter, while the broadening of the particle mode is mainly due to the uneven geometries of the Ag caps and the Si pillar tips, according to the analysis in section 3.2 based on the simulated results. The intensity ratio of the two peaks is related to the constructive and destructive interference of the excitation light caused by the substrate. It can be seen from Fig. 5(a) that for D_{Ag} = 125 nm and 225 nm, the scattering intensity of the cavity mode is higher than that of the particle mode, while

for D_{Ag} = 150 nm and 200 nm, the scattering intensity of the two modes are similar. This is consistent to the simulation results shown in Fig. 3(e). When the NPs lean together, it can be seen from Fig. 5(a) that the particle LSPR mode dramatically weakens, accompanied by a very gentle bump in the spectra near 550 nm, indicating the generation of the hybridized modes. In addition, the cavity LSPR modes are shown to be stable at near 800 nm for all the four substrates regardless of leaning. The above results are in agreement with the conclusion in section 3.3, that when NPs form clusters, the LSPR wavelengths of the cavity mode are nearly unaffected, while the peak of the particle mode vanishes, and is accompanied by the emergence of various LSPR modes around 500 – 600 nm that represent the hybridized plasmonic modes. Further evidence of the existence of the cavity LSPR mode can be found in the appendix, in section 5, where we simulated the scattering spectra of a dimer of Ag NPs with and without Si cavities. We show in Fig. 8 that for such structures only the cavity LSPR mode can contribute to the experimentally observed LSPR peaks around 800 nm.

Furthermore, SERS measurements of 10 mM trans-1,2-bis (4-pyridyl) ethylene (BPE) in ethanol solution are performed on the D_{Ag} = 225 nm sample under both 532 nm and 780 nm excitations. NPs are leaned when the analyte solution evaporates. The results are shown in Fig. 5(c). It can be seen that the SERS intensity ratio between 780 nm and 532 nm excitations is about 2, which is in agreement with the ratio observed in the scattering spectrum of the leaning NPs (D_{Ag} = 225 nm) in Fig. 5(a). It can be deduced that the SERS signals under 780 nm excitation benefit most from the strong localized fields near the necks of the NPs generated by the cavity LSPR mode, while for the 532 nm case, the hot-spots in the gaps of the NPs generated by the hybridized particle modes contribute the most. Furthermore, the NP substrate exhibits a good SERS uniformity with a standard deviation of 5.2 % of the average signal intensity over a length of 1 inch, as shown in Fig. 10 in the appendix. The result demonstrates the accuracy of the employed fabrication procedure.

4 Conclusion

Localized plasmon resonances and plasmon couplings in Ag capped Si nanopillar structures were studied by 3D FEM simulations and dark-field scattering measurements. The simulation results show that a standalone Ag@Si NP has two LSPR modes, the particle mode and the cavity mode. The particle mode can be distinguished by the enhanced localized fields near the center of the Ag cap. The cavity mode can be distinguished by the enhanced localized fields near the neck of the Ag cap, and its resonance position is dominated by the diameter of the Si pillar. The resonance energy of the particle mode is shown to be sensitive to the size of the Ag cap and can be hybridized by leaning of the pillars. The resonance energy of the cavity mode is however only dominated by the diameter of the Si pillar, and cannot be tuned via leaning of adjacent nanopillars. Furthermore, the presence of the substrate is shown to have little tuning effect on the two LSPR modes of the NP, but can dramatically change the intensity of the two modes by introducing constructive or destructive interferences of the excitation lights, depending on the distance from the substrate to the Ag cap. The scattering measurements support the conclusions drawn from the simulations. The measured scattering peaks are broad, due to the uneven geometries of the fabricated NPs. In addition, the ratio of the SERS intensities between 780 nm and 532 nm excitations for 10 mM BPE fits the ratio in the scattering measurement. These SERS spectra also prove that the NP substrate has a wide LSPR energy range due to the contribution of both the hybridized modes and the cavity modes, as shown in the scattering spectra, where each of them covers wide range LSPR energies. The results in this paper provide guidance for further optimization and development of such structures, to realize e.g. tuning of the LSPR wavelengths towards near- and mid- infrared for SEIRA applications and for further increases in EF to improve the SERS detection limits.

5 Appendix

5.1 Fabrication of NP Substrates

The Ag NP substrates are fabricated using a four-step nanofabrication process. First, mask-less Si RIE is used to form Si pillars over an entire 4 inch Si wafer. 4 inch p-

type single-side polished (100) wafers are used. Etching is conducted in an Advanced Silicon Etcher (Surface Technology Systems MESC Multiplex ICP) at a SF_6:O_2 flow ratio of 1.12, platen power of 120 W and a chamber pressure of 36 mTorr. The Si NPs are formed at a rate of ~3 nm/s. The Si NP density is ~20 pillars/μm^2. Subsequently, an oxygen plasma process of 1 minute is applied to remove Si RIE byproducts from the Si surface. Here, an Advanced Silicon Etcher (Surface Technology Systems MESC Multiplex ICP) is used at an O_2 flow of 45 sccm, a platen power of 20 W, a coil power of 800 W and a chamber pressure of 10 mTorr. Lastly, a continuous Ag metal film is deposited over the whole wafer using e-beam evaporation. Alcatel SCM 600 is used at a pressure of 2 x 10^{-6} mbar for the deposition. The deposition rate is 10 Å/s for the Ag evaporation.

5.2 Scattering Measurements

Scattering spectra of Ag NPs are acquired using a dark-field microscopy system. First, light from a halogen lamp (Instrument Systems, Model: DLS 500) is coupled into a cleaved optical fiber for uniform irradiation of the Ag NP sample. The incident angle is 30 degrees. Then, the scattered light is collected by a 10x objective lens and recorded by a spectrometer (Instrument Systems, Model: Spectro 320-141). Finally, the recorded scattering intensity is normalized with the lamp spectrum.

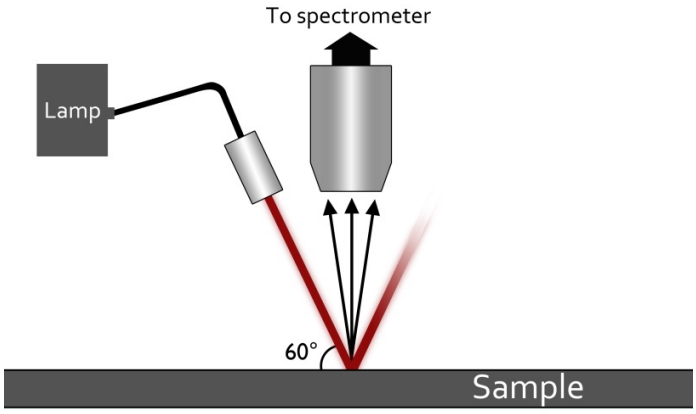

Fig. 6: A schematic of the dark-field scattering measurements.

5.3 SERS Measurements

The SERS experiments are conducted using a Thermo Scientific Raman DXR microscope. The signal collection time is 1s and is averaged 3 times. A 25 μm slit is used. The laser spot is about 3.1 μm in diameter. The microscope was coupled to a single grating spectrometer with a 5 cm^{-1} FWHM spectral resolution and a ± 2 wavenumber accuracy. All SERS spectra were collected at 0.1 mW laser power, using a 10x objective. The target molecule is 10 mM trans-1,2-bis (4-pyridyl) ethylene (BPE) dissolved in ethanol. Droplets of BPE were deposited on the NPs and left for drying during which the NPs lean together, forming clusters.

5.4 LSPR Contribution of the Nanoholes

To prove the validity of eliminating the LSPR effects of the nanoholes on the substrate, scattering and SERS measurements are performed on a substrate, where the NPs are peeled off by tape, as shown in Fig. 7(b). For comparison, measurements are also conducted on a sample with normal standing NPs. The measured scattering and SERS spectra are shown in Fig. 7(a) and Fig. 7(c), respectively. It can be seen from Fig. 7(a) that the contribution to the scattering signal by the nanoholes is negligible. This is reasonable since the sizes and shapes of the nanoholes are highly uneven, thus there are no specific resonance wavelengths for the nanoholes. It can also be seen from Fig. 7(c) that the localized fields around the nanoholes are very weak, since the SERS signal decreases by 200 times when the NPs are peeled off. In conclusion, the nanoholes on the Ag film above the Si wafer do not have a specific LSPR energy, and their LSPR resonance and the resulting localized fields are negligible compared with those produced by the NPs.

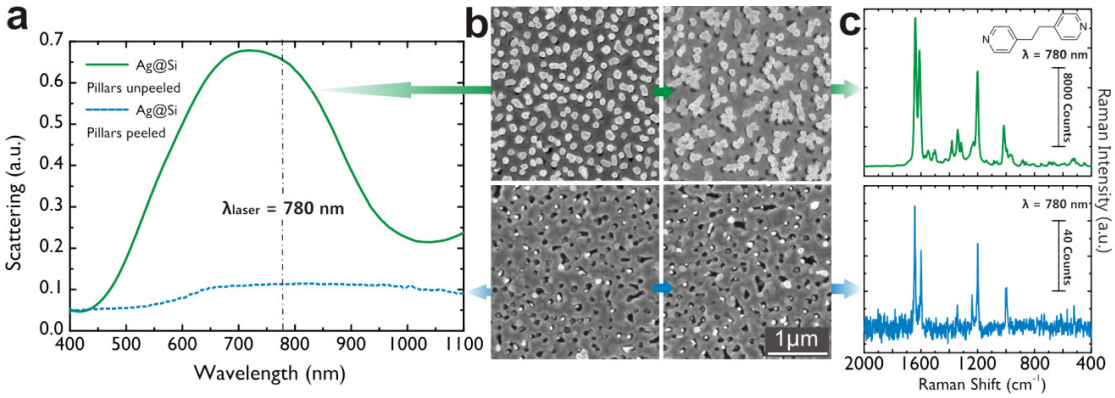

Fig. 7. (a) Measured scattering spectra using a conventional dark-field setup on an Ag@Si NP substrate and an Ag@Si NP substrate with NPs peeled off. The Ag deposition thickness is D_{Ag} = 200 nm. (b) Upper and lower left: Top view SEM images of the two substrates used for the scattering measurements in (a), Upper and lower right: Top view SEM images of the samples used in the SERS measurements in (c). The NPs are leaned during the evaporation of the target molecule solution, as seen in the upper right image. (c) SERS spectra of 10mM BPE in ethanol obtained using the substrates shown in (b) under 780 nm excitation. A 10x lens is used to focus and collect the light and the laser power is 0.1 mW.

5.5 Further Evidence Proving the Existence of the Cavity LSPR Mode

We have measured optical properties (dark-field scattering spectra) of some Ag NP structures with different Ag NP cap sizes in order to evaluate LSPR peak positions, as shown in Figs. 5(a) and 5(b) in the main text. Here, we further evaluate and demonstrate the existence of the Ag cap cavity resonance mode using FEM calculations. For simplicity, we consider a dimer of Ag NPs with and without Ag cavities.

In Fig. 8(a), we define Ag NPs as Ag ellipsoid positioned on top of a Si nanopillar. We otherwise use the same parameters as shown in Fig. 4. The calculated scattering spectra in Fig. 8(a) for both incident field polarizations are dramatically different compared to those of the Ag NP dimer with Si cavities, shown in Fig. 8(b). All LSPR peaks in Fig. 8(a) are at around 600 nm, and the spectra are quite different from the experimental ones shown in Fig. 5(a), since no LSPR peaks can be found near 800 nm in Fig. 8(a). In Fig. 8(b) we define the Ag NP dimer including Ag cap cavities. In this case, the LSPR peaks caused by the plasmon couplings via the Ag NP cap cavities are found at around 800 nm. Their position is close to those in the experimentally observed spectra

shown in Fig. 5(a). We believe these results provide further evidence that proves the existence of the cavity LSPR mode whose resonance position is very stable regardless of leaning, and such cavity LSPR mode contributes to the experimentally observed LSPR peaks at around 800 nm, that are also stable regardless NP leaning.

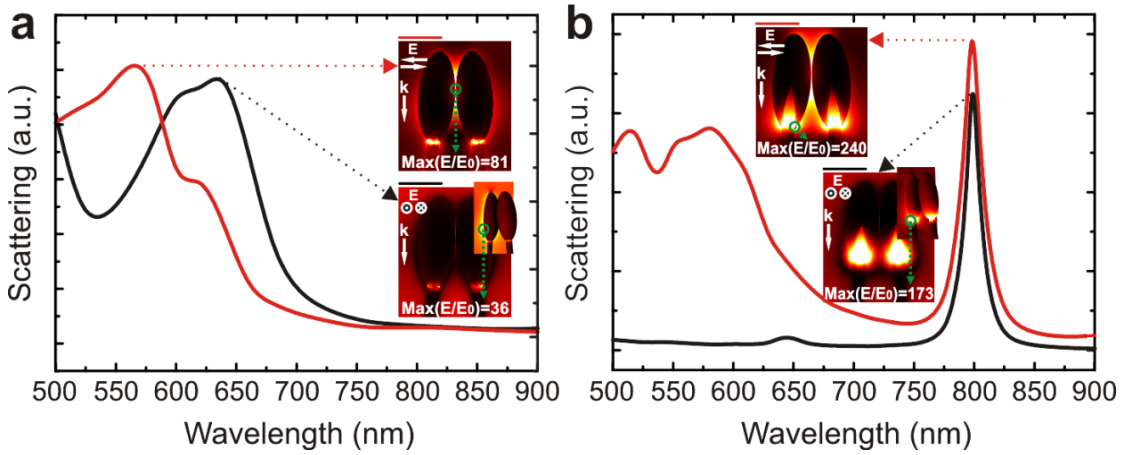

Fig. 8. (a) Calculated scattering spectra for a dimer of standard Ag@Si NPs without Si cavities (the Si inside the Ag caps are replaced by Ag) under different polarization directions. The polarization directions used in the calculation are shown in the insets. Insets: electric field enhancement maps plotted for the strongest resonance peaks under different polarization directions. (b) Same as (a), but for the case that the NPs contain Si cavities inside their Ag caps.

5.6 Geometric Changing of the NP Substrate when Increasing the Ag Deposition Thickness

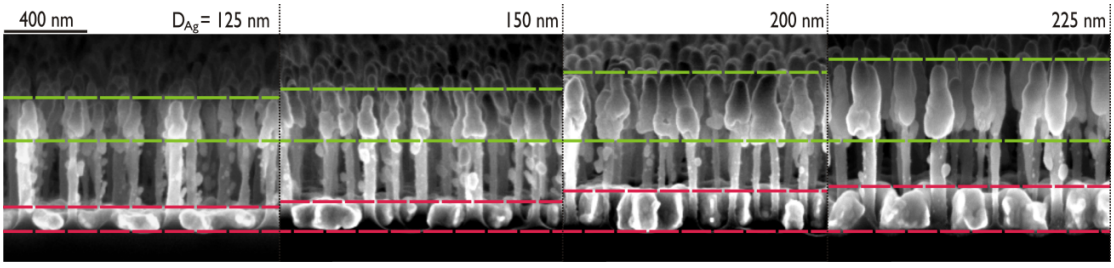

Fig. 9. Cross-sectional SEM images of the NP substrates with different Ag deposition thicknesses D_{Ag} = 125 nm, 150 nm, 200 nm and 225 nm. Si pillars are covered by Ag, and the Si substrate is covered by an Ag film with holes near the Si pillars. For all the samples, Si pillars are made by the same etching recipe described in the appendix, section 1 with the same etching time of 4 minutes. All samples are tilted by 5° during the SEM measurements.

As can be seen from Fig. 9, when the Ag deposition thickness D_{Ag} increases from 125 nm to 225 nm, the average size of the Ag caps increases both laterally and vertically. In addition, the average thickness of the Ag film on the Si substrate increases. Furthermore, the average distance between the bottom of the Ag caps and the Ag film decreases when increasing D_{Ag} from 125 nm to 225 nm.

5.7 SERS Uniformity of the NP Substrate

As shown in Fig. 10, the NPs exhibit high SERS uniformity over the 1 inch mapping line. The standard deviation for the 1641 cm^{-1} BPE Raman peak is 5.2 % of the average signal intensity. Such a result indicates that the fabrication procedure of the NP substrate is quite accurate, i.e., NPs with a large-scale uniformity are fabricated.

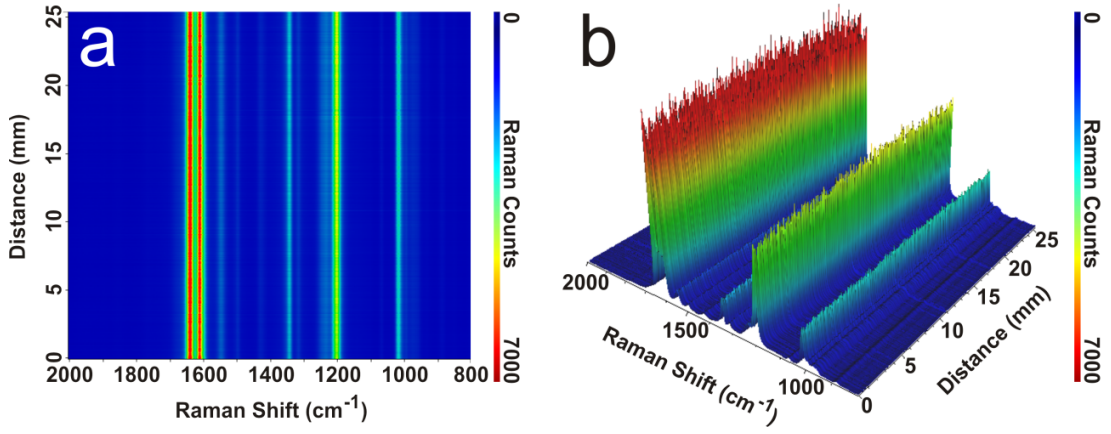

Fig. 10. Mapped SERS spectra of 10 mM BPE in ethanol solution obtained using the NP sample of D_{Ag} = 225 nm under a 780 nm excitation. (a) 2-D view. (b) 3-D view. The mapping distance was 1 inch. The step size was 50 um. A 10x objective lens was used to focus and collect the light and the laser power was 0.1 mW. The diameter of the laser spot was 3.1 um. Droplets of BPE were deposited on the NPs and left for drying during which the NPs lean together, forming clusters. The standard deviation for the 1641 cm^{-1} BPE Raman peak is 5.2 % of the average signal intensity.

6 Acknowledgement

This work has been funded by the NAPLAS project, The Danish Council for Independent Research.

References

1. N. J. Halas, S. Lal, W. Chang, S. Link and P. Nordlander, "Plasmons in strongly coupled metallic nanostructures," Chem. Rev. **111**(6), 3913-3961 (2011).
2. M. E. Stewart, C. R. Anderton, L. B. Thompson, J. Maria, S. K. Gray, J. A. Rogers and R. G. Nuzzo, "Nanostructured plasmonic sensors," Chem. Rev. **108**(2), 494-521 (2008).
3. P. L. Stiles, J. A. Dieringer, N. C. Shah and R. P. Van Duyne, "Surface-enhanced Raman spectroscopy," Annu. Rev. Anal. Chem. **1**, 601-626 (2008).
4. J. Kneipp, H. Kneipp, and K. Kneipp, "SERS - a single-molecule and nanoscale tool for bioanalytics," Chem. Soc. Rev. **37**, 1052–1060 (2008).
5. B. Sharma, M. F. Cardinal, S. Kleinman, N. G. Greeneltch, R. R. Frontiera, M. G. Blaber, G. C. Schatz and R. P. Van Duyne, "High performance SERS substrates: advances and challenges ," MRS Bulletin **38**, 614–624 (2013).
6. S. Chen, M. Svedendahl, R. P. Van Duyne and M. Käll, "Plasmon-enhanced colorimetric ELISA with single molecule sensitivity," Nano Lett. **11**(4), 1826–1830 (2011).
7. Y. Shen, J. Zhou, T. Liu, Y Tao, R. Jiang, M. Liu, G. Xiao, J. Zhu, Z. Zhou, X. Wang, C. Jin and J. Wang, "Plasmonic gold mushroom arrays with refractive index sensing figures of merit approaching the theoretical limit," Nat. Commun. **4**, 2381 (2013).
8. O. Kedem, A. Vaskevich and I. Rubinstein, "Critical issues in localized plasmon sensing," J. Phys. Chem. C **118**(16), 8227–8244 (2014).
9. R. Adato and H. Altug, "In-situ ultra-sensitive infrared absorption spectroscopy of biomolecule interactions in real time with plasmonic nanoantennas," Nat. Commun. **4**, 2154 (2013).
10. R. Bukasov and J. S. Shumaker-Parry, "Silver nanocrescents with infrared plasmonic properties as tunable substrates for surface enhanced infrared absorption spectroscopy," Anal. Chem. **81**(11), 4531–4535 (2009).
11. V. J. Sorger, R. F. Oulton, R. Ma and X. Zhang, "Toward integrated plasmonic circuits," MRS Bulletin **37**, 728–738 (2012).

12. H. Wei, Z. Wang, X. Tian, M. Käll and H. Xu, “Cascaded logic gates in nanophotonic plasmon networks,” Nat. Commun **2**, 387 (2011).
13. S. Schmid, K. Wu, P. E. Larsen, T. Rindzevicius and A. Boisen, “Low-Power Photothermal Probing of Single Plasmonic Nanostructures with Nanomechanical String Resonators,” Nano. Lett. **14**(5), 2318–2321 (2014).
14. A. M. Goodman, Y. Cao, C. Urban, O. Neumann, C. Ayala-Orozco, M. W. Knight, A. Joshi, P. Nordlander and N. J. Halas, “The surprising in vivo instability of near-IR-absorbing hollow Au-Ag nanoshells,” ACS Nano **8**(4), 3222–3231 (2014).
15. J. Li, Y. Huang, Y. Ding, Z. Yang, S. Li, X. Zhou, F. Fan, W. Zhang, Z. Zhou, D. Wu, B. Ren, Z. Wang and Z. Tian, “Shell-isolated nanoparticle-enhanced Raman spectroscopy,” Nature **464**, 392–395 (2010).
16. X. Xia, J. Zeng, Q. Zhang, C. H. Moran and Y. Xia, “Recent Developments in Shape-Controlled Synthesis of Silver Nanocrystals,” J. Phys. Chem. C **116**(41), 21647–21656 (2012).
17. M. J. Banhozler, J. E. Millstone, L. Qin and C. A. Mirkin, “Rationally designed nanostructures for surface-enhanced Raman spectroscopy,” Chem. Soc. Rev. **37**, 885–897 (2008).
18. P. Dawson, J. A. Duenas, M. G. Boyle, M. D. Doherty and S. E. J. Bell, “Combined Antenna and Localized Plasmon Resonance in Raman Scattering from Random Arrays of Silver-Coated, Vertically Aligned Multiwalled Carbon Nanotubes,” Nano Lett. **11**(2), 365–371 (2011).
19. M. Hu, F. S. Ou, W. Wu, I. Naumov, X. Li, A. M. Bratkovsky, R. S. Williams and Z. Li, “Gold Nanofingers for Molecule Trapping and Detection,” J. Am. Chem. Soc. **132**(37), 12820–12822 (2010).
20. S. J. Lee and M. Moskovits, “Remote Sensing by Plasmonic Transport,” J. Am. Chem. Soc. **134**(28), 11384–11387 (2012).
21. N. G. Greeneltch, M. G. Blaber, A.-I. Henry, G. C. Schatz and R. P. Van Duyne, “Immobilized Nanorod Assemblies: Fabrication and Understanding of Large Area Surface-Enhanced Raman Spectroscopy Substrates,” Anal. Chem. **85**(4), 2297–2303 (2013).

22. J. S. Shumaker-Parry, H. Rochholz and M. Kreiter, “Fabrication of Crescent-Shaped Optical Antennas,” Adv. Mater. **17**(17), 2131–2134 (2005).
23. B. J. Roxworthy, A. M. Bhuiya, X. Yu, E. K. C. Chow and K. C. Toussaint Jr, “Reconfigurable nanoantennas using electron-beam manipulation,” Nat. Commun. **5**, 4427 (2014).
24. M. S. Schmidt, J. Hübner and A. Boisen, “Large Area Fabrication of Leaning Silicon Nanopillars for Surface Enhanced Raman Spectroscopy,” Adv. Mater. **24**(10), OP11–OP18 (2012).
25. K. Wu, T. Rindzevicius, M. S. Schmidt, K. B. Mogensen, A. Hakonen and A. Boisen, “Wafer-Scale Leaning Silver Nanopillars for Molecular Detection at Ultra-Low Concentrations,” J. Phys. Chem. C **119**, 2053-2062 (2015).
26. J. Yang, M. Palla, F. G. Bosco, T. Rindzevicius, T. S. Alstrøm, M. S. Schmidt, A. Boisen, J. Ju and Q. Lin, “Surface-Enhanced Raman Spectroscopy Based Quantitative Bioassay on Aptamer-Functionalized Nanopillars Using Large-Area Raman Mapping,” ACS Nano **7**(6), 5350–5359 (2013).
27. J. J. Castillo, T. Rindzevicius, K. Wu, M. S. Schmidt, K. A. Janik, A. Boisen, W. Svendsen, N. Rozlosnik and J. Castillo-León, “Synthesis and characterization of covalent diphenylalanine nanotube-folic acid conjugates,” J. Nanopart. Res. **16**, 2525 (2014).
28. P. B. Johnson and R. W. Christy, “Optical Constants of the Noble Metals,” Phys. Rev. B **6**, 4370–4379 (1972).
29. S. Kadkhodazadeh, J. Rosenkrantz de Lasson, M. Beleggia, H. Kneipp, J. B. Wagner and K. Kneipp, “Scaling of the Surface Plasmon Resonance in Gold and Silver Dimers Probed by EELS,” J. Phys. Chem. C **118**, 5478–5475 (2014).
30. E. Hutter, J. H. Fendler and D. Roy, “Surface Plasmon Resonance Studies of Gold and Silver Nanoparticles Linked to Gold and Silver Substrates by 2-Aminoethanethiol and 1,6-Hexanedithiol,” J. Phys. Chem. B **105**, 11159–11168 (2001).
31. R. Gupta, M. J. Dyer and W. A. Weimer, “Preparation and characterization of surface plasmon resonance tunable gold and silver films,” J. Appl. Phys. **92**, 5264 (2002).
32. L. Y. Wu, B. M. Ross and L. P. Lee, “Optical Properties of the Crescent–Shaped Nanohole Antenna,” Nano Lett. **9**(5), 1956–1961 (2009).

33. S. Raza, W. Yan, N. Stenger, M. Wubs and N. A. Mortensen, “Blueshift of the surface plasmon resonance in silver nanoparticles: substrate effects,” Opt. Express. **21**(22), 27344–27355 (2013).
34. K. Wu, X. Cheng and L. P. Lee, “Intra-particle coupling and plasmon tuning of multilayer Au/dielectric/Au nanocrescents adhered to a dielectric cylinder,” Nanotechnology **23**, 055201 (2012).
35. E. Prodan, C. Radloff, N. J. Halas and P. Nordlander, “A Hybridization Model for the Plasmon Response of Complex Nanostructures,” Science **302**(5644), 419–422 (2003).

CHAPTER 7

WAFER-SCALE LEANING SILVER NANOPILLARS FOR MOLECULAR DETECTION AT ULTRA-LOW CONCENTRATIONS [P2]

Kaiyu Wu,[†] Tomas Rindzevicius,[†,*] Michael Stenbæk Schmidt,[†]
Klaus Bo Mogensen,[†] Aron Hakonen,[‡] and Anja Boisen[†]

†Technical University of Denmark, Department of Micro- and Nanotechnology
Ørsteds Plads, Building 345 east, 2800 Kgs. Lyngby, Denmark
‡Chalmers University of Technology, Department of Applied Physics
Gothenburg, 412 96, Sweden
**Technical University of Denmark, Department of Micro- and Nanotechnology*
Ørsteds Plads, Building 345 east, 2800 Kgs. Lyngby, Denmark
Phone: +45 45 25 57 28
E-mail: trin@nanotech.dtu.dk

Published in
J. Phys. Chem. C **2015**, *119*, 2053 – 2062
doi: 10.1021/jp510073y

Wafer-scale surface-enhanced Raman scattering (SERS) substrates fabricated using maskless lithography are important for scalable production targets. Large-area, leaning silver-capped silicon nanopillar (Ag NP) structures suitable for SERS molecular detection at extremely low analyte concentrations are investigated. Theoretical results show that isolated Ag NPs essentially support two localized surface plasmon (LSP) modes. The most prominent LSP resonance is observed in the near-infrared region (~800 nm) and can

be tuned by changing the diameter of the silicon nanopillars (Si NPs). The corresponding electric field distribution maps indicate that the maximum E-field enhancement is found at the Ag cavity, i.e., the bottom part of the Ag cap. We argue that the plasmon coupling between the resonant Ag cap cavities contributes most to the enhancement of the Raman signal. We experimentally evaluate these findings and show that by exposing Si NPs to an O_2-plasma the average Ag NP cluster size, and thus the overall interpillar coupling, can be systematically reduced. We show that deposition of Cr adhesion layers on Si NPs (>3 nm) introduces plasmon coupling loss to the Ag NP LSP cavity mode that significantly reduces the SERS intensity. Results also show that short exposures to the O_2-plasma and the use of 1 - 3 nm Cr adhesion layers are advantageous for reducing the signal background noise from Ag NPs. In addition, the influence of the Ag NP height and Ag metal thickness on SERS intensities is investigated and optimal fabrication process parameters are evaluated. Finally, the SERS spectrum from 100 pM trans-1,2-bis (4-pyridyl) ethylene (BPE) is recorded, showing distinct characteristic Raman vibrational modes. The calculated enhancement factor is of the order of 10^8, and the SERS signal intensity exhibits a standard deviation of around 14% (660 data points) across a 5×5 mm^2 surface area.

1 Introduction

Surface-enhanced Raman scattering (SERS)[1-3] is a well-established spectroscopic technique for chemical and biological sensing. Noble metal nanostructures support localized surface plasmon resonances (LSPRs)[4-6] that spatially confine the incident field and produce tremendous electromagnetic field enhancement spots, i.e., hot spots.[7] A broad variety of SERS substrates have been fabricated over the past decade, e.g., nanorods,[8] nanocubes,[9] nanostars,[10] various particle arrays,[11-16] and silver dendrites.[17] Recently, electric field (E-field) enhancement factors (EFs) above 10^8 to even 10^{10} have been reported.[1] Detection limits down to a single molecule level have also been reported.[18-20] For a practical use, it is generally required that SERS substrates display (i) high and reproducible EFs over large surface areas and (ii) a tunable LSPR wavelength over a broad spectral region.[1] For applications that require mass-produced SERS substrates, structures should also be robust, be cost-effective, and involve few

nanofabrication steps that are compatible with high volume manufacturing process flows.[21]

From the nanofabrication point of view, the majority of produced SERS substrates are either based on (i) metallic nanoparticles in colloidal suspension or (ii) roughened metallic surfaces. Various shapes of metallic nanoparticles in colloidal solutions showing high EFs with tunable LSPR wavelengths have been synthesized, and their optical properties have been investigated both experimentally and theoretically.[9,11-16] The main advantage of the SERS active colloidal suspensions is high EFs caused by the lightning-rod effect that is particularly pronounced in metal nanoparticles with sharp surface features. Decreasing the interparticle separation, the LSPR coupling increases and the largest E-field enhancement values are usually obtained in the case of colloidal particle aggregates. In order to control the interparticle spacing, additional process steps are often needed. For instance, H. Wang et al. have reported a method to fabricate sub-10 nm gaps in highly ordered Au particle arrays functionalized with cetyltrimethylammonium bromide (CTAB).[13] Sub-10 nm distance control between plasmonic nanoparticles can also be realized by biotemplate assisted synthesis.[15,16]

Nanostructured surfaces can be tailored using a wide range of experimental approaches.[1] A mask for a given nanostructure can initially be produced using lithographic techniques such as nanosphere[22] or e-beam lithography.[23] Then, the final morphology is defined through metal deposition and resist lift-off processes that convert the mask into Raman active SERS substrates.[22-26] Generally, such SERS substrates exhibit better nanostructure uniformities with more reproducible SERS signals across a larger surface area compared to, e.g., particle colloids. One issue with this type of SERS substrates is that, while the reproducibility of the SERS signal improves, the intensity usually decreases.[27] Several methods have been developed to increase EFs by employing sharp metal particle features[28, 29] and by forming sub-10 nm gaps between the nanostructures.[30, 31]

Vertically standing metal nanopillar (NP) structures are good candidates to fulfill both uniformity and high E-field enhancement requirements for reproducible molecular detection. Various NP arrays using e-beam lithography,[32] anodized aluminum oxide templates,[33,35] nano-imprinting,[34] oxygen-plasma-stripping-of-photoresist technique,[36] ion

milling,[37] interference lithography,[38, 40] and coating of multiwalled carbon nanotubes[39] have been reported. Recently, we have developed a new method to fabricate wafer-scale Ag-capped Si nanopillar (Ag NP) SERS substrates utilizing maskless lithography.[41, 42] The fabrication method is particularly interesting due to its simplicity, low cost, and high throughput that are necessary for commercial applications. These Ag NP substrates are capable of producing high E-field enhancement, while the SERS signal uniformity remains relatively stable across a large (> cm^2) substrate surface area.[34, 41] Since the NP fabrication process is essentially based on two simple and cost-effective steps, it opens new possibilities to tailor materials at the nanometer scale without the use of expensive lithographic tools.

Despite the aforementioned advantages, challenges in the nanofabrication procedure still remain. The SERS background noise of the Ag NP structures is considerable, and the SERS enhancement factor is not optimized. These shortcomings could inhibit molecular detection at < nM concentrations. In order to develop the leaning Ag NP structures into a robust SERS platform, a more thorough understanding of the fabrication process capabilities and limitations is required. There is a need for further theoretical and experimental work to address (i) the nature of the resonant Ag NP excitations and subsequently (ii) evaluate experimental procedures that affect the SERS intensity, uniformity, and background signals.

In this work, we first provide theoretical insight into the resonant Ag NP excitations. Scattering spectra and E-field enhancement distributions around single Ag NPs were simulated using the finite element method (FEM). We find that the optical properties of Ag NPs are dominated by an Ag cap cavity LSPR mode. Importantly, the E-field enhancement maps show that the largest enhancement is located at the bottom of the Ag cap and in contact with the Si NP. This allows us to investigate experimental process parameters that affect the SERS signal intensity and the background noise measured from Ag NPs. Fabrication process steps for removing Si reactive ion etching (RIE) byproducts from the Si NP surface that constitute the SERS background noise are introduced. We systematically expose Si NPs to O_2-plasma treatment and show that the process can be utilized for both the Si NP surface cleaning and to reduce the average Ag NP cluster size. The latter gradually reduces the observed SERS intensities. Cr adhesion layers on Si NPs

can also be used to reduce background noise. However, the plasmon coupling losses become non-negligible for >3 nm Cr layers and the SERS intensity is considerably decreased. In addition, we vary the Ag NP height and the thickness of the Ag metal film to obtain maximum SERS intensities and signal uniformities. Finally, the experimentally optimized Ag NP substrates are evaluated by SERS detection at low analyte concentrations (<nM).

2 Theoretical Methods

The theoretical section is aimed at helping to understand the nature of the resonant Ag NP excitations and is used as a general guideline to interpret the experimental data. Since the nanostructures are fabricated using maskless lithography, a variation in the Si NP width and Ag cap surface morphologies is inherent in the fabrication process. Therefore, the Ag NP geometry was constructed using only the experimentally observed representative Ag NP dimensions. An Ag metal film below the NPs is not included in the theoretical model. An isolated Ag NP is modeled as a Si cylinder with a rounded bottom and a cone-shaped tip covered by the Ag metal film; see the schematic picture in Figure 1a. 3D FEM is utilized to calculate scattering spectra and the electric field enhancement distribution around a single Ag NP. Both Si and Ag materials are modeled using experimentally obtained complex permittivities,[43, 44] and the surrounding medium is set to a vacuum (n = 1). A perfectly matched layer (PML) is integrated in the model and adjusted to minimize nonphysical reflections at the boundaries. A highly nonuniform adaptive mesh is used to increase the accuracy of calculation, especially near the structure's geometric singularities. The mesh is refined until the EM field converges throughout the solution domain. By solving time-harmonic Maxwell equations under different incident wavelengths, scattering spectra and the E-field enhancement distribution ($|E|/|E_0|$) over the domain of interest can be calculated.

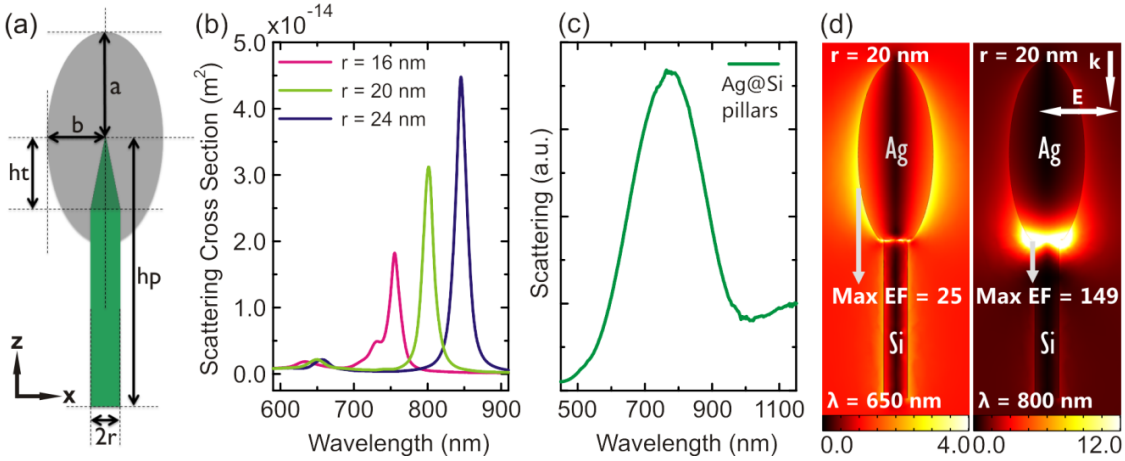

Figure 1. (a) Schematic picture of an Ag NP in the x-z plane. (b) Calculated scattering spectra of isolated Ag NPs with varying Si pillar radius, r. The Ag NP parameters used were a = 155 nm, b = 62 nm, ht = 100 nm, and hp = 400 nm. The tips at the bottom of the Ag ellipsoid are rounded (5 nm in radius). The normal incident light is polarized along the x-axis. The calculations were performed using FEM. (c) Measured scattering spectrum of Ag NPs with r ≈ 20 ± 4 nm, hp ≈ 400 nm, and pillar density ρ_{NP} ≈ 18 ± 2 pillars/μm^2. The thickness of the e-beam evaporated Ag metal film is 200 nm. (d) The calculated E-field enhancement distribution ($|E|/|E_0|$) around a single Ag NP for the LSPR peaks at λ = 650 and 800 nm. The Ag NP parameters used were the same as in part b for r = 20 nm. The color map range for the cavity LSPR at λ = 800 nm was enhanced for clarity.

Figure 1b shows the simulated scattering cross section spectra of a single Ag NP with varying Si NP radii of r = 16, 20, and 24 nm. For r = 20 nm, two LSPR peaks at 650 and 800 nm can be observed and the result is in good agreement with the experimentally obtained Ag NP scattering spectrum, Figure 1c. Due to variations in the radius of the fabricated Si NPs, the measured scattering spectrum exhibits a broader LSPR peak compared to the simulated ones. The simulated E-field enhancement distributions ($|E|/|E_0|$) around the Ag NP are shown in Figure 1d. The E-field enhancement distribution at 650 nm exhibits a clear dipolar pattern; i.e., the largest E-field enhancement factor (EF) is observed at the Ag cap edges and is $|E|/|E_0|$ ~25. The most significant LSPR peak is at 800 nm, and the E-field is spatially confined at the bottom of the Ag cap; i.e., the E-field enhancement originates in the Ag cap cavity; see Figure 1d. The maximum EF for the Ag cap cavity mode is ~149, i.e., ~6 times larger compared to

the 650 nm mode. The resonance peak position of the cavity mode is sensitive to the radius of the Si NP, as is shown in Figure 1b. When the radius r is increased from 16 to 24 nm, the LSP resonance exhibits an ~100 nm red-shift.

The above results indicate some Ag NP fabrication challenges. First of all, a part of the Si NP surface is within the area of high EM fields that originate from the Ag cap cavity. Since the Si surface is covered by the Si RIE byproducts, the SERS background noise can be enhanced, thus inhibiting detection of target molecules at extremely low concentrations. Process steps to control the Si NP surface contamination level are therefore necessary. Furthermore, the use of Cr adhesion layers for the Ag metal deposition can compromise the SERS signal and needs to be experimentally verified. Simulation of a NP by replacing the Ag cap cavity material with Cr shows that the plasmon resonance at ~800 nm vanishes completely; Figure S.1 (Supporting Information). Calculations also show that the size and shape of the Ag cap have a minor influence on the position of the LSPR wavelength of the cavity mode, and that the largest E-field enhancement is observed at the bottom of the Ag cap for both isolated Ag NPs and nearly touching Ag NP dimers; see Figures S.4 and S.5 (Supporting Information), respectively. The results confirm that the LSPR position of the cavity mode is highly sensitive to the radius and refractive index of the Si cylinder, similar to other structures exhibiting cavity LSPR.[45] For SERS applications, some inhomogeneity of the Si NP width is acceptable, since combined (broad) LSPR is suitable for a wide range of laser excitation wavelengths.

3 Experimental Methods

The Ag NP structures were fabricated using a four-step process, schematically shown in Figure 2. First, maskless Si RIE is utilized to form Si NP structures with $r \approx 20 \pm 4$ nm in radius and $h \approx 480$-1810 nm over an entire 4-in. Si wafer. The Si NP density in all cases is $\rho_{NP} \approx 18 \pm 2$ pillars/μm^2. Second, an O_2-plasma process is systematically applied to (i) remove Si RIE byproducts from the Si surface and (ii) control the Ag NP cluster size. Third, a Cr adhesion layer is evaporated onto the Si NP structure. Lastly, a Ag metal film is deposited on the Si NPs using e-beam evaporation. The deposition results in the formation of silver caps at the apex of the Si NPs and a silver film on the underlying Si surface. The Ag NP height, hp, in the following is defined as the distance

from the middle of the Ag cap to the Ag metal surface (Figure 1.). The relation between the Si NP height h, the Ag NP height hp, and the thickness of the Ag metal film D_{Ag} is $h = hp + D_{Ag}$. Silver is chosen due to its favorable dielectric function that results in particularly strong optical resonances in the visible spectral range. The contribution to the absorption cross section due to interband transitions is then negligible.[46]

Si RIE Etching: Four inch p-type single side polished (100) wafers were used. Etching is conducted in an Advanced Silicon Etcher (Surface Technology Systems MESC Multiplex ICP) at a SF_6:O_2 flow ratio of 1.12, a platen power of 110 W, and a bottom chamber pressure of 36 mTorr. The Si NPs are formed at a rate of ~3 nm/s.

Oxygen Plasma Treatment: The Advanced Silicon Etcher (Surface Technology Systems MESC Multiplex ICP) is used at an O_2 flow of 45 sccm, a platen power of 20 W, a coil power of 800 W, and a bottom chamber pressure of 10 mTorr.

Electron Beam Evaporation of Cr and Ag: Alcatel SCM 600 is used at a pressure of 2×10^{-6} mbar. Deposition rates are 3 and 10 Å/s for Cr and Ag evaporation, respectively. The deposited metal layer thickness varies by ± 3%.

SERS measurements: All SERS experiments were conducted using a Thermo Scientific Raman DXR microscope. The signal collection time was 1 s and was averaged three times, using a 25 μm slit and a 0.8 μm diameter laser spot. The microscope was coupled to a single grating spectrometer with a 5 cm^{-1} fwhm spectral resolution and a ± 2 wavenumber accuracy. All SERS spectra were collected at a laser power of 0.1 mW (0.5 mW in Figure 3), using a 10× objective lens and an excitation wavelength of 780 nm unless stated otherwise. The Ag NP SERS substrates were investigated using 10 mM trans-1,2-bis (4-pyridyl) ethylene (BPE) dissolved in ethanol. Droplets of BPE or Mili-Q water (5 μL) were deposited and left for drying. The droplets spread over the whole Ag NP surface area (5×5 mm^2) in several seconds. The SERS signal mapping was performed using 1 mM BPE, 10x objective lens, a 5x5 mm scan area and 30 μm signal collection steps.

Dark-Field Scattering Measurements: The scattering signal of the Ag NPs was acquired using a dark-field microscopy system. Light from a halogen lamp (Instrument Systems, Model: DLS 500) is coupled into an optical fiber to irradiate the Ag NP sample. The incident angle was 30°. The scattered light was collected using a 10× objective lens

and recorded using a spectrometer (Instrument Systems, Model: Spectro 320-141). Finally, the obtained scattering signal was divided by the reference white light spectrum in order to obtain the scattering signal from Ag NPs.

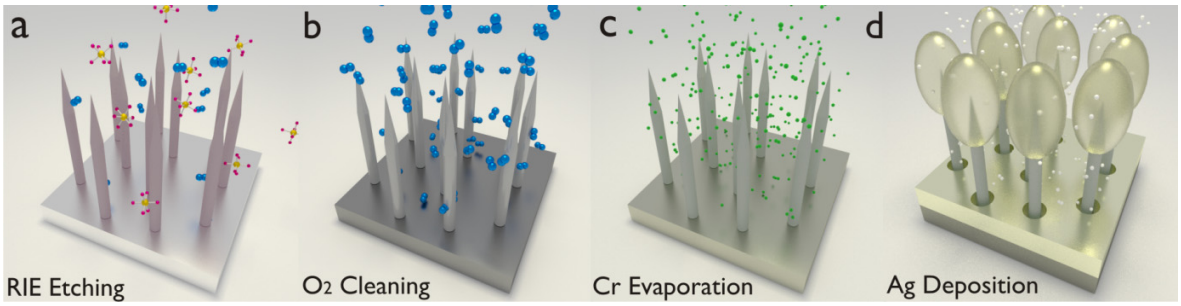

Figure 2. Summary of the fabrication process steps for the Ag NP SERS substrates. (a) Vertically standing Si pillars were produced using maskless RIE, r ≈ 20 ± 4 nm, h ≈ 480 – 1810 nm and pillar density ρ_{NP} ≈ 18 ± 2 pillars/μm^2. (b) The Si NPs were treated using O_2-plasma, t = 0 – 10 min. (c) Deposition of the Cr adhesion layer, D_{Cr} = 0 – 10 nm. (d) Evaporation of Ag metal film, D_{Ag} = 125 – 300 nm.

4 Results and Discussion

4.1 O_2 Plasma Treatment

In this section, we study the influence of O_2-plasma exposure on the SERS signal intensity and the background noise. The Si NP structures are plasma etched using SF_6 and O_2 gases, and therefore, Si etching byproducts are expected to cover the Si surface. To evaluate this, all substrates in this section were fabricated using identical experimental conditions yielding Si NP arrays with r ≈ 20 ± 4 nm, h ≈ 600 ± 30 nm, and ρ_{NP} ≈ 18 ± 2 pillars/μm^2. The structures were then exposed to O_2-plasma for 0-10 min and covered by a 200 nm thick Ag film without Cr adhesion layers. The height of the fabricated Ag NP structures is hp ≈ 400 nm. The SERS spectra were recorded before and after exposing the samples to a 1 μL BPE solution. The summarized results are presented in Figure 3.

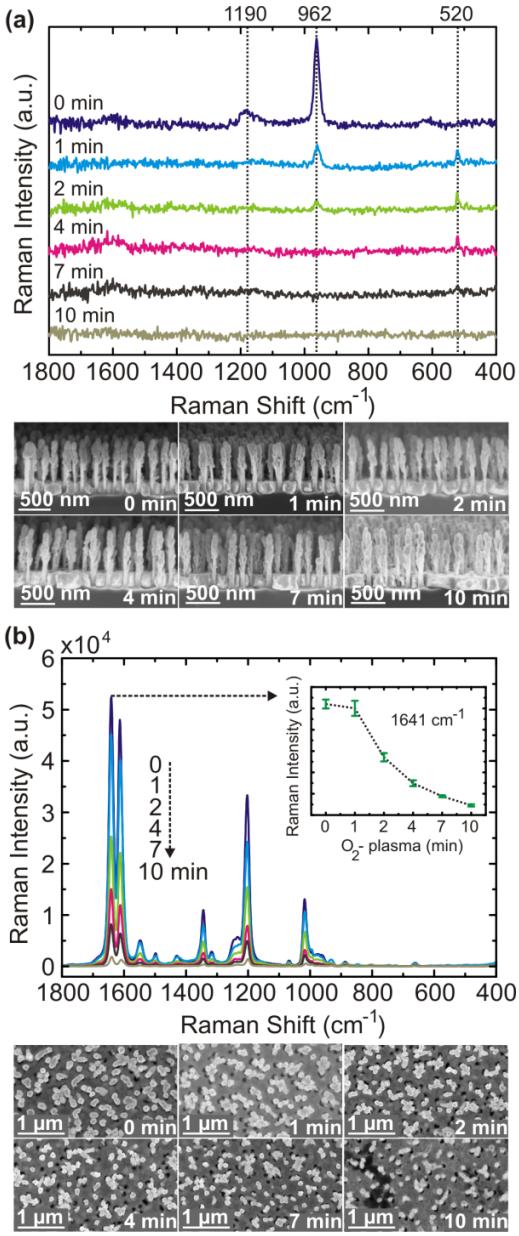

Figure 3. (a) SERS background spectra from Ag NPs after initially exposing Si NPs to an O_2-plasma (t=0-10 min). Bottom: SEM images (side view) of the corresponding Ag NP structures. (b) SERS spectra of BPE acquired using the same Ag NP structures as shown in part a. The inset in part b shows the signal intensity plots for the 1641 cm^{-1} band as a function of the O_2-plasma time measured from five random spots. Bottom: SEM images (top view) that display the corresponding Ag NPs after exposure to BPE, where evaporation of the solvent has forced groups of individual Ag NPs into clusters (see text for details).

Figure 3a shows the SERS spectra from Ag NP substrates treated by O_2-plasma, t=0-10 min. The observed Raman modes at 520, 962, and 1190 cm^{-1} correspond to Si-Si, SiF_3,[47] and Si-O groups,[50] respectively. Treating the samples for 1 min with an O_2-plasma readily reduces the signal from the SiF_3 group by a factor of ~5, and the Si-O signal from the $SiOF_2$ group[50] disappears. For prolonged O_2-plasma exposures (> 4 min), the SiF_3 peak vanishes; see Figure 3a.

To determine the influence of the O_2-plasma step on the SERS signal from the analyte molecules, 1 μL droplets of BPE were deposited and left to dry. The droplets spread over the whole Ag NP surface in several seconds regardless of the O_2-plasma time. Upon solvent drying, capillary forces pull Ag NPs together, causing NP clustering that increases the LSPR coupling between Ag NPs.[41] The results in Figure 3b show that the SERS signal from BPE gradually decreases as the O_2-plasma exposure time is increased. A 4 min exposure to O_2-plasma reduces the SERS intensity by a factor of ~4; thus, the Ag NP EF decreases dramatically. To investigate this, we examined the samples using SEM, see Figure 3(a) and (b). The SEM images reveal considerable Ag NP shape changes that affect the EF of the structure. In particular, the Ag NP cap is transformed into more elongated shapes. After RIE, the Si surface is mostly populated by SiF_x and SiO_2 and the proportion depends on the SF_6/O_2 gas ratio.[52] If the proportion of either O_2 or SF_6 gases in the RIE chamber is significantly increased, the Si surface is then dominated by SiO_2 or SiF_x, respectively. The O_2-plasma treatment gradually transforms SiF_x into SiO_2, which improves the Ag metal adhesion and consequently alters the stiffness of the Ag-coated Si NPs – limiting the cluster formation. The systematically reduced NP cluster size then leads to the decrease of the total EF;[41] see SEM images in Figure 3b.

In order to analyze the influence of the Ag cap shape changes to the cavity LSPR, we performed additional calculations (see Figure S.5, Supporting Information). By stretching the bottom of the Ag cap by 150 nm along the Si pillar, and squeezing the width of the Ag cap by 40 nm, the LSPR peak position of the cavity mode blue-shifts from ~800 to ~750 nm. Since no significant change in the E-field enhancement was observed, we attribute the reduced SERS signal intensities to changes in Ag NP cluster size. To conclude, (i) a 1 min O_2-plasma step removes a substantial amount of SiF_x

contamination while keeping the SERS signal intensity relatively unchanged and (ii) prolonged exposures to O_2-plasma reduce the EF of the structure by gradually shrinking the NP cluster sizes.

4.2 Cr Adhesion Layers

A Cr deposition step is often used to induce a more uniform growth of Ag or Au films on Si or SiO_2 substrates. In this section, we evaluate the influence of a Cr adhesion layer on the Ag NP SERS intensity. All substrates were fabricated using the procedure described in the previous section. The O_2-plasma step was not utilized in this study. A varying thickness of the Cr adhesion layer (0-10 nm) and a 200 nm thick Ag metal film were deposited using e-beam evaporation. All SERS spectra were recorded before and after exposing the Ag NP substrates to BPE.

The results are presented in Figure 4. The SERS background noise from Ag NP structures can be significantly reduced by increasing the thickness of the Cr layer (D_{Cr}), shown in Figure 4a. At D_{Cr} = 6 nm, the signal from the 962 cm^{-1} mode is reduced by a factor of ~4 and the response from both Si-O and SiF_3 groups is negligible at D_{Cr} = 10 nm. Similarly to the O_2-plasma treatment case, SERS signals from BPE decrease gradually as a function of the Cr layer thickness. Although a 3 nm Cr layer is advantageous for reducing background noise, the effect is generally quite small for both the background and the SERS intensity from BPE. In Figure 4b, the recorded SERS signals drop significantly for D_{Cr} > 3 nm, and for D_{Cr} = 10 nm, the SERS intensity is reduced by a factor of ~1.5. Interestingly, the SEM images in Figure 4 a and b reveal that even for thicker Cr layers, e.g., D_{Cr} = 10 nm, Ag cap shapes and stiffness properties remain similar. As expected, the SERS intensity drop is caused by plasmon coupling losses introduced through the Cr adhesion layer. Cr layers introduce loss to the coupling path of the cavity LSPR mode; thus, the corresponding E-field enhancement factor is reduced. We verified these findings using FEM calculations; see Figure S.1 (Supporting Information). The results confirmed that, by replacing the Ag cap cavity material with Cr, the cavity resonance vanishes completely. Overall, the results in Figure 4 indicate that the background decreases primarily due to the reduced SERS performance of the Ag NP structures.

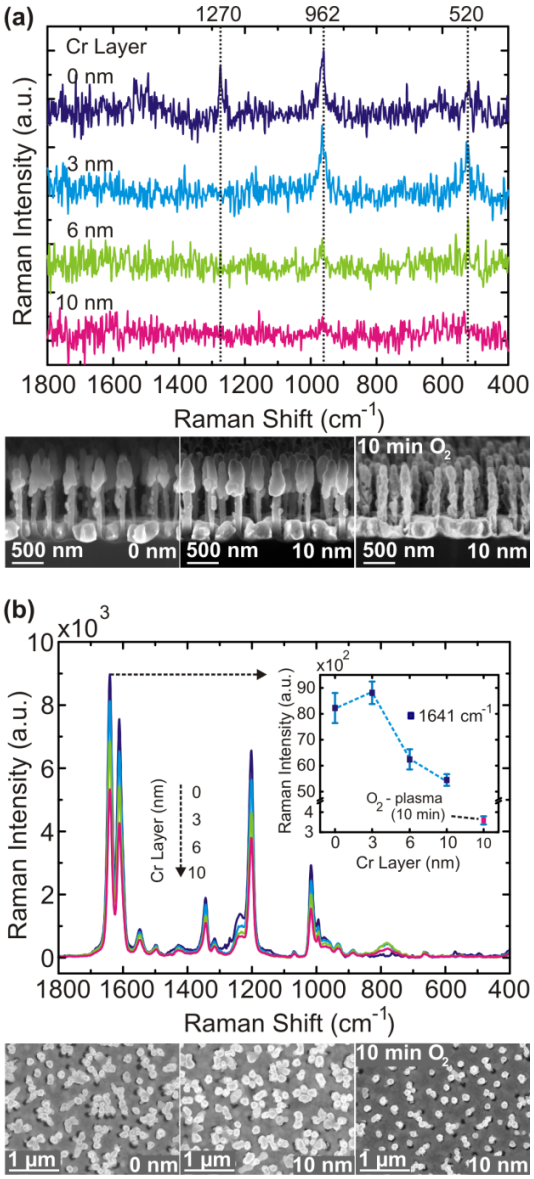

Figure 4. (a) SERS background spectra from Ag NP structures with different Cr layer thicknesses (D_{Cr} = 0 – 10 nm). The Cr coatings were applied to the Si NP structures prior to Ag metal deposition. Bottom: SEM images (side view) for D_{Cr} = 0 and 10 nm, respectively and for using a 10 min O_2-plasma prior to coating of the Si NPs with 10 nm Cr. (b) SERS spectra of BPE using the same structures shown in part a. The inset in part b shows the signal intensity plots for the 1641 cm^{-1} band as a function of the Cr layer thickness measured from five random spots. Bottom: SEM images (top view) illustrate clustering of the Ag NPs after exposure to BPE.

Finally, applying both O_2-plasma and then D_{Cr} = 10 nm reduces the SERS signal from BPE by a factor of >20, Figure 4b. The corresponding SEM image resembles findings in the previous section and further strengthens the explanation that the optical properties of Ag NP substrates are primarily altered via the O_2-plasma step that induces changes in Ag cap shapes and interpillar leaning (Ag NP clustering).

4.3 Height of the Ag NPs

In the previous sections we studied the influence of O_2-plasma treatment and Cr adhesion layers on the SERS performance of leaning Ag NP structures. The results showed that the Ag NP cluster size plays a major role in the enhancement of the Raman signal. In this section, we study the SERS intensity changes caused by an increased Ag NP height. Si NP structures with r = 20 ± 4 nm, ρ_{NP} = 18 ± 2 pillars/μm^2, and varying heights h ≈ 480-1810 nm were fabricated across an entire 4-in. Si wafer. The Si NP height was systematically increased by adjusting the Si RIE process time; see the Experimental Methods section. All Si NP substrates were covered by a 200 nm thick Ag film, yielding Ag NP heights of hp ≈ 280-1610 nm. O_2-plasma and Cr adhesive layer steps were not included in the fabrication process.

The SERS performance of the fabricated Ag NP structures was evaluated using BPE dissolved in ethanol. Since taller Ag NP structures form larger Ag NP clusters, the uniformity of the SERS signal can be affected. We therefore collected line series SERS spectra over a distance of 1 mm; see data in Figure 5 a-e. The results show that the SERS intensity is relatively stable, even though the Ag NP clusters are significantly larger for taller Ag NPs; e.g., see the SEM images for hp = 1210 and 1610 nm. The averaged (100 spectra) SERS intensity for the 1641 cm^{-1} BPE band as a function of the Ag NP height is shown in Figure 5f. The intensity is highest for hp ≈ 390 nm Ag NPs and then gradually decreases with increased Ag NP height. A similar phenomenon can be observed using a 532 nm laser excitation wavelength; i.e., the largest SERS intensity is found for the hp = 390 nm Ag NPs. The observed signal intensity ratio for 780 vs 532 nm excitation wavelengths is close to 1.5:1 (see Figure S.2, Supporting Information). Recalling that the LSPR of the cavity mode for isolated Ag NPs is at λ_{LSPR} = 800 nm, the result is in qualitative agreement with theoretical findings in Figure 1.

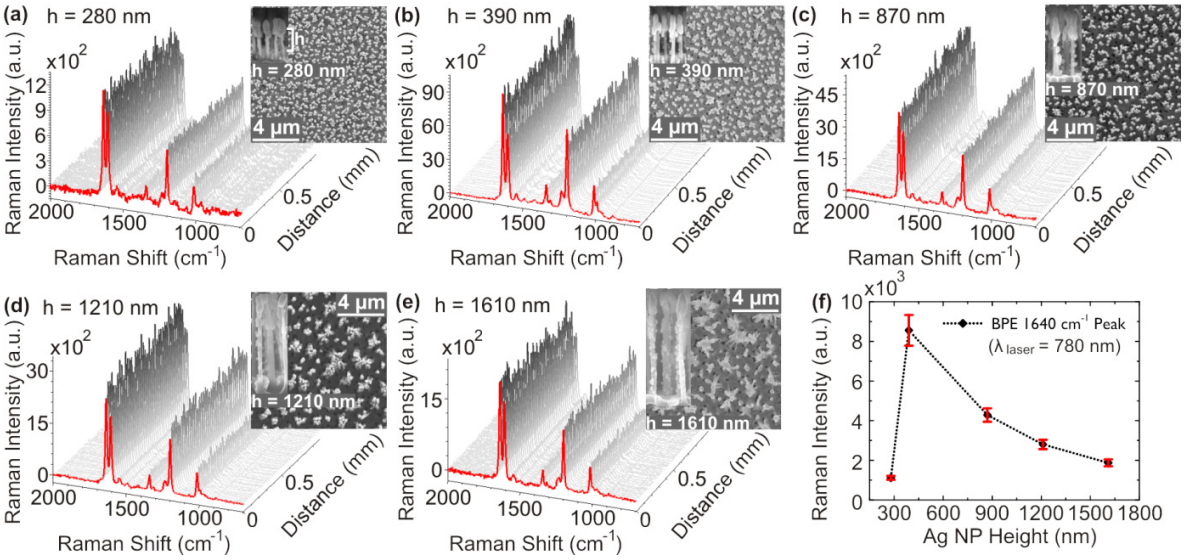

Figure 5. (a-e) Line series SERS spectra of BPE deposited on Ag NP structures with varying NP height (hp ≈ 280-1610 nm). The spectra were collected over a distance of 1 mm with 10 µm steps (40 spectra out of 100 are shown). SEM images illustrate the corresponding Ag NP structures (side view) and clustering of Ag NP after exposure to BPE (top view). (f) The SERS signal intensity plots for the 1641 cm^{-1} band as a function of the Ag NP height averaged over 100 spectra.

Interestingly, an increased Ag NP cluster size has a negative effect on the overall recorded SERS intensity. One explanation could be that BPE molecules are spread over a larger surface area using, e.g., hp = 1610 nm compared to hp = 390 nm Ag NPs. Since Ag NP substrates are hydrophilic toward ethanol, an increase in Ag NP height could lead to inhomogeneous adsorption of BPE; i.e., fewer BPE adsorb on the Ag cap surface due to fast solvent evaporation. This can lead to a different SERS intensity behavior for analytes deposited in gaseous or liquid forms. To verify this, 10 mM thiophenol dissolved in ethanol was evaporated for 10 min on each of the fabricated substrates. After this, leaning of the Ag NPs was induced using 1 µL ethanol droplets. Results showed that the SERS intensity behavior is similar to that observed in Figure 5f (See Figure S.2, Supporting Information).

The SERS intensity variation could be partly influenced by coupling of the Ag NP cap to the Ag film. This effect causes changes in the particle LSPR peak position as a function of the distance to the metal film.[49] Optical interactions of plasmonic particles

coupled to a metal film are most pronounced for particle-film separations of $d \leq 100$ nm.[49] Hu et al. have demonstrated experimentally that, for isolated 60 nm diameter Ag particles, LSPRs can be tuned by adjusting the Au film-particle spacing.[53] Noticeable shifts in the particle LSPR start to occur at $d \approx D$, where d is the film-particle separation distance and D is the particle diameter. In Figure 5 a and b, the separation between the Ag cap and the Ag metal film is close to hp ≈ *2a*; therefore Ag cap plasmon coupling to the Ag metal film can contribute to the observed SERS intensity variation. However, a more detailed study focused on the Ag NP optical properties is required to assess the sharp SERS intensity increase observed at hp = 390 nm.

4.4 Thickness of the Ag Metal Film

In this section, we investigate experimentally the influence of the Ag metal thickness on the E-field enhancement properties of the Ag NP structures. The density of the fabricated Si NPs is kept at $\rho_{NP} \approx 18 \pm 2$ pillars/μm^2, r ≈ 20 ± 4 nm, and h ≈ 600 nm. The O_2-plasma treatment and Cr deposition steps were not included in the Ag NP fabrication process. The thickness of the Ag film (D_{Ag}) was varied between 125 and 300 nm, and SERS intensities for the 1641 cm^{-1} BPE band as a function of the Ag metal thickness are shown in Figure 6a. Small intensity maxima and a sharp peak in the SERS intensity were found at D_{Ag} = 150 and 225 nm, respectively. The SERS intensity for D_{Ag} = 225 nm is increased by a factor of 4 in comparison to the D_{Ag} = 125 nm case. The observed SERS intensity behavior was similar using both 532 and 780 nm laser excitation wavelengths; see Figure S.3 (Supporting Information).

To assess the origin for the sharp SERS intensity rise for D_{Ag} = 225 nm, we examine SEM images for D_{Ag} = 125, 175, 225, and 250 nm; see Figure 6b. First, the images show that increasing D_{Ag} decreases the number of isolated Ag NPs; i.e., for D_{Ag} > 225 nm, nearly all Ag NPs lean toward each other and become a part of large Ag NP conglomerates. For larger D_{Ag}, the surface area of the substrate increases enabling more BPE molecules to bind, enhancing the SERS intensity. Second, the shape of the Ag cap is transformed toward more elongated shapes. According to our theoretical findings, if the Ag ellipsoid dimension, *a,* is increased, the LSPR of the cavity mode blue-shifts toward the 780 nm excitation laser wavelength. The experimental data is in accordance with

previous claims that the main contribution of the Ag NP EF comes from the NP cavity mode, whose resonance is close to 800 nm; see Figure 1.

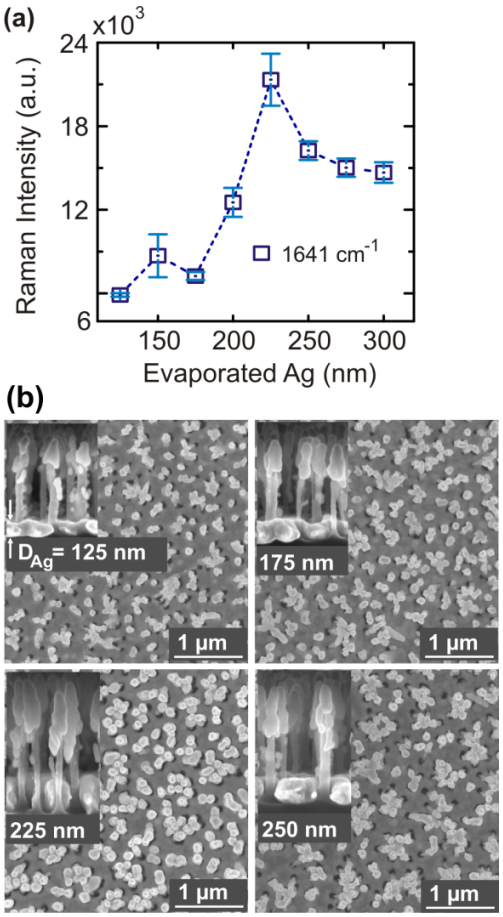

Figure 6. (a) SERS signal intensity plots for the 1641 cm^{-1} BPE band as a function of the Ag layer thickness measured from five random spots. The Ag metal thickness was varied between D_{Ag} = 125 and 300 nm. (b) SEM images (top view) illustrate clustering of the Ag NPs after BPE deposition and solvent drying. The Insets in part b show the Ag NP structures prior to exposure to BPE.

4.5 Optimized Ag NP Structures for SERS Applications

Finally, all process optimizations for the Ag NP fabrication were integrated to fabricate substrates that exhibit the highest SERS intensity and uniformity over a 4-in. wafer. In order to verify that all experimental findings in previous sections can be consistently combined, we prepared two identical Ag NP substrate sets with $\rho_{NP} \approx 18 \pm 2$ pillars/μm^2, r ≈ 20 ± 4 nm, and hp ≈ 390 nm. The Si NP structures were then exposed to

an O_2-plasma for 1 and 1.5 min, respectively, followed by deposition of 3 nm thick Cr layers. The Ag metal thickness D_{Ag} was then varied between 210 and 255 nm for both sample sets, i.e., around the D_{Ag} = 225 nm value that yields the highest SERS intensity; see Figure 6a.

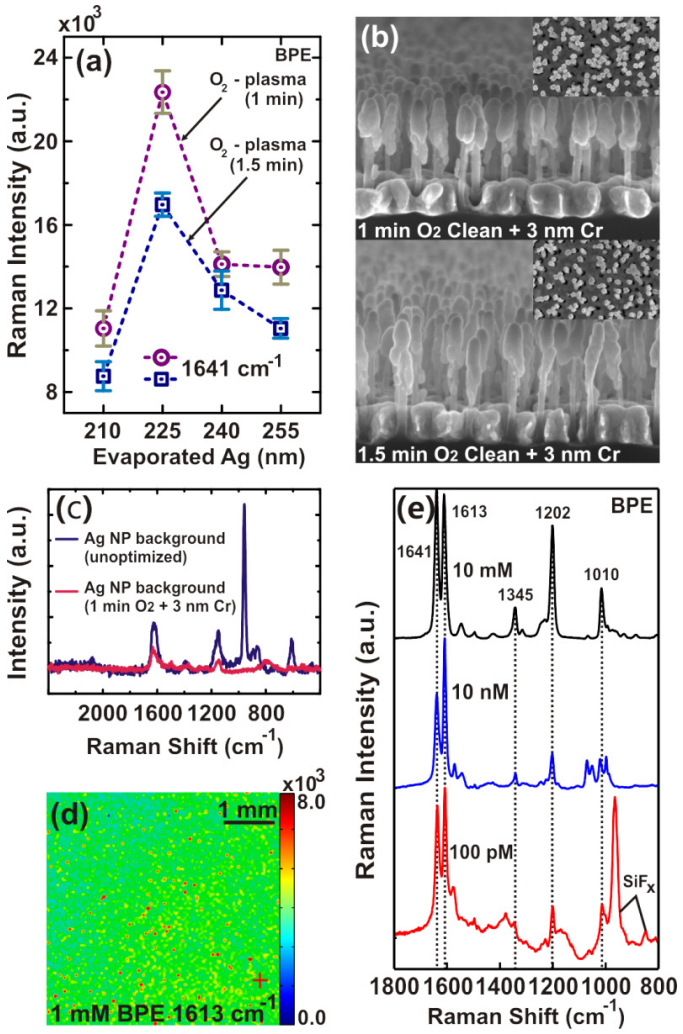

Figure 7. (a) SERS intensity plots of the 1641 cm^{-1} BPE mode for Ag NPs with varying Ag metal thickness. Prior to metal depositions, the Si NPs were exposed to an O_2-plasma for 1 and 1.5 min. (b) SEM images showing Ag NPs treated with O_2-plasma, D_{Ag} = 225 nm. Side and top views show the structures before and after exposure to BPE, respectively. (c) The influence of O_2-plasma treatment and Cr layer deposition on the SERS signal from the Ag NPs. (d) Evaluation of the SERS signal uniformity using the optimized Ag NP substrate, i.e., D_{Ag} = 225 nm, hp = 390 nm, 1 min O_2-plasma, and 3 nm Cr. (e) SERS spectra of BPE at low concentrations using the optimized Ag NP structures.

A summary of the SERS signal intensity changes for the two sample sets is shown in Figure 7a. Results confirm that the SERS intensity is extremely sensitive to O_2-plasma treatment for all evaluated Ag metal thicknesses. For D_{Ag} = 225 nm, an additional 30 s exposure to O_2-plasma results in an ~30% decrease in the signal intensity. SEM images in Figure 7b reveal that the Ag cap shape is more elongated for the 1.5 min O_2-plasma case. As a result, the Ag NP cluster size is reduced, which translates into poorer Ag NP enhancement properties.

Results in the sections 4.1 and 4.2 showed that a 1 min O_2-plasma step and a 3 nm Cr layer are useful for reducing SERS signals from the Si RIE induced surface contaminations, as seen in Figures 3 and 4, respectively. Indeed, the results in Figure 7c confirm that the aforementioned Si surface treatment steps are advantageous. Prior to collecting the SERS spectra, the Ag NP structures (D_{Ag} = 225 nm) were preleaned using 1 μL of DI water to induce the Ag NP cluster formation and then the SERS signal from the Ag NP structures without analyte molecules was recorded. An identical Ag NP substrate without the O_2-plasma and Cr deposition steps was measured for comparison (Figure 7(c)). The Raman scattering peaks at 962 cm^{-1} (SiF_3), 1151 cm^{-1} (Si-O), 1640 cm^{-1} (C=C), and 2080 cm^{-1} (Si-C)[47, 48] are significantly reduced in intensity. The weak Raman mode appearing at 800 cm^{-1} for the SF_6/O_2 plasma treated sample corresponds to the SiF group.[47]

In order to investigate the SERS signal uniformity, 1 μL of BPE was dispersed on a surface of optimized Ag NPs, i.e., 1 min O_2-plasma, D_{Cr} = 3 nm, and D_{Ag} = 225 nm. In Figure 7d, the SERS intensity map over a 5 × 5 mm^2 surface area for a 1613 cm^{-1} BPE vibrational mode is shown. The standard deviation for the displayed Raman scattering peak is around 14%, and the recorded signal uniformity is highly reproducible over a surface area of ~3.2-in. in diameter on a 4-in. Ag NP substrate.

The molecular detection limit of the experimentally optimized leaning Ag NP substrates was evaluated using different concentrations of BPE; see results in Figure 7e. Analyte concentrations down to 100 pM can be detected displaying all five distinct BPE Raman bands at 1641, 1613, 1202, and 1010 cm^{-1}. Note that some BPE Raman modes split, e.g., the 1010 cm^{-1} peak in the 10 nM BPE spectrum. This is likely caused by a high energy density that induces photochemistry reactions on the Ag surface, leading to

decomposition of the analyte molecules.[51] The EF for the optimized Ag NP structures was then calculated according to

$$EF = \frac{I_{SERS}/N_{SERS}}{I_{ref}/N_{ref}} \quad (1)$$

where I_{SERS} is the SERS intensity, N_{SERS} is the number of corresponding molecules within the laser spot, I_{ref} is the reference Raman signal intensity, and N_{ref} is the number of molecules responsible for the Raman scattering signal.[34] The obtained EF was 1.3×10^8, see the calculation details in the Supporting Information.

5 Conclusions

In this paper, we report the fabrication steps that are important for achieving high SERS intensity and uniformity in the leaning Ag NP structures fabricated using maskless lithography. The fabrication process contains four simple, cost-effective and quick steps that are compatible with high volume manufacturing process flows: (i) Si RIE, (ii) O_2-plasma treatment, (iii) deposition of the Cr adhesion layer, and (iv) evaporation of the Ag metal. First, the nature of the E-field enhancement in isolated Ag NPs was theoretically investigated using FEM. Calculations showed that the optical properties of single Ag NPs are dominated by a distinct Ag cap cavity resonance mode found close to ~800 nm. The resonance position can primarily be tuned via the diameter of the Si NP. The near-field plots produced at the resonance showed that the incident field is spatially confined at the Ag cap cavity, i.e., at the bottom of the Ag cap. This allowed us to attribute the E-field enhancement in Ag NPs to plasmon coupling between Ag cap cavity LSPRs that contribute most to the enhancement of the Raman signal. Moreover, since these hot spots are located at the Ag-Si interface, we established that the measured background noise from the Ag NPs corresponds to Si RIE byproducts that populate the Si NP surface.

We then showed experimentally that the O_2-plasma process and Cr adhesion layers can be used to improve the SERS signal intensity and reduce the contribution from the Si surface contaminants. Importantly, by controlling the O_2-plasma exposure time, the background noise from Ag NPs can be significantly reduced. However, a prolonged exposure to the O_2-plasma induces a more uniform Ag growth on Si NPs, which produces elongated Ag cap shapes. Consequently, the Ag NP cluster size, thus the SERS intensity,

is systematically reduced. The Cr adhesion layer (3 nm) can also be utilized to further reduce the contribution from the contaminated Si NP surface. However, thicker Cr layers (>3 nm) introduce loss which weakens the plasmon coupling in the Ag cavity. Moreover, by adjusting the Si NP height and thickness of the evaporated Ag film, we found that the SERS intensity can be systematically varied.

Finally, we combined all our experimental findings and presented a recipe to fabricate Ag NP structures that exhibit the highest SERS intensity. The Raman scattering signal was then recorded over a larger surface area with standard deviations of ~14% across a 5 mm × 5 mm chip. The result was reproducible over an ~3.2-in. in diameter surface area. We tested the substrate performance by recording BPE spectra down to a concentration of 100 pM, displaying clear Raman vibration modes specific to BPE.

Experimental findings suggest that the Ag NP substrates are strong candidates for obtaining a reliable SERS detection of molecular species at ultra-low concentrations. We emphasize that the nanofabrication process is simple, cost-effective, and CMOS compatible and could be suitable for mass-production in standard IC foundries utilizing even larger Si carrier wafers.

6 Supporting Information

Supporting Information Available: Calculated absorbance spectra and E-field maps for isolated Ag NPs that show the influence of the Ag cap cavity material (Cr and Si) on the cavity LSPR; SERS spectra of thiophenol on Ag NPs with varying NP height; SERS signal intensity plots for the 1641 cm^{-1} BPE band as a function of the Ag layer thickness measured using the 532 nm laser excitation wavelength; SERS spectra of thiophenol on leaned and nonleaned (isolated) Ag NPs; calculated E-field enhancement distributions ($|E|/|E_0|$) around a single Ag NP and a NP dimer; calculated scattering spectra of a standard Ag NP and an Ag NP with an elongated Ag cap; evaluation of the Raman enhancement factor (EF) for the optimized substrate.

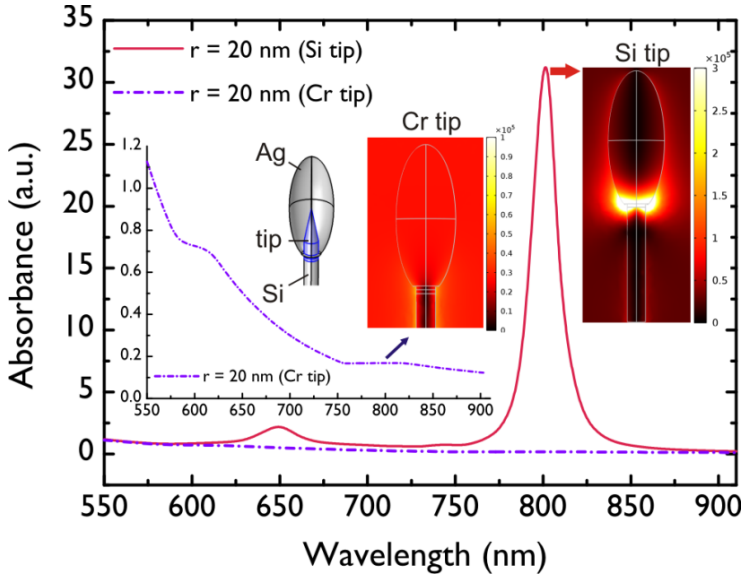

Figure S.1. Calculated absorbance spectra and E-field maps for isolated Ag NPs that show the influence of the Ag cap cavity material (Cr and Si) on the cavity LSPR.

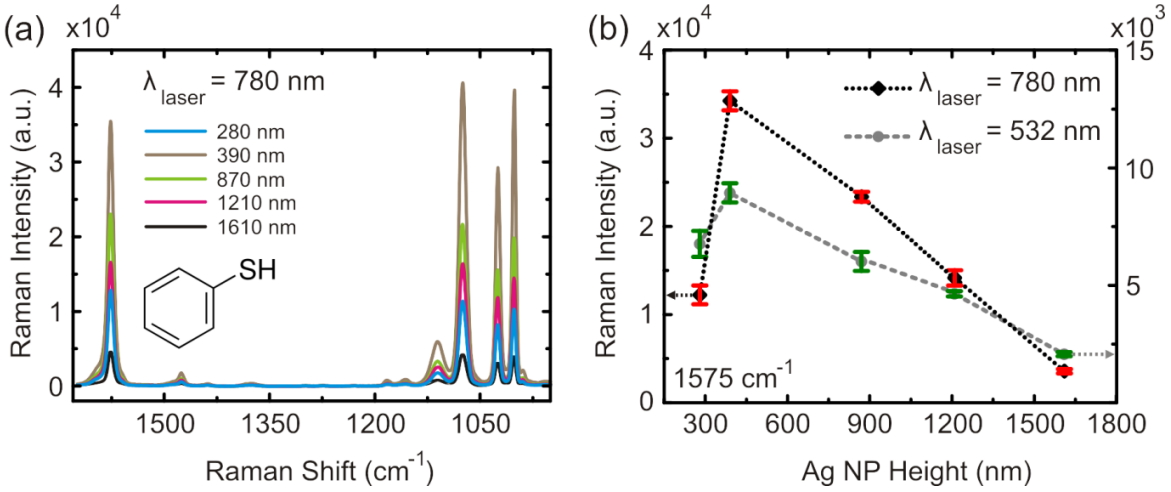

Figure S.2. (a) SERS spectra of thiophenol on Ag NPs with varying NP height (hp ≈ 280-1610 nm). 10 mM thiophenol dissolved in ethanol was evaporated for 10 min onto each of the fabricated substrates. After the evaporation step, Ag NP leaning was induced using a 1 µL ethanol droplet. (b) 1575 cm^{-1} thiophenol peak intensity from 5 random points plotted vs. the Ag NP height for 532 and 780 nm laser excitation wavelengths.

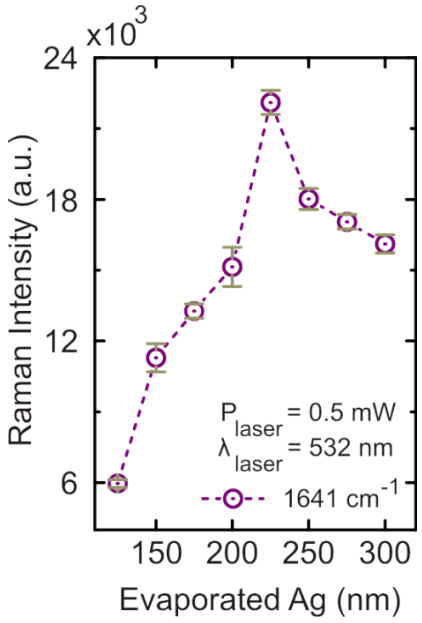

Figure S.3. SERS signal intensity plots for the 1641 cm^{-1} BPE band as a function of the Ag layer thickness measured from 5 random spots using the 532 nm laser excitation wavelength. The Ag metal thickness was varied between D_{Ag} = 125 and 300 nm.

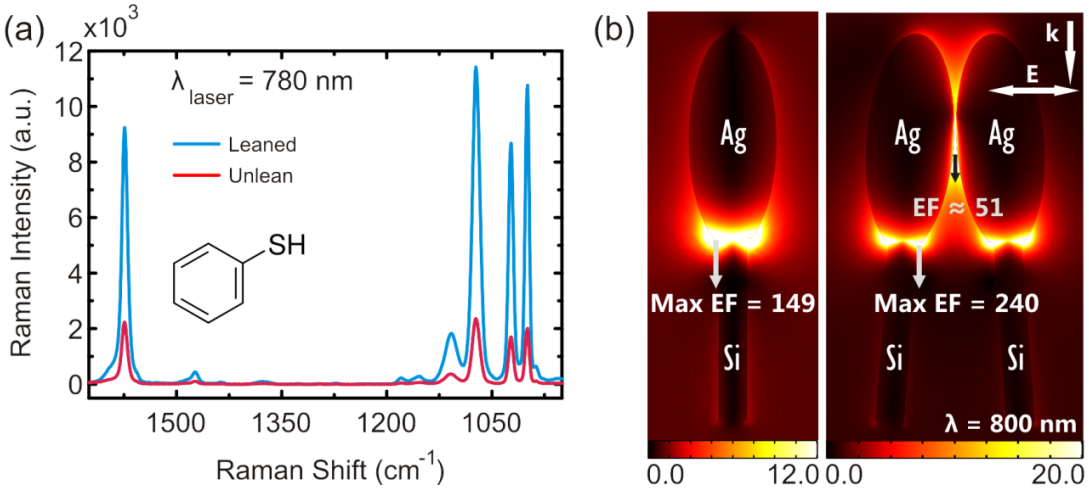

Figure S.4. (a) SERS spectra of thiophenol on leaned and non-leaned (isolated) Ag NPs with hp ≈ 280 nm. 10 mM thiophenol dissolved in ethanol was evaporated for 10 min onto the fabricated substrates. After the evaporation step, Ag NP leaning was induced using a 1 µL ethanol droplet. Spectra are obtained before and after leaning of the NPs. (b) The calculated E-field enhancement distributions ($|E|/|E_0|$) around a single Ag NP and a NP dimer at λ = 800 nm. The Ag NP parameters used were the same as in figure 1b for r = 20 nm. For the dimer case, the minimum distance between the two NPs is 1 nm. It can be seen from (a) that isolated NPs provide a SERS signal which is lowered by a factor of ~5 compared with that of the leaning NPs. This supports that the Ag cap cavities contribute most to the overall SERS signal. In addition, it can be seen from (b) that leaning increases the maximum EF of the cavity mode from 149 to 240, and introduces additional hot-spots in the nano gaps between the NPs with EFs of ~51 which are smaller than that of the cavity mode. Therefore, it can be concluded that the Ag cap cavity and the nano gaps both contributes to the SERS signal. The field maps also suggest that the Ag cap cavity mode is the main contributor to the overall SERS signal.

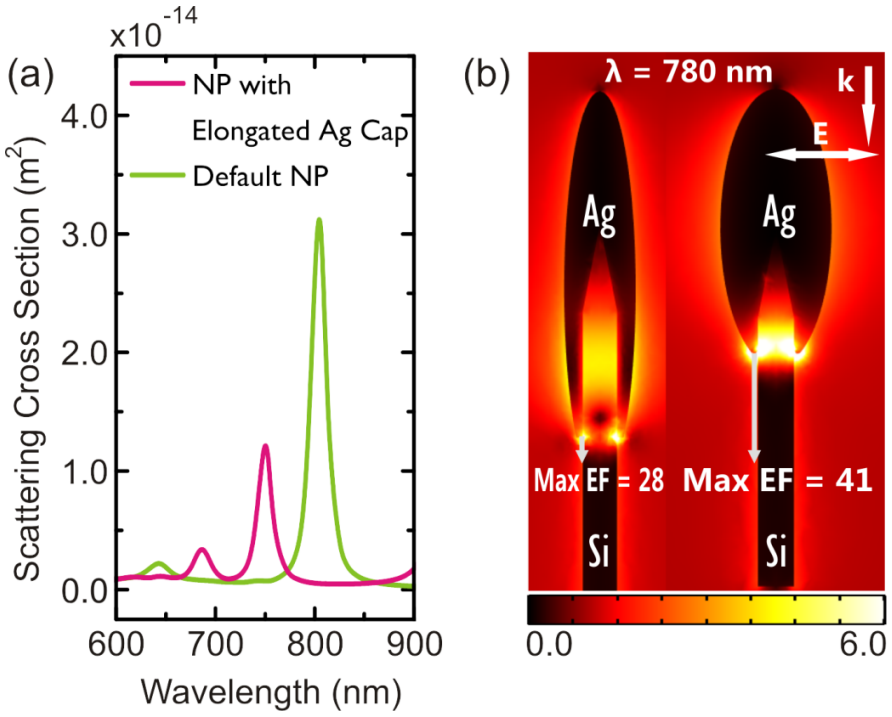

Figure S.5. (a) Calculated scattering spectra of a standard (default) Ag NP and an Ag NP with an elongated Ag cap. Parameters for the former was the same as in figure 1b for r = 20 nm. The elongated NP is modeled by stretching the bottom of the Ag cap by 150 nm along the Si pillar, and by squeezing the width of the Ag cap by 40 nm. (b) The calculated E-field enhancement distribution ($|E|/|E_0|$) around a standard Ag NP and an Ag NP with an elongated Ag cap at λ = 780 nm excitation.

The Raman enhancement factor (EF) for the optimized substrate was calculated from the formula:

$$EF = \frac{I_{SERS}/N_{SERS}}{I_{ref}/N_{ref}}$$

The numbers used in the calculation are obtained using the method described in reference 34. To be specific, to establish the value for I_{Ref} a 0.1 M ethanol solution of trans-1,2-Bis(4-pyridyl)ethylene (BPE) was poured into a petri dish. With a 50X objective and using an excitation wavelength of 780 nm and a power of 1mW, 1.4 counts/s (I_{Ref}) were measured at the 1200 cm^{-1} peak. Using the interaction volume of 60 μm^3, the number of molecules responsible for the Raman signal (N_{Ref}) was estimated to be 3.60 x 10^9.

To establish the values for I_{SERS} a 5 x 5 mm^2 piece of the optimized silver coated nanopillar substrate with a pillar density of ~18 μm^{-2} was immersed into a 10 mM

ethanolic solution of BPE for 15 minutes. Hereafter, the substrate was removed and dried in air. After drying, the substrate was rinsed in ethanol. Using identical conditions as for I_{Ref}, a signal intensity of 50000 counts/s was measured for the 1200 cm^{-1} peak. The number of molecules inside the laser spot was estimated by assuming a monolayer of BPE all over the substrate. A packing density of 3.3 x 10^6 BPE molecules/μm^2 was used for this calculation.[55] With a laser spot size with a radius of 0.8 μm and taking the topography of the silver surface on the Si pillar into consideration, the effective surface area probed by the laser was 0.3 μm^2. This gives an estimate of $N_{SERS} = 10^6$ molecules. Hence, the calculated EF becomes 1.3 x 10^8.

7 Acknowledgement

This work has been funded by the NAPLAS project, The Danish Council for Independent Research. K. B. Mogensen is thankful for support from The Danish National Advanced Technology Foundation (HTF, grant no. 083-2012-1). The manuscript was written through contributions of all authors. All authors have given approval to the final version of the manuscript. Authors would like to thank Prof. Mikael Käll and Stephan S. Keller for stimulating discussions and comments. The authors declare no competing financial interest.

References

(1) Sharma, B.; Cardinal, M. F.; Kleinman, S. L.; Greeneltch, N. G.; Frontiera, R. R.; Blaber, M. G.; Schatz, G. C.; Van Duyne, R. P. High-performance SERS Substrates: Advances and Challenges. *MRS Bull*. **2013**, *38*, 615-624.

(2) Le Ru, E. C.; Meyer, M.; Etchegoin, P. G. Proof of Single-Molecule Sensitivity in Surface Enhanced Raman Scattering (SERS) by Means of a Two-Analyte Technique. *J. Phys. Chem. B* **2006**, *110*, 1944-1948.

(3) Abalde-Cela, S.; Aldeanueva-Potel, P.; Mateo-Mateo, C.; Rodríguez-Lorenzo, L.; Alvarez-Puebla, R. A.; Liz-Marzán, L. M. Surface-enhanced Raman Scattering Biomedical Applications of Plasmonic Colloidal Particles. *J. R. Soc., Interface* **2010**, *7*, S435-S450.

(4) Hutter, E.; Fendler, J. H. Exploitation of Localized Surface Plasmon Resonance. *Adv. Mater*. **2004**, *16*, 1685-1706.

(5) Willets, K. A.; Van Duyne, R. P. Localized Surface Plasmon Resonance Spectroscopy and Sensing. *Annu. Rev. Phys. Chem*. **2007**, *58*, 267-297.

(6) Mayer, K. M.; Hafner, J. H. Localized Surface Plasmon Resonance Sensors. *Chem. Rev.* **2011**, *111*, 3828-3857.

(7) Xu, H.; Aizpurua, J.; Käll, M.; Apell, P. Electromagnetic Contributions to Single-molecule Sensitivity in Surface-enhanced Raman Scattering. *Phys. Rev. E* **2000**, *62*, 4318-4324.

(8) Ye, X.; Zheng, C.; Chen, J.; Gao, Y.; Murray, C. B. Seeded Growth of Monodisperse Gold Nanorods Using Bromide-Free Surfactant Mixtures. *Nano Lett.* **2013**, *13*, 2163-2171.

(9) Rycenga, M.; Xia, X.; Moran, C. H.; Zhou, F.; Qin, D.; Li, Z.-Y.; Xia, Y. Generation of Hot Spots with Silver Nanocubes for Single-Molecule Detection by Surface-Enhanced Raman Scattering. *Angew. Chem. Int. Ed*. **2011**, *50*, 5473-5477.

(10) Khoury, C. G.; Vo-Dinh, T. Gold Nanostars for Surface-Enhanced Raman Scattering: Synthesis, Characterization and Optimization. *J. Phys. Chem. C* **2008**, *112*, 18849-18859.

(11) Bastús, N. G.; Comenge, J.; Puntes, V. C. Kinetically Controlled Seeded Growth Synthesis of Citrate-Stabilized Gold Nanoparticles of up to 200 nm: Size Focusing versus Ostwald Ripening. *Langmuir*. **2011**, *27*, 11098-11105.

(12) Zhang, J.; Gao, Y.; Alvarez-Puebla, R. A.; Buriak, J. M.; Fenniri, H. Synthesis and SERS Properties of Nanocrystalline Gold Octahedra Generated from Thermal Decomposition of $HAuCl_4$ in Block Copolymers. *Adv. Mater*. **2006**, *18*, 3233-3237.

(13) Wang, H.; Levin, C. S.; Halas, N. J. Nanosphere Arrays with Controlled Sub-10-nm Gaps as Surface-Enhanced Raman Spectroscopy Substrates. *J. Am. Chem. Soc*. **2005**, *127*, 14992-14993.

(14) Langille, M. R.; Personick, M. L.; Zhang, J.; Mirkin, C. A. Defining Rules for the Shape Evolution of Gold Nanoparticles. *J. Am. Chem. Soc*. **2012**, *134*, 14542-14554.

(15) Lim, D.-K.; Jeon, K.-S.; Hwang, J.-H.; Kim, H.; Kwon, S.; Suh, Y. D.; Nam, J.-M. Highly Uniform and Reproducible Surface-enhanced Raman Scattering from DNA-tailorable Nanoparticles with 1-nm Interior Gap. *Nat. Nanotechnol.* **2011**, *6*, 452-460.

(16) Kühler, P.; Roller, E.-M.; Schreiber, R.; Liedl, T.; Lohmüller, T.; Feldmann, J. Plasmonic DNA-Origami Nanoantennas for Surface-Enhanced Raman Spectroscopy. *Nano Lett*. **2014**, *14*, 2914-2919.

(17) He, L.; Lin, M.; Li, H.; Kim, N.-J. Surface-enhanced Raman Spectroscopy Coupled with Dendritic Silver Nanosubstrate for Detection of Restricted Antibiotics. *J. Raman Spectrosc*. **2010**, *41*, 739-744.

(18) Lim, D.-K.; Jeon, K.-S.; Kim, H. M.; Nam, J.-M.; Suh, Y. D. Nanogap-engineerable Raman-active Nanodumbbells for Single-molecule Detection. *Nat. Mater*. **2010**, *9*, 60-67.

(19) Le Ru, E. C.; Etchegoin, P. G. Single-Molecule Surface-Enhanced Raman Spectroscopy. *Annu. Rev. Phys. Chem*. **2012**, *63*, 65-87.

(20) Xu, H.; Bjerneld, E. J.; Käll, M.; Borjesson, L. Spectroscopy of Single Hemoglobin Molecules by Surface Enhanced Raman Scattering. *Phys. Rev. Lett*. **1999**, *83*, 4357-4360.

(21) Betz, J. F.; Yu, W. W.; Cheng, Y.; White, I. M.; Rubloff, G. W. Simple SERS Substrates: Powerful, Portable, and Full of Potential. *Phys. Chem. Chem. Phys.* **2014**, *16*, 2224-2239.

(22) Zhang, X.; Yonzon, C. R.; Van Duyne, R. P. Nanosphere Lithography Fabricated Plasmonic Material and their Applications. *J. Mater. Res*. **2006**, *21*, 1083-1092.

(23) Abu Hatab, N. A.; Oran, J. M.; Sepaniak, M. J. Surface-Enhanced Raman Spectroscopy Substrates Created via Electron Beam Lithography and Nanotransfer Printing. *ACS Nano*. **2008**, *2*, 377-385.

(24) Sánchez-Iglesias, A.; Aldeanueva-Potel, P.; Ni, W.; Pérez-Juste, J.; Pastoriza-Santos, I.; Alvarez-Puebla, R. A.; Mbenkum, B. N.; Liz-Marzán, L. M. Chemical Seeded Growth of Ag Nanoparticle Arrays and their Application as Reproducible SERS Substrates. *Nano Today*. **2010**, *5*, 21-27.

(25) Greeneltch, N.; Blaber, M.; Henry, A-I.; Schatz, G.; Van Duyne, R. P. Immobilized Nanorod Assemblies: Fabrication and Understanding of Large Area Surface-enhanced Raman Spectroscopy Substrates. *Anal. Chem*. **2013**, *85*, 2297-2303.

(26) Oh, Y.-J.; Jeong, K.-H. Glass Nanopillar Arrays with Nanogap-Rich Silver Nanoislands for Highly Intense Surface Enhanced Raman Scattering. *Adv. Mater*. **2012**, *24*, 2234-2237.

(27) Le Ru, E. C.; Etchegoin, P. *Principles of Surface Enhanced Raman Spectroscopy and related Plasmonic Effects*; Elsevier: Amsterdam, The Netherland, **2008**.

(28) Shumaker-Parry, J. S.; Rochholz, H.; Kreiter, M. Fabrication of Crescent-Shaped Optical Antennas. *Adv. Mater*. **2005**, *17*, 2131-2134.

(29) Wu, L. Y.; Ross, B. M.; Lee, L. P. Optical Properties of the Crescent-shaped Nanohole Antenna. *Nano Lett*. **2009**, *9*, 1956-1961.

(30) Dinish, U. S.; Yaw, F. C.; Agarwal, A.; Olivo, M. Development of Highly Reproducible Nanogap SERS Substrates: Comparative Performance Analysis and its Application for Glucose Sensing. *Biosens. Bioelectron*. **2011**, *26*, 1987-1992.

(31) Im, H.; Bantz, K. C.; Lindquist, N. C.; Haynes, C. L.; Oh, S.-H. Vertically Oriented Sub-10-nm Plasmonic Nanogap Arrays. *Nano lett*. **2010**, *10*, 2231-2236.

(32) Caldwell, J. D.; Glembocki, O.; Bezares, F. J.; Bassim, N. D.; Rendell, R. W.; Feygelson, M.; Ukaegbu, M.; Kasica, R.; Shirey, L.; Hosten, C. Plasmonic Nanopillar Arrays for Large-Area, High-Enhancement Surface-Enhanced Raman Scattering Sensors. *ACS Nano* **2011**, *5*, 4046-4055.

(33) Ruan, C.; Eres, G.; Wang, W.; Zhang, Z.; Gu, B. Controlled Fabrication of Nanopillar Arrays as Active Substrates for Surface-enhanced Raman Spectroscopy. *Langmuir*. **2007**, *23*, 5757-5760.

(34) Hu, M.; Ou, F. S.; Wu, W.; Naumov, I.; Li, X.; Bratkovsky, A. M.; Williams, R. S.; Li, Z. Gold Nanofingers for Molecule Trapping and Detection. *J. Am. Chem. Soc*. **2010**, *132*, 12820-12822.

(35) Huang, Z.; Meng, G.; Huang, Q.; Yang, Y.; Zhu, C.; Tang, C. Improved SERS Performance from Au Nanopillar Arrays by Abridging the Pillar Tip Spacing by Ag Sputtering. *Adv. Mater*. **2010**, *22*, 4136-4139.

(36) Mao, H.; Wu, W.; She, D.; Sun, G.; Lv, P.; Xu, J. Microfluidic Surface-Enhanced Raman Scattering Sensors Based on Nanopillar Forests Realized by an Oxygen-Plasma-Stripping-of-Photoresist Technique. *Small*. **2014**, *10*, 127-134.

(37) Gartia, M. R.; Xu, Z.; Behymer, E.; Nguyen, H.; Britten, J. A.; Larson, C.; Miles, R.; Bora, M.; Chang, A. S.-P.; Bond, T. C.; Liu, G. L. Rigorous Surface Enhanced Raman Spectral Characterization of Large-area High-uniformity Silver-coated Tapered Silica Nanopillar Arrays. *Nanotechnology*. **2010**, *21*, 395701.

(38) Bora, M.; Fasenfest, B. J.; Behymer, E. M.; Chang, A. S.-P.; Nguyen, H. T.; Britten, J. A.; Larson, C. C.; Chan, J. W.; Miles, R. R.; Bond, T. C. Plasmon Resonant Cavities in Vertical Nanowire Arrays. *Nano Lett*. **2010**, *10*, 2832-2837.

(39) Dawson, P.; Duenas, J. A.; Boyle, M. G.; Doherty, M. D.; Bell, S. E. J.; Kern, A. M.; Martin, O. J. F.; Teh, A.-S.; Teo, K. B. K.; Milne, W. I. Combined Antenna and Localized Plasmon Resonance in Raman Scattering from Random Arrays of Silver-Coated, Vertically Aligned Multiwalled Carbon Nanotubes. *Nano Lett*. **2011**, *11*, 365-371.

(40) Yang, X.; Ileri, N.; Larson, C. C.; Carlson, T. C.; Britten, J. A.; Chang, A. S. P.; Gu, C.; Bond, T. C. Nanopillar Array on a Fiber Facet for Highly Sensitive Surface-enhanced Raman Scattering. *Opt. Express*. **2012**, *20*, 24819-24826.

(41) Schmidt, M. S.; Hübner, J.; Boisen, A. Large Area Fabrication of Leaning Silicon Nanopillars for Surface Enhanced Raman Spectroscopy. *Adv. Mater*. **2012**, *24*, OP11-OP18.

(42) Yang, J.; Palla, M.; Bosco, F. G.; Rindzevicius, T.; Alstrøm, T. S.; Schmidt, M. S.; Boison, A.; Ju, J.; Lin, Q. Surface-Enhanced Raman Spectroscopy Based Quantitative Bioassay on Aptamer-Functionalized Nanopillars Using Large-Area Raman Mapping. *ACS Nano*. **2013**, *7*, 5350-5359.

(43) Johnson, P. B.; Christy, R. W. Optical Constants of the Noble Metals. *Phys. Rev. B*. **1972**, *6*, 4370-4379.

(44) Bass, M.; DeCusatis, C.; Enoch, J.; Lakshminarayanan, V.; Li, G.; MacDonald, C.; Mahajan, V.; Van Stryland, E. *Handbook of Optics, 3rd ed*.; McGraw-Hill Professional: New York **2009**.

(45) Wu, K.; Cheng, X.; Lee, L. P. Intra-particle Coupling and Plasmon Tuning of Multilayer Au/dielectric/Au Nanocrescents Adhered to a Dielectric Cylinder. *Nanotechnology*, **2012**, *23*, 055201.

(46) Cardinal, M. F.; Rodríguez-González, B.; Alvarez-Puebla, R. A.; Pérez-Juste, J.; Liz-Marzán, L. M. Modulation of Localized Surface Plasmons and SERS Response in Gold Dumbbells through Silver Coating. *J. Phys. Chem. C*. **2010**, *114*, 10417-10423.

(47) Colthup, N. B.; Daly, L. H.; Wiberley, S. E. *Introduction to Infrared and Raman Spectroscopy, 3rd Edition*. Academic Press: San Diego, U.S., **1990**.

(48) Lin-Vien, D.; Colthup, N. B.; Fateley, W. G.; Grasselli, J. G. *The Handbook of Infrared and Raman Characteristic Frequencies of Organic Molecules*. Academic Press: Boston, U.S., **1991**.

(49) Lévêque, G.; Marti52n, O. J. Optical Interactions in a Plasmonic Particle Coupled to a Metallic Film. *Optics Express,* **2006**, *14*, 9971-9981.

(50) Reiche, M.; Wiegand, M.; Gösele, U. Infrared Spectroscopic Analysis of Plasma-treated Si(100)-surfaces. *Microchimica Acta*. **2000**, *133*, 35-43.

(51) Alaverdyan, Y.; Johansson, P.; Käll, M. Photo-induced Transformations in 2,2':5',2''-Terthiophene Thin Films on Silver. *Phys. Chem. Chem. Phys.* **2006**, *8*, 1445-1450.

(52) d'Agostino, R.; Flamm, D. L. Plasma Etching of Si and SiO_2 in SF_6-O_2 Mixtures. *J. Appl. Phys.* **1981**, *52*, 162-167.

(53) Hu, M.; Ghoshal, A.; Marquez, M.; Kik, P. G. Single Particle Spectroscopy Study of Metal-Film-Induced Tuning of Silver Nanoparticle Plasmon Resonances. *J. Phys. Chem. C*. **2010**, *114*, 7509-7515.

CHAPTER 8

MACROSCALE SERS UNIFORMITY AND REPRODUCIBILITY USING DENSELY CLUSTERED NANOPILLARS [P3]

Kaiyu Wu*, Tomas Rindzevicius, Michael Stenbæk Schmidt,
Anil Haraksingh Thilsted, and Anja Boisen

Technical University of Denmark, Department of Micro- and Nanotechnology
Ørsteds Plads, Building 345B
2800 Kgs. Lyngby, Denmark
*kaiwu@nanotech.dtu.dk

Under review

The ideal surface-enhanced Raman spectroscopy (SERS) substrate should fulfil the following: i) predictable SERS enhancement, ii) macroscale SERS signal uniformity, and iii) suitability for mass production with excellent reproducibility. We have previously shown that SERS-active nanopillar structures, fabricated by lithography-free processes, show high average SERS enhancements ($>10^8$) and are mass producible. Here we report an improved process and show that these structures exhibit unrivalled macroscale SERS uniformities (RSD: ~2.5% in mm scale, ~7% in inch scale) and SERS reproducibilities (RSD: ~1.5% across three wafers), while at the same time obtaining a very large average enhancement factor of $>10^8$. We also show a simple example of fast and reliable SERS analysis of low-volume analytes using such structures. We emphasize that the nanofabrication process is cost-effective, and is suitable for mass production in standard IC foundries using even larger silicon wafers.

1 Introduction

Surface-enhanced Raman spectroscopy (SERS) is a powerful analytical technique for a vast range of chemical and biological sensing applications.[1-4] It is an ultrasensitive and label-free detection method. With the aid of the significantly enhanced localized electrical fields near the surfaces of noble metallic nanostructures, called "hot spots"[5], SERS can reveal the vibrational modes of target molecules located inside those hot spots.[6,7] To sense a single molecule, a SERS enhancement factor (EF) above 10^9 should be achieved.[8]

SERS-active materials can be divided into two categories: nanoparticle colloidal suspensions and structural solid substrates. For both, it would be ideal if the plasmonic nanostructures are chemically stable, easy to prepare in a reproducible manner, and exhibit a spatially uniform, high EF.[9] To achieve reproducible and quantitative SERS analyses, the key issue is to fabricate SERS-active materials in a repeatable way and to improve the uniformity of the hot spots.

A number of SERS-active metallic nanoparticles in colloidal solutions have been synthesized, including shell-isolated nanoparticles,[10] core-shell nanoparticles,[11] and nanoparticles with sharp features.[12,13] The main advantage of them is their high EFs caused by (i) intra- or inter particle plasmonic couplings, and (ii) lightning-rod effect that is specifically pronounced in metallic nanoparticles with sharp features. Since the EF is extremely sensitive to the inter particle spacing, it is necessary to control the size of the gap junctions between nanoparticles to achieve a spatially uniform EF. For example, bio-template assisted synthesis can be used to realize sub-10 nm distance control between nanoparticles.[14] Recently, reliable and quantitative SERS analysis has been achieved using core–shell nanoparticles with embedded internal standards,[15] or alkanethiolate ligand-regulated silver nanoparticle films.[16]

A vast variety of top-down process flows have been employed to fabricate SERS-active structural solid substrates.[17] Most of them are lithography-based techniques, which first tailor mask layers to form different nanostructured patterns, that are then transferred into a variety of substrate materials. The realised structures are subsequently metalized to make the surface SERS-active.[18-22] Strong EFs are obtained at hot spots formed either at the gap junctions between individual structures[23-25] or at the metallic

nanogrooves[26] and nanotips.[27,28] Structural solid SERS substrates usually exhibit more reproducible SERS signals across larger surface areas compared to colloidal nanoparticle systems, at the cost of lower EFs.[29-31] To our knowledge, there is no report to date that demonstrates SERS reproducibility in large scale fabricated SERS substrates based on rigorous statistical examinations. Since an excellent SERS reproducibility across large surface areas is the prerequisite for reliable SERS analyses, this work has both academic as well as industrial relevance.

Using a lithography-free reactive ion etch (RIE) process followed by e-beam assisted metal evaporation, we have developed large-area silver capped silicon nanopillars (Si NPs) with a high aspect ratio and used these as SERS substrates.[32-34] The fabricated Si NPs are flexible and will lean towards their nearest neighbours as deposited analyte solution evaporates, creating self-assembled SERS hot spots in which the analyte molecules are located. Average EFs of above 10^8 and detection limit down to 10^{-10} M have been achieved.[34] A key advantage of such SERS substrates is their simple fabrication process. The fabrication procedure is fast, repeatable and does not require any lithographic steps. The low fabrication costs enable these SERS substrates to be used as cheap single use consumables.

In spite of the aforementioned advantages, challenges remain for the NP substrate to facilitate reproducible SERS signals. According to our previous report,[34] the SERS intensities of the NP substrate exhibit a relative standard deviation (RSD) of around 14% across a 5 × 5 mm^2 surface area. In addition, we have yet to demonstrate a good macroscale reproducibility of the SERS signal.

Large-area SERS enhancement uniformity is a fundamental prerequisite to achieve reliable measurements and a prerequisite if quantitative SERS is to be realised. The aim of this work is to tackle EF uniformity issues for the NP substrate by means of an improved nanofabrication process. In SERS, the overall signal can be considered the sum of the signals contributed by all analytes located in the hot spots probed by the excitation laser. Inhomogeneity of the SERS signals can be ascribed to i) the electrical field enhancement in the hot spots being sensitive to the detailed shape of plasmonic nanostructure as well as the coupling between nanostructures, which can vary by several orders of magnitude,[35] and ii) the uneven distribution of analytes in individual hot spots.

To improve SERS uniformity and reproducibility of the Si NP substrate, one approach is to increase the density of the NPs. In this case, the leaning NPs are expected to form larger and denser packed clusters that exhibit more uniform hot spot properties, due to shorter average distances from each NP to its neighbours. There is a need for further experimental work to (i) find and systematically evaluate the experimental parameters that affect the density of the NPs, and subsequently (ii) modify and develop the lithography-free process to fabricate high-density Si NPs with reproducible SERS intensities and large-area SERS uniformities, which would consequently qualify them for reliable and reproducible SERS analyses.

In this paper, we first provide insights into the mask-less RIE process that produces Si NPs on a 4-inch silicon wafer. We show that by decreasing the chamber pressure during etching, the density of the fabricated NPs can be systematically increased. Thereby, Si NPs of uniform heights with an increased density as high as approximately 48 NPs μm^{-2} can be fabricated. These NPs are able to form, via leaning, large and densely packed clusters that exhibit more uniformly spaced hot spots, compared to the NPs arrays with lower densities, as shown by **Figure 1**. Next, macroscale SERS uniformity and wafer-to-wafer SERS reproducibility of the densely clustered Si NPs are evaluated. SERS RSDs of around 2.5% are observed across 1 mm distances. Inch-scale SERS RSDs of around 6% are achievable, and averaged SERS intensities exhibit an RSD of around 1.5% across three wafers. This indicates that such a process is capable of fabricating high-density Si NPs with extremely large-scale SERS uniformity, and more importantly, with excellent reproducibility. Lastly, an example of macroscale reproducible SERS analyses is given. Using two sets of specimens of ~1 × 1 cm^2 surface areas taken from two wafers, fast and reproducible SERS analyses of BPE in ethanol of 1 μL sample volumes with concentrations from 4 x 10^{-7} M (73 ppb) to 10^{-2} M are demonstrated.

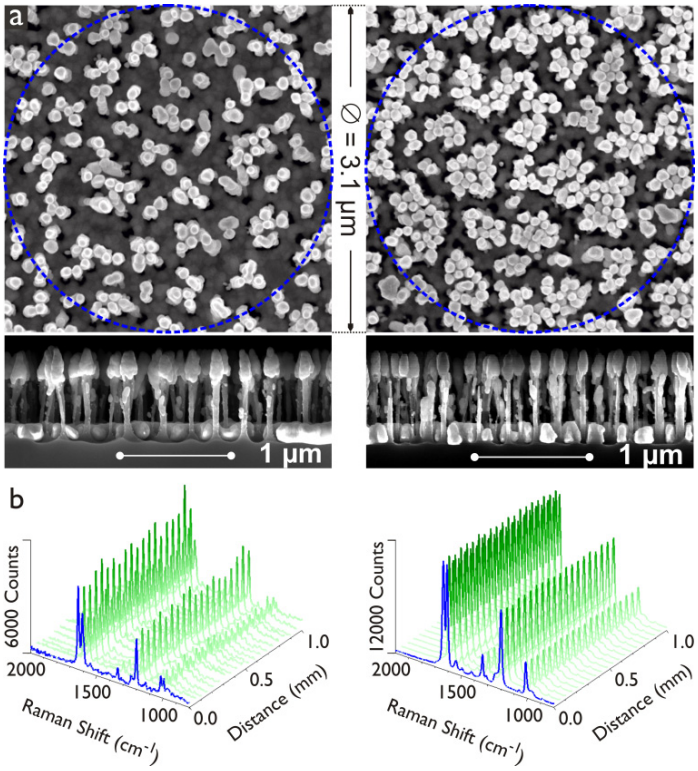

Figure 1. (a) Top-view and cross-sectional SEM images of the Si NPs. The density of the NPs is ~19 NPs μm^{-2} and ~48 NPs μm^{-2} for the left-side and right-side images, respectively. (a) top) The NPs are leaned by dripping and drying of 1 µL 10^{-3} M BPE in ethanol solution. The dotted blue circles represent the spot area of the SERS excitation laser. (b) Two scanned SERS spectra across a 1 mm line, acquired correspondingly on the NP substrate shown in (a) above each map. For clarity, each map only shows 20 spectra.

2 Results and Discussions

2.1 Density Control in the Lithography-free Process

To improve SERS uniformity and reproducibility of the Si NP substrate, our approach was to increase the density of the NPs. Here, we demonstrate how the density of the NPs can be controlled in the employed lithography-free process.

It was found, that during the RIE, the pressure of the chamber has an influence on the density of the fabricated Si NPs. To gain a better control of the process, it was logical to perform a systematic study to reveal the relationship between p, the RIE chamber pressure and D, the density of NPs. This was specifically done by i) fabricating NPs under four different values of p, ranging from 18 mTorr to 36 mTorr, followed by ii)

SEM characterization of these NPs both before and after clustering. The results are shown in **Figure 2**.

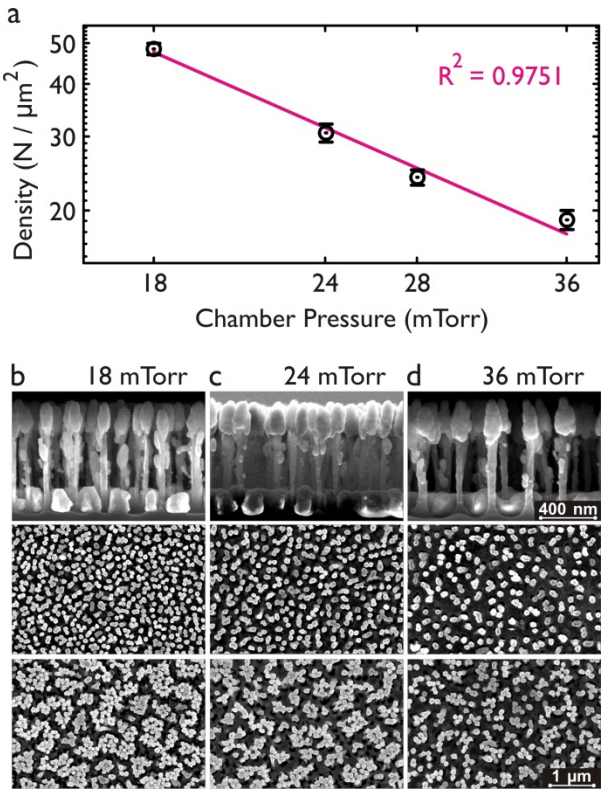

Figure 2. (a) Log-log plot for the density of the NPs *D* versus the RIE chamber pressure *p*. (b)-(d) Representative SEM images for the NPs fabricated with a RIE chamber pressure of 18 mTorr, 24 mTorr and 36 mTorr, respectively. From the first row to the third row, cross-sectional images, top-view images of the vertical NPs, and top-view images of the leaning NPs are shown in sequence. The clusters of NPs were formed by drying the deposited of ethanol. The Ag deposition thickness was 185 nm for all the samples.

It can be seen from Figure 2b-d that a lower *p* leads to a higher *D*. Lowering the chamber pressure increases the mean free path of the reactive ions, and thus intensifies the anisotropic etch. Initially formed Si pillars are vulnerable to isotropic etch, thus a more anisotropic RIE retains more pillars, and increases the density of the NPs. To quantify such an effect, *D* versus *p* is plotted using double logarithmic axes, shown in Figure 2a. It can be seen that by decreasing *p* from 36 mTorr to 18 mTorr, *D* increases from ~19 NPs μm^{-2} to ~48 NPs μm^{-2}. Furthermore, Figure 2a shows that *D* exhibits a

monomial dependence on p, as is shown by the linear fit in the log-log plot with a correlation of $R^2 = 0.9751$. Therefore, the following equation:

$$\boldsymbol{D = ap^b} \quad (1)$$

, where $a = 3000$, $b = -1.433$, and $p \in [18, 36]$ mTorr can be established to estimate the density of the NPs D, given the value of the RIE chamber pressure p.

Further reducing the RIE chamber pressure leads to the production of irregular NPs with non-uniform heights. **Figure 3b and 3c** show the irregular NPs fabricated under p of 16 mTorr and 12 mTorr, respectively. For these structures, at the apex of the Si NPs, due to the significant variation in heights, regular Ag caps in the same horizontal plane cannot be formed. As a result, SERS performance degrades, since densely clustered Ag caps with uniform nanogaps no longer form via leaning of the NPs. In Figure 3a it is seen that, irregular NPs fabricated under p of 16 mTorr and 12 mTorr exhibit only ∼30% and ∼15% of the SERS signal obtained on NPs with a uniform height fabricated under a p of 18 mTorr.

Based on the results above, it is reasonable to set p = 18 mTorr as the standard RIE chamber pressure for fabrication of high-density Si NPs, as applying it produces NPs of the highest density with a uniform height. It should be pointed out that in all our previous studies, only substrates with a density of ∼19 NPs μm^{-2} were used.[32-34, 36-40]

It is worth noting that, for the high-density Si NPs, fixing p = 18 mTorr as the employed RIE chamber pressure, the fabrication process can further be optimized in terms of SERS EF, by changing RIE etching time and Ag deposition thickness. Systematic optimization results are shown in the supplementary material in **Figure S1**. It was found that by employing 255 seconds of etching with an Ag deposition thickness of 185 nm, a maximum SERS signal could be obtained. The calculated average SERS EF of the optimized substrate is $\sim 1.11 \times 10^8$. Details of the calculation are in the supplementary material.[41,42] Additionally, dark-field scattering measurements were carried out on the NPs fabricated by the optimized process. Results are shown in the supplementary material in **Figure S2**. The scattering intensity of the leaning NPs displays a maximum around 800 nm, which is close to the wavelength of the employed Raman laser (780 nm). Detailed theoretical and experimental investigations regarding the localized plasmon resonances of such type of structures can be found in our previous study.[36]

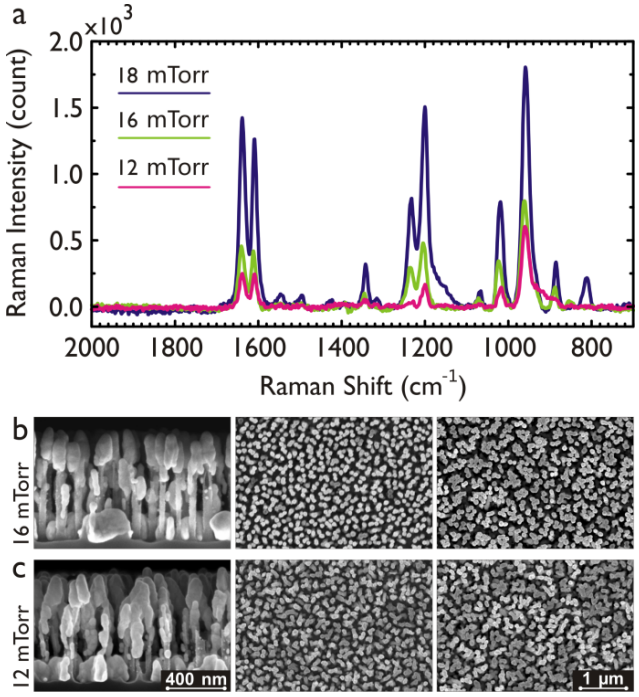

Figure 3. (a) SERS spectra of 10^{-4} M BPE measured on Si NPs fabricated using different RIE chamber pressures. The NPs were leaned by dripping and drying of 1 μL 10^{-4} M BPE in ethanol solution. (b) and (c) Representative SEM images for the NPs fabricated using a RIE chamber pressure of 16 mTorr and 12 mTorr, respectively. From the first column to the third column, cross-sectional images, top-view images of the vertical NPs, and top-view images of the leaning NPs are shown. In (b) and (c) the clusters of NPs were formed by dripping and drying of ethanol.

2.2 Influence of NP Density on SERS Uniformity

Here, the influence of the density of the NPs on the SERS uniformity is presented. Three ~1 × 1 cm^2 Si NP specimens, fabricated under different RIE chamber pressures were used for the experiment. The employed pressure was 18 mTorr, 24 mTorr and 36 mTorr, producing substrates with a density of ~48 NPs μm^{-2}, ~31 NPs μm^{-2} and ~19 NPs μm^{-2}, accordingly. The NPs leaned towards their neighbours and clusters of NPs were formed after dripping and drying of 1 μL 10^{-4} M BPE in ethanol solution. The droplet immediately spread over the whole specimen area and completely evaporated several seconds thereafter. SEM images of the NPs were recorded both before and after leaning (Figure 2b-d). SERS line scans were then conducted on all three specimens. Each line scan was 1 mm long with a step size of 10 μm. The obtained spectra are shown in

Figure 4b. The SERS intensities at the 1641 cm^{-1} BPE peak were averaged, and the corresponding RSDs were calculated. The results are shown in Figure 4a. It can be seen that the SERS RSD decreases from ~10.5% to ~4.5% when increasing the NP density from ~19 NPs μm^{-2} to ~48 NPs μm^{-2}. Such a result confirms our hypothesis , that an increasing density of the NPs would improve the SERS uniformity. By increasing NP density, the leaning NPs form larger and more densely packed clusters that exhibit more uniform hot spot properties, due to the shorter average distances from each NP to its

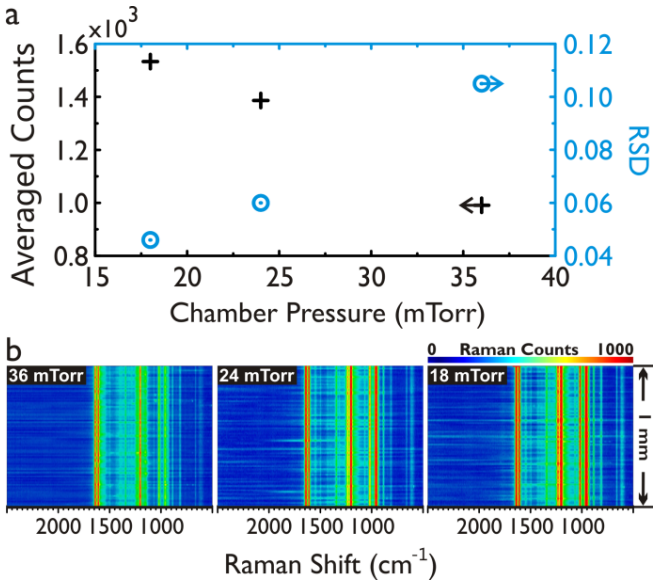

Figure 4. (a) The averaged SERS intensities and the corresponding RSDs at the 1641 cm^{-1} BPE peak for NPs of different densities fabricated under different RIE pressures, obtained based on the scanned spectra in (b). (b) SERS line scans of 10^{-4} BPE on three specimens containing NPs fabricated under different RIE chamber pressures. The employed pressure *p* was 18 mTorr, 24 mTorr and 36 mTorr, producing NPs with a *D* of ~48 NPs μm^{-2}, ~31 NPs μm^{-2} and ~19 NPs μm^{-2}, accordingly. The NPs leaned towards their neighbours and clusters of NPs were formed after dripping and drying of 1 µL 10^{-4} M BPE in ethanol solution. SEM images of the NPs before and after leaning are shown in Figure 2b-d. The scanned distance was 1 mm, with a step size of 10 µm. Each map contains 101 spectra.

neighbours. This effect can clearly be seen in Figure 2b-d from the SEM images of the clustering NPs. Besides, it should be pointed out that the SERS intensity increases when increasing NP density. As shown by Figure 4a, the averaged SERS intensity of the 1641

cm^{-1} BPE peak increases by ~50% when increasing NP density from ~19 NPs μm^{-2} to ~48 NPs μm^{-2}. This is reasonable, since the laser spot covers a greater number of hot spots for NPs with a higher density, as has been illustrated in Figure 1.

2.3 Large-area SERS Uniformity and Wafer-to-wafer SERS Reproducibility of the Densely Clustered Nanopillars

To improve SERS uniformity, Si NP substrates consisting of high-density NPs (~48 NPs μm^{-2}) were fabricated by an optimized process. They exhibited very good SERS uniformity across a 1 mm distance, as shown and discussed in section 2.2. In this section, we investigate and demonstrate even larger scale SERS uniformity and wafer-to-wafer SERS reproducibility for the densely clustered Si NPs. For such purposes, we performed straight-line SERS scans on three wafers. Each line scan started from the centre of the 4-inch wafer and ended at its edge, with a step size of 100 μm. The schematic in **Figure 5a** shows the track of the line scan. The analyte was 10^{-4} M BPE dissolved in ethanol. The incubation time was less than 5 seconds. Figure 5b shows the line scanned SERS spectra. It can be seen that for all the three wafers, the SERS intensity remains high until half way towards the wafer edge, whereafter it decreases dramatically. To quantify such an effect, Figure 5e plots the trajectory of the SERS intensities at the 1641 cm^{-1} BPE peak for wafer 1. It can be seen that between 0 - 0.75 inch from the centre of the wafer, the SERS signal remains relatively stable. It then gradually decreases after the 0.75-inch point, and falls dramatically after the 1-inch point. This is also true for the other two wafers. As shown in Figure 5c and 5d, for all the three wafers, after extending the statistical region from 0 – 0.75 inch to 0 – 1 inch, the averaged SERS signal of the 1641 cm^{-1} BPE peak decreases with an increased RSD. In addition, Figure 5c shows that the high-density Si NPs exhibit an extremely long-range SERS uniformity, which is ~7% across 0.75 inch, with averaged SERS intensities exhibiting a RSD of ~1.5% across the

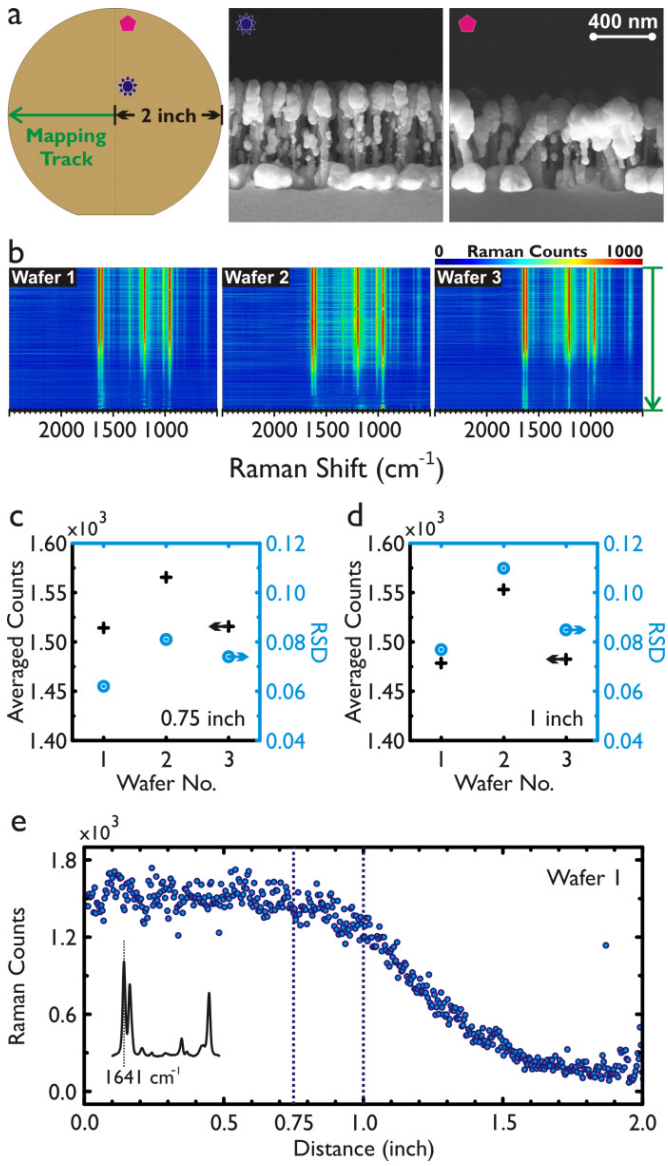

Figure 5. (a) Schematic of the track for the SERS line scans in (b), plus cross-sectional SEM images of the fabricated Si NPs (~48 NPs μm^{-2}) near the middle and near the edge of a wafer. (b) Line scanned SERS spectra on three wafers following the track shown in (a). Each line scan started from the centre of the 4-inch wafer towards its edge, with a step size of 100 μm. A map consists of 255 spectra. The analyte was 10^{-4} M BPE dissolved in ethanol. The incubation time was less than 5 seconds. Clusters of the NPs were formed when the analyte solution evaporated. (c) - (d) The averaged SERS intensities and the corresponding RSDs of the 1641 cm^{-1} BPE peak, calculated according to the SERS maps in (b) for three different wafers. The statistical range for (c) and (d) is 0 – 0.75 inch and 0 – 1 inch, respectively, from the centre of the wafer. (e) Trajectory plot of the SERS intensities at the 1641 cm^{-1} BPE peak for wafer 1 across the SERS line scan shown in (b).

three wafers, indicating an excellent reproducibility of the process. Such results imply that in order to carry out reproducible and reliable SERS analysis, one should only use specimens in a circle, which is homocentric with the 4-inch wafer and has a 1.5-inch diameter. To improve yield, the whole process can be transferred to 6-inch or 8-inch wafers or larger, since the drop of the SERS intensity towards the edge of the wafer is hypothesised to be due to the macro loading effect during the mask-less RIE process.[43] The macro loading effect alters and randomizes the morphology of the NPs which are close to the edge of the wafer, as shown in the SEM images in Figure 5a.

2.4 Reproducible SERS Analysis on High-density Nanopillars

In this section, we show an example of macroscale reproducible SERS analyses using the high-density Si NPs. SERS analyses of BPE in ethanol of 1 μL sample volumes with concentrations from 4 x 10^{-7} M (73 ppb) to 10^{-2} M were performed on two sets of specimens taken respectively from two wafers. Each specimen had ~1 × 1 cm^2 surface areas. It is worth noting that sensing analyte of low concentrations becomes harder, since the absolute number of the analyte molecules decreases. This consequently reduces the number of analyte molecules that can adhere to the substrate surface, resulting in weaker SERS signals. In this study, a very low sample volume (1 μL) was chosen since being able to sense analytes in small sample volumes in a short time is needful for many practical applications.[44,45] To compensate the uneven distribution of the low-concentration analytes on the surface of the NPs, a SERS line scan of 1 mm distance with a step size of 10 μm composed one analysis. Doing this essentially increased the total probing area of the Raman laser by 100 times. It is noteworthy that the analysis was still fast, since measuring an individual spot only took 3 seconds (1s exposure × 3 times). For each analysis, we recorded the averaged SERS intensity and the corresponding RSD at the 1641 cm^{-1} BPE Raman peak.

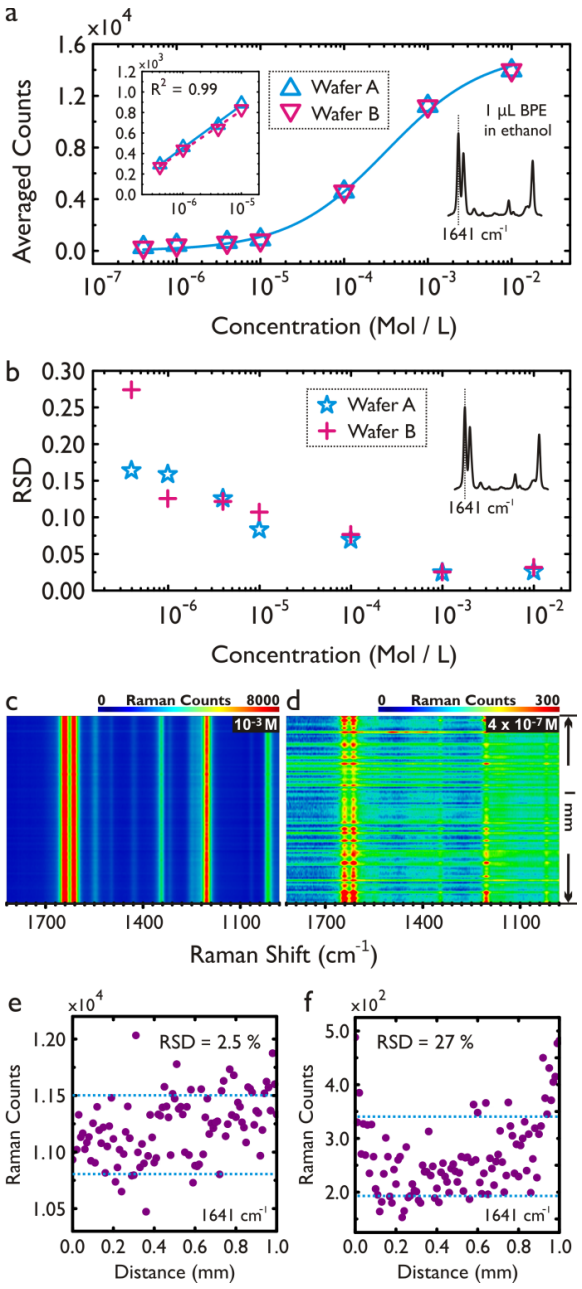

Figure 6. SERS analyses of BPE in ethanol of 1 µL sample volumes with concentrations from 4 x 10^{-7} M to 10^{-2} M. The analyses were performed on two sets of specimens taken from two wafers. Only the specimens from the centre of each wafer were used. Each specimen has~1 × 1 cm^2 surface area. Clusters of NPs were formed by dripping and drying of the analyte solution. A straight-line SERS scan of 1 mm distance with a step size of 10 µm composes one analysis. (a) and (b) the recorded averaged SERS intensities and the corresponding RSDs at the 1641 cm^{-1} BPE peak. (c) and (d) line scanned SERS spectra on specimens of wafer B at 10^{-2} M and 4 x 10^{-7} M. (e) and (f) the trajectory plot of the 1641 cm^{-1} BPE peak intensity corresponding to (c) and (d), respectively.

Results are shown in **Figure 6a** and **6b**. It can be seen from Figure 6a that the SERS analysis is reproducible between the two wafers. This indicates that i) densely clustered NPs exhibit very good SERS uniformities across macroscale areas (inch-scale), via the improved hot spot uniformity, and ii) the fabrication process is highly reproducible, as have been demonstrated and discussed previously in details. The line scanned intensities of the 1641 cm^{-1} BPE Raman peak for all the samples are shown in the supplementary material in Figure S3. Figure 6b shows that the RSD increases from ~2.5% to ~25% when the concentration of BPE decreases from 10^{-3} M to 4 x 10^{-7} M. Such an increase is hypothesised to be due to the uneven distribution of the analytes on the surface of the NPs. Direct evidence can be found in the maps and the corresponding intensity trajectory plots of the 1641 cm^{-1} BPE peak for 10^{-3} M and 4 x 10^{-7} M, shown by Figure 6c – 6f. To reliably and quantitatively sense even lower concentrations with the same small sample volume of 1 μL using such structures, the analyses should be performed with the aid of other techniques, such as surface functionalization and complex statistical modelling, which is out of the scope of this study.

3 Conclusion

Large-area high-density Si NPs (~48 NPs μm^{-2}) that are capable of forming densely packed clusters are fabricated using a two-step lithography-free process. The nanofabrication process is cheap, fast and is suitable for mass production in standard IC foundries. The key to increase the density of the NPs is to decrease the chamber pressure during the maskless RIE process. We have shown that the density exhibits a monomial dependence on the RIE chamber pressure. The process is further optimized in terms of SERS EF. The optimized structures exhibit macroscale SERS uniformities (RSD: ~2.5% in mm scale, ~7% in inch scale) and an excellent SERS reproducibility (RSD: ~1.5% across three wafers), with an average SERS EF of $>10^8$. Wafer-to-wafer reproducible and reliable SERS analyses of BPE in ethanol from 1 μL sample volumes with concentrations from 4 x 10^{-7} M (73 ppb) to 10^{-2} M are also demonstrated. Our experimental findings demonstrate that densely clustered Si NPs are strong candidates for obtaining reproducible and reliable SERS spectra. From a practical point of view these SERS substrates are particularity interesting since they are easy to handle and store and

the fabrication is scalable, facilitating a wide and simple use of SERS in sensing applications.

4 Experimental Section

Fabrication of SERS nanopillars: The SERS substrate fabrication process flow can be divided into three parts. First, starting from a 4-inch Si wafer, a mask-less RIE was employed to form Si NPs with radius ≈ 20 ± 4 nm and height ≈ 600 nm. P-type single-side (100) polished wafers were used (Topsil). Mask-less RIE was performed in an Advanced Silicon Etcher (Surface Technology Systems MESC Multiplex ICP) at an SF_6:O_2 flow ratio of 1.12, a platen power of 120 W, and a chamber pressure from 18 mTorr to 36 mTorr depending on the required NP density. The employed etching time was 255 seconds. Si NPs were formed at a rate of ~3 nm/s. Next, an O_2 plasma treatment was applied to remove RIE by-products from the surface of the Si NPs. An O_2 flow of 45 sccm, a platen power of 20 W, a coil power of 800 W, and a chamber pressure of 10 mTorr were used. The time of the O_2 plasma treatment was 1 minute. Lastly, a 185 nm thick Ag film was deposited onto the Si NPs by e-beam evaporation. An Alcatel SCM 600 was used for the deposition at a pressure of 2×10^{-6} mbar, with a deposition rate of 10 Å/s. The deposition resulted in the formation of Ag caps at the apex of the Si NPs, along with an Ag film on the underlying Si surface. Representative cross-sectional SEM images of the fabricated Si NPs are shown in Figure 1. Silver was chosen due to its favourable dielectric function which results in strong plasmonic resonances for the Si NPs with the applied Raman laser excitation with a 780 nm wavelength.[36] The manufactured substrates are stored in a vacuum Thermo Scientific Nalgene desiccator to minimize oxidation.

SEM characterization: SEM images were recorded using a Zeiss Supra 40VP field emission scanning electron microscope with a maximum spatial resolution of 1.0 nm. An in-lens detector was used. A working distance of ~2 mm and an acceleration voltage of 8.0 kV were used. The angle between the incident electron beam and the surface of the Si NPs was 90° and 0° for top-view and cross-sectional imaging, respectively. In the density analysis shown in Figure 2a, each data point was obtained by three measurements via SEM analyses on different regions of the samples.

SERS measurements: A Thermo Scientific DXR confocal Raman microscope with a spatial resolution of 1 μm and a confocal depth of 2 μm was used for all the SERS measurements. The microscope was coupled to a single grating spectrometer with a 5 cm^{-1} FWHM spectral resolution and a ± 2 wavenumber accuracy. All Raman measurements were conducted at room temperatures. The absolute Raman intensities of the instrument over its detectable spectral range were calibrated according to a known lamp spectrum along with the Raman signal produced on solid polystyrene. For SERS measurements on the Si NPs, unless otherwise noted, the signal collection time was 1 s and was averaged 3 times; a 25 μm slit and a 10X objective lens were used; an excitation wavelength of 780 nm was employed at 0.1 mW (0.3 mW in Figure 1, 7 and S3) with a laser spot of 3.1 μm in diameter; a step size of 10 μm (100 μm for Figure 6) was used. Except for the measurements shown in Figures 1, 6, 7, and S3, a 1 μL volume of 10^{-4} M BPE dissolved in ethanol was deposited onto a Si NP specimen. The deposited droplet spread over the whole specimen area of ~1 × 1 cm^2 and completely evaporated in a few seconds. The fabricated NPs are flexible and lean towards their nearest neighbours as the deposited analyte solution evaporated, creating self-assembled SERS hot spots in-between and at the necks of the Ag caps.[36] Top-view SEM images of the leaning Si NPs of two different densities (~19 NPs μm^{-2} and ~48 NPs μm^{-2}) are shown in Figure 1.

5 Supporting Information

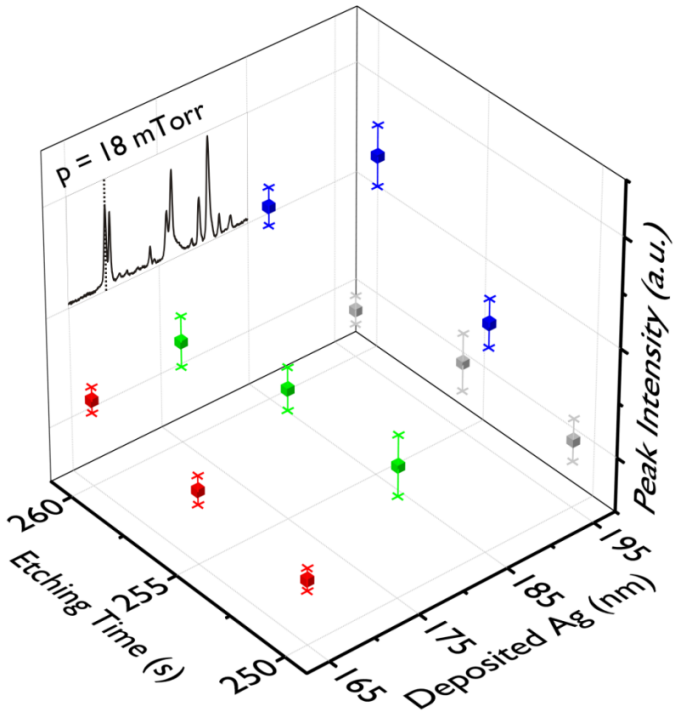

Figure S1. Optimization of the high-density Si NPs (~48 NPs μm^{-2}) in terms of surface enhanced Raman scattering (SERS) intensity, by systematically changing the mask-less etching time and the deposition thickness of the Ag. The plot shows the averaged BPE 1641 cm^{-1} peak intensities, each obtained over 5 spectra. A 1 µL volume of 10^{-4} M BPE dissolved in ethanol was first deposited onto the specimen. The droplet then spread over the whole specimen area of ~1 × 1 cm^2 and completely evaporated in several seconds during which the NPs leaned towards each other and formed clusters. The signal collection time was 1 s and was averaged 3 times. A 25 µm slit and a 10x objective lens were used. An excitation wavelength of 780 nm was employed at 0.1 mW.

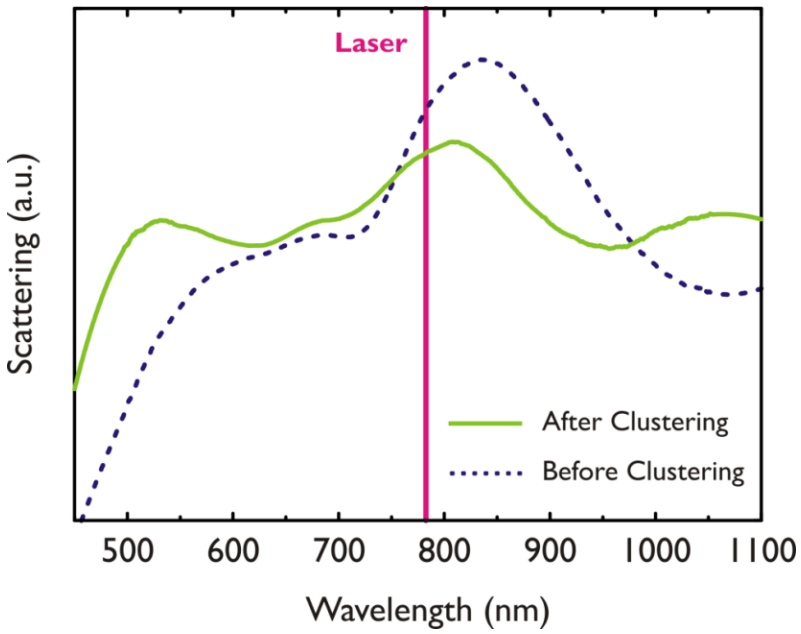

Figure S2. Dark-field scattering spectra of the optimized high-density Si NPs (~48 NPs μm^{-2}) before and after clustering of the NPs. Clustering is induced by dripping and drying of ethanol. The 780 nm line of the Raman excitation laser is highlighted in the figure. For the dark-field measurement, a Nikon Ti-U inverted microscope was used with a CF LU Plan Fluor Epi 50x objective, which had a working distance of 1 mm and a NA of 0.8. The incident angle was ~50 degree. The scattered light was collected from the centre of the objective and was subsequently guided into a spectrometer (Shamrock Spectrograph SR-303I-A, equipped with Andor Newton 970 EMCCD).

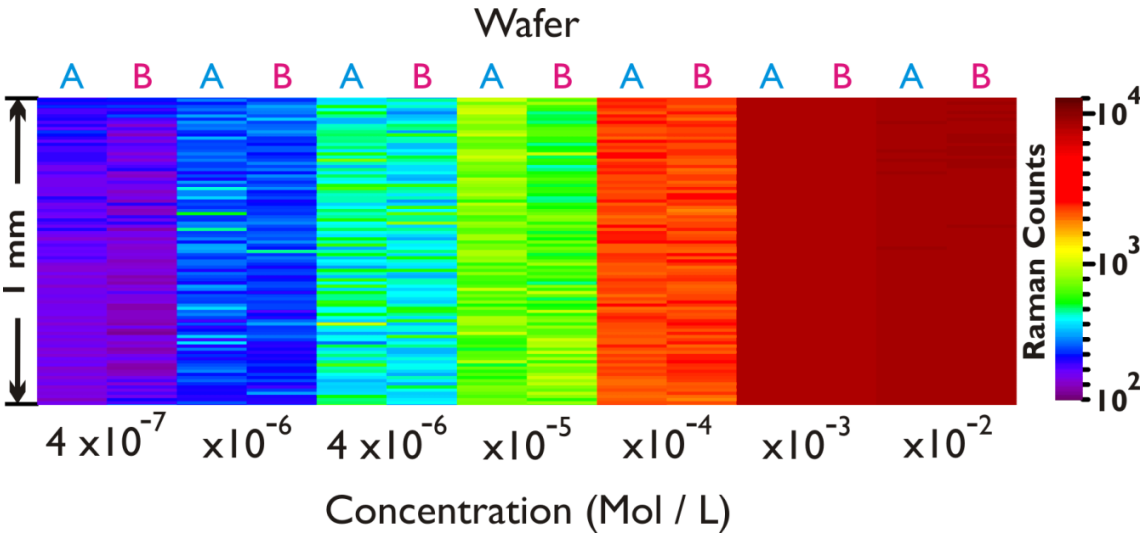

Figure S3. Distribution of the SERS intensity at the 1641 cm^{-1} BPE peak obtained on high-density Si NPs. BPE in ethanol of 1 µL sample volumes with concentrations from 4 x 10^{-7} M (73 ppb) to 10^{-2} M were deposited on two sets of specimens taken respectively from two wafers. Each specimen had ~1 × 1 cm^2 surface areas. The SERS intensities at the 1641 cm^{-1} BPE peak was recorded by performing line scans. Every scan was of 1 mm distance with a10 µm step size.

The average SERS enhancement factor (EF) of the optimized substrate was calculated from the formula:

$$EF = \frac{I_{SERS}/N_{SERS}}{I_{Ref}/N_{Ref}}$$

The numbers used in the calculation are obtained using the method described in reference 41 in the main text. To be specific, to establish the value for I_{Ref} a 0.1 M ethanol solution of BPE was poured into a petri dish. With a 50X objective and using an excitation wavelength of 780 nm and a power of 1 mW, 1.4 counts s^{-1} (I_{Ref}) were measured at the 1200 cm^{-1} peak. Using the interaction volume of 60 μm^3, the number of molecules responsible for the Raman signal (N_{Ref}) was estimated to be 3.60 x 10^9. To establish the values for I_{SERS} a 1 × 1 cm^2 piece of the optimized Si NP substrate with a density of ~48 NPs μm^{-2} was immersed into a 10 mM ethanoic solution of BPE for 1 hour. Hereafter, the substrate was removed and dried in air. After drying, the substrate was rinsed in ethanol. Using identical conditions as for I_{Ref}, a signal intensity of ~65000 counts s^{-1} was

measured for the 1200 cm^{-1} peak. The number of molecules inside the laser spot was estimated by assuming a monolayer of BPE all over the substrate. A packing density of 3.3×10^6 BPE molecules μm^{-2} was used for this calculation.[42] With a laser spot size with a radius of 0.8 μm and taking the topography of the silver surface on the Si pillar into consideration, the effective surface area probed by the laser was ~0.45 μm^2. This gives an estimate of N_{SERS} = 1.5 x 10^6 molecules. Hence, the average EF becomes 1.11 x 10^8.

6 Acknowledgements

This work was funded by (i) the NAPLAS project, Danish Council for Independent Research, and (ii) the HERMES Project, European Research Council under the European Union's Seventh Framework Programme.

References

[1] P. L. Stiles, J. A. Dieringer, N. C. Shah, R. P. Van Duyne, *Annu. Rev. Anal. Chem.* **2008**, *1*, 601.

[2] B. Sharma, R. R. Frontiera, A.-I. Henry, E. Ringe, R. P. Van Duyne, *Mater. Today* **2012**, *15*, 16.

[3] C. Costas, V. López-Puente, G. Bodelón, C. González-Bello, J. Pérez-Juste, I. Pastoriza-Santos, L. M. Liz-Marzán, *ACS Nano* **2015**, *9*, 5567.

[4] A. Barhoumi, N. J. Halas, *J. Am. Chem. Soc.* **2010**, *132*, 12792.

[5] M. Käll, H. Xu, P. Johansson, *J. Raman Spectrosc.* **2005**, *36*, 510.

[6] K. Kneipp, *Physics Today* **2007**, *60*, 40.

[7] L. Tong, H. Xu, M. Käll, *MRS Bulletin* **2014**, *39*, 163.

[8] E. C. Le Ru, P. G. Etchegoin, *Annu. Rev. Phys. Chem.* **2012**, *63*, 65.

[9] S. Schlücker, *Angew. Chem. Int. Ed.* **2014**, *53*, 4756.

[10] J. F. Li, Y. F. Huang, Y. Ding, Z. L. Yang, S. B. Li, X. S. Zhou, F. R. Fan, W. Zhang, Z. Y. Zhou, D. Y. Wu, B. Ren, Z. L. Wang, Z. Q. Tian, *Nature* **2010**, *464*, 392.

[11] A. K. Samal, L. Polavarapu, S. Rodal-Cedeira, L. M. Liz-Marzán, J. Pérez-Juste, I. Pastoriza-Santos, *Langmuir* **2013**, *29*, 15076.

[12] V, López-Puente, S. Abalde-Cela, P. C. Angelomé, R. A. Alvarez-Puebla, L. M. Liz-Marzán, *J. Phys. Chem. Lett.* **2013**, *4*, 2715.

[13] L. Pérez-Mayen, J. Oliva, A. Torres-Castro, E. De la Rosa, *Nanoscale* **2015**, *7*, 10249.

[14] D.-K. Lim, K.-S. J, J.-H. Hwang, H. Kim, S. Kwon, Y. D. Suh, J.-M. Nam, *Nat. Nanotechnol.* **2011**, *6*, 452.

[15] W. Shen, X. Lin, C. Jiang, C. Li, H. Lin, J. Huang, S. Wang, G. Liu, X. Yan, Q. Zhong, B. Ren, *Angew. Chem.* **2015**, *127*, 7416.

[16] H.-Y. Chen, M.-H. Lin, C.-Y. Wang, Y.-M. Chang, S. Gwo, *J. Am. Chem. Soc.* **2015**, *137*, 13698.

[17] B. Sharma, M. F. Cardinal, S. L. Kleinman, N. G. Greeneltch, R. R. Frontiera, M. G. Blaber, G. C. Schatz, R. P. Van Duyne, *MRS Bulletin* **2013**, *38*, 615.

[18] T.-W. Chang, M. R. Gartia, S. Seo, A. Hsiao, G. L. Liu, *Nanotechnology* **2014**, *25*, 145304.

[19] C. Hou, G. Meng, Q. Huang, C. Zhu, Z. Huang, B. Chena, K. Suna, *Chem. Commun.* **2014**, *50*, 569.

[20] Y. Zhao, Y.-L. Zhang, J.-A. Huang, Z. Zhang, X. Chen, W. Zhang, *J. Mater. Chem. A* **2015**, *3*, 6408.

[21] J. Li, C. Chen, H. Jans, X. Xu, N. Verellen, I. Vos, Y. Okumura, V. V. Moshchalkov, L. Lagaea, P. V. Dorpe, *Nanoscale* **2014**, *6*, 12391.

[22] V. Merk, J. Kneipp, K. Leosson, *Adv. Opt. Mater.* **2013**, *1*, 313.

[23] X. Liu, Y. Shao, Y. Tang, K.-F. Yao, *Sci. Rep.* **2014**, *4*, 5835.

[24] M. Hu, F. S. Ou, W. Wu, I. Naumov, X. Li, A. M. Bratkovsky, R. S. Williams, Z. Li, *J. Am. Chem. Soc.* **2010**, *132*, 12820.

[25] A. Hakonen, M. Svedendahl, R. Ogier, Z.-J. Yang, K. Lodewijks, R. Verre, T. Shegai, P. O. Anderssonb, M. Käll, *Nanoscale* **2015**, *7*, 9405.

[26] M. Yilmaz, M. Ozdemir, H. Erdogan, U. Tamer, U. Sen, A. Facchetti, H. Usta, G. Demirel, *Adv. Funct. Mater.* **2015**, *25*, 5669.

[27] A. S. D. S. Indrasekara, S. Meyers, S. Shubeita, L. C. Feldman, T. Gustafsson, L. Fabris, *Nanoscale* **2014**, *6*, 8891.

[28] Y. Lu, G. L. Liu, J. Kim, Y. X. Mejia, L. P. Lee, *Nano Lett.* **2005**, *5*, 119.

[29] Q. Zhang, Y. H. Lee, I. Y. Phang, C. K. Lee, X. Y. Ling, *Small* **2014**, *10*, 2703.

[30] H. Liu, X. Zhang, T. Zhai, T. Sander, L. Chen, P. J. Klarb, *Nanoscale* **2014**, *6*, 5099.

[31] A. N. Severyukhina, B. V. Parakhonskiy, E. S. Prikhozhdenko, D. A. Gorin, G. B. Sukhorukov, H. Möhwald, A. M. Yashchenok, *ACS Appl. Mater. Inter.* **2015**, *7*, 15466.

[32] M. S. Schmidt, J. Hübner, A. Boisen, *Adv. Mater.* **2012**, *24*, OP11.

[33] J. Yang, M. Palla, F. G. Bosco, T. Rindzevicius, T. S. Alstrøm, M. S. Schmidt, A. Boisen, J. Ju, Q. Lin, *ACS Nano* **2013**, *7*, 5350.

[34] K. Wu, T. Rindzevicius, M. S. Schmidt, K. B. Mogensen, A. Hakonen, A. Boisen, *J. Phys. Chem. C* **2015**, *119*, 2053.

[35] H. Xu, E. J. Bjerneld, M. Käll, L. Börjesson, *Phys. Rev. Lett.* **1999**, *83*, 4357.

[36] K. Wu, T. Rindzevicius, M. S. Schmidt, K. B. Mogensen, S. Xiao, A. Boisen, *Opt. Express* **2015**, *23*, 12965.

[37] R. K. Lauridsen, T. Rindzevicius, S. Molin, H. K. Johansen, R. W. Berg, T. S. Alstrøm, K. Almdal, F. Larsen, M. S. Schmidt, A. Boisen, *Sens. Biosens.* **2015**, *5*, 84.

[38] J. J. Castillo, T. Rindzevicius, K. Wu, M. S. Schmidt, K. A. Janik, A. Boisen, W. Svendsen, N. Rozlosnik, J. Castillo-León, *J. Nanopart. Res.* **2014**, *16*, 2525.

[39] J. J. Castillo, T. Rindzevicius, K. Wu, C. E. Rozo, M. S. Schmidt, A. Boisen, *J. Raman Spectrosc.* **2015**, *46*, 1087.

[40] M. Palla, F. G. Bosco, J. Yang, T. Rindzevicius, T. S. Alstrom, M. S. Schmidt, Q. Lin, J. Ju, A. Boisen, *RSC Adv.* **2015**, *5*, 85845.

[41] J. D. Caldwell, O. Glembocki, F. J. Bezares, N. D. Bassim, R. W. Rendell, M. Feygelson, M. Ukaegbu, R. Kasica, L. Shirey, C. Hosten, *ACS Nano* **2011**, *5*, 4046.

[42] Y. S. Hu, J. Jeon, T. J. Seok, S. Lee, J. H. Hafner, R. A. Drezek, H. Choo, *ACS Nano* **2010**, *4*, 5721.

[43] R. A. Gottscho, C. W. Jurgensen, D. J. Vitkavage, *J. Vac. Sci. Technol. B* **1992**, *10*, 2133.

[44] A. Hakonen, P. O. Andersson, M. S. Schmidt, T. Rindzevicius, M. Käll, *Anal. Chim. Acta* **2015**, *893*, 1.

[45] U. S. Dinish, C. Y. Fu, K. S. Soh, R. Bhuvaneswari, A. Kumar, M. Olivo, *Biosens. Bioelectron.* **2012**, *33*, 293.

CHAPTER 9

CONCLUDING REMARK

For this thesis, an in-depth understanding of the localized surface plasmon resonances (LSPRs) of the nanopillar arrays for surface-enhanced Raman spectroscopy (SERS) was developed, and the fabrication process of these NPs was engineered and improved in terms of their SERS performance.

3D FEM simulations were first employed to study the plasmonic responses of the Ag capped Si nanopillars (Ag NPs). Results showed that an individual Ag NP supported two LSPR modes, i.e., the particle mode and the cavity mode. When two identical Ag NPs leaned toward each other, their particle modes hybridized into various new LSPR modes, which appeared across a wide spectra region, from 515 nm to 950 nm. Upon excitation, these hybridized LSPR modes generated electromagnetic hot spots in the gap junction between the two leaning NPs, with simulated maximum electrical field enhancement factors (EFs) of ~90. On the other hand, the resonance energy of the cavity mode was dominated by the diameter of the Si pillar, and could not be tuned via leaning. Its corresponding enhanced fields were observed near the neck of the NP. In addition, the presence of the substrate was shown to have little tuning effect on the two LSPR modes of the NP, but could dramatically change the intensity of the two modes, by introducing constructive or destructive interferences of the excitation lights, depending on the distance from the substrate to the Ag cap. The dark-field scattering measurements supported the conclusions drawn from the simulations. It should be point out that the measured scattering peaks were broad, due to the uneven geometries of the fabricated NPs.

Successfully understanding the LSPR properties of the SERS NPs had guiding significance in optimizing their fabrication process, since the generation conditions, and the locations of the electromagnetic hot spots, were made clear. Based on the conclusions presented in the last paragraph, the following could be deduced. (i) The electromagnetic

SERS EF of the NPs was highly dependent on the height of the NPs. (ii) The cavity LSPR mode was a double-edged sword. Its near field could not only enhance the Raman scattering signals of the analytes, but also those of the etching residuals on the Si pillar. Essentially, the cavity mode was the electron oscillations in the bottom part of the Ag cap, coupled via the Si pillar. (iii) The leaning NPs should display a broad SERS-active wavelength, as they supported 1) a number of hybridized LSPR modes covering a wide spectral range, and 2) various cavity LSPR modes at different wavelengths, due to the 'intrinsic tuning' induced by the variation in the diameter of the Si pillars. Indeed, experimentally, the Ag NP substrate was shown SERS-active at both 532 and 780 nm excitations.

Next, the fabrication steps that were important for achieving high SERS intensity and low SERS background, were systematically evaluated. The experimental data showed that the O_2-plasma process and the Cr adhesion layers could be used to reduce the SERS background signals. However, a prolonged exposure to the O_2 plasma induced a more uniform Ag growth on the Si NPs, which produced elongated Ag cap shapes, and led to a lower NP leaning rate as well as a lower SERS intensity. Furthermore, thicker Cr layers (>3 nm) introduced loss, which weakened the plasmon couplings in the Ag cavities, also leading to a lower SERS intensity. In addition, the SERS intensity could be systematically tuned by adjusting the Si NP height and thickness of the evaporated Ag film. Combining all these experimental findings, a recipe to fabricate Ag NPs exhibiting a high SERS signal-to-noise ratio was presented. On the optimized Ag NP substrate, a SERS spectrum of 100 pM/L trans-1,2-bis (4-pyridyl) ethylene (BPE) was obtained, showing distinct characteristic Raman vibrational modes. The measured enhancement factor was of the order of 10^8, and the SERS signal intensity exhibited a standard deviation of around 14% (660 data points) across a 5×5 mm^2 surface area.

Lastly, experiments were conducted to improve the EF uniformity of the Ag NPs, as large-area SERS EF uniformity is a prerequisite if quantitative SERS is to be realised. By increasing density of the NPs, the leaning NPs formed larger and more densely packed clusters, which exhibited more uniform hot spot properties, due to the shorter average distances from each NP to its neighbours. Large-area, high-density Ag NPs (~48 NPs μm^{-2}) that were capable of forming densely packed clusters were presented. The key

to increase the density of the NPs was to decrease the chamber pressure during the maskless RIE process. Experimental results showed that the NP density exhibited a monomial dependence on the RIE chamber pressure. The process was further optimized in terms of SERS EF. The optimized structures exhibited macroscale SERS uniformities (RSD: ~2.5% in mm scale, ~7% in inch scale) and an excellent SERS reproducibility (RSD: ~1.5% across three wafers), with an average SERS EF of $>10^8$. Wafer-to-wafer reproducible and reliable SERS analyses of BPE in ethanol from 1 μL sample volumes with concentrations from 4 x 10^{-7} M (73 ppb) to 10^{-2} M were also demonstrated. These experimental findings demonstrated that densely clustered NPs were strong candidates for obtaining reproducible and reliable SERS spectra.

In summary, a deep understanding of the LSPR coupling effects in the SERS NP structures was established. Their fabrication process was systematically evaluated and optimized. The result was a highly efficient SERS substrate, fabricated by a cost-effective process, displaying a high SERS EF, a low SERS background signal, and a relatively spatially uniform SERS EF. Future studies could be, e.g., the exploration of analytical applications using the developed SERS substrate, in the area of environmental monitoring and food safety.

This Ph.D. thesis presents (i) an in-depth understanding of the localized surface plasmon resonances in the nanopillar arrays for surface-enhanced Raman spectroscopy (SERS), and (ii) systematic ways of optimizing the fabrication process of nanopillar arrays to improve their SERS efficiencies. The Ph.D. project is part of the NAPLAS - NAnoPLAsmonic Sensors project, funded by The Danish Council for Independent Research.

DTU Nanotech
Ørsteds Plads, building 345C
DK-2800 Kgs. Lyngby

http://www.nanotech.dtu.dk/

Published by:
DTU Nanotech
Department of Micro- and Nanotechnology
Technical University of Denmark
Ørsteds Plads, building 345C
DK-2800 Kgs. Lyngby